Force-Based Control for Reduced Deformation Human-Robot Transport of Flexible Objects

Kyle Schultz

A dissertation
submitted in partial fulfillment of the
requirements for the degree of

Doctor of Philosophy

University of Washington

2026

Reading Committee:

Santosh Devasia, Chair

Joseph Garbini

Lance McCann

Program Authorized to Offer Degree:

Department of Mechanical Engineering

University of Washington

Abstract

Force-Based Control for Reduced Deformation Human-Robot Transport of Flexible Objects

Kyle Schultz

Chair of the Supervisory Committee:
Santosh Devasia
Department of Mechanical Engineering

This thesis considers force-based human-robot collaborative transportation (co-transport) of flexible objects using only force/torque measurements at the robot end-effector, which are standard on many industrial robots, without relying on external sensing in the control loop. The challenge is that, unlike rigid-object co-transport, the dynamics of a flexible object distort the interaction force sensed by the robot. As a result, standard admittance control can lead to reduced gain margins, increased deformation, and instability. Large deformations are undesirable because they degrade transport performance and can damage flexible objects. The thesis develops two model-based methods to address this problem. First, a dynamics-compensated admittance controller improves within-trial co-transport performance by compensating for the flexible-object dynamics. Experimental results show a 45% reduction in RMS deformation compared to standard admittance control while allowing higher effective admittance without loss of stability. Second, for repeated co-transport tasks, a dynamics-based estimator reconstructs human motion from measured interaction force and robot motion, and this estimate is used to iteratively correct the admittance-controller error across trials. Experimental results on a UR10e industrial robot platform in a seven-subject preview-tracking study show a 79% reduction in RMS deformation relative to admittance control alone. In the final iterations, the learned motion reduces deformation below the human RMS reference-tracking error. These results show that modeling flexible-object dy-

namics can make force-based co-transport practical without external sensing in the control loop, and provide a basis for low-deformation collaborative manipulation on industrial robot platforms.

ACKNOWLEDGMENTS

This dissertation would not have been possible without the many people who have supported me throughout my academic journey. I am grateful to the staff, faculty, and fellow students who have helped me along the way through all three of my mechanical engineering degrees. I would like to thank my committee members, Professor Joseph Garbini, Professor Taghvaei, and Dr. Lance McCann, for their guidance and support. I would also like to thank my current and former lab mates in the Precision Controls Lab for their friendship, encouragement, and support.

I am grateful to my colleagues in the Boeing Advanced Research Center for sharing their vast practical knowledge and experience with me. Thank you to my family and friends for understanding my busy schedule and supporting me throughout this work.

Finally, I would like to express how deeply fortunate I have been to work with Professor Santosh Devasia over the last eight years, from my undergraduate studies to the completion of this dissertation. His patience, encouragement, and profound knowledge have shaped me both personally and professionally.

TABLE OF CONTENTS

Page

List of Figures . . . iii

List of Tables . . . vii

NOMENCLATURE . . . viii

Chapter 1: Introduction . . . 1
1.1 Motivating Example . . . 2
1.2 Research Goal and Contributions . . . 8
1.3 Thesis Organization . . . 10

Chapter 2: Background and Related Work . . . 12
2.1 Multi-robot Object Transport . . . 12
2.2 Admittance Control . . . 13
2.3 Vision-Based Flexible-object Transport . . . 16
2.4 Iterative Learning for Repeated Physical Interaction Tasks . . . 16
2.5 Conclusion . . . 17

Chapter 3: MC1: Improving Human-Robot Co-Transport Performance by Correcting for Flexible Object Dynamics . . . 19
3.1 Problem Statement . . . 19
3.2 Control Architecture . . . 21
3.3 Proposed Approach . . . 26
3.4 Experiment . . . 28
3.5 Results . . . 29
3.6 MC1: Conclusion . . . 30

Chapter 4: MC2: Iterative Learning for Flexible Object Co-Transport 32
4.1 Introduction 32
4.2 Problem Formulation 34
4.3 Proposed Approach 39
4.4 Experimental Methods 45
4.5 Experimental Results 53
4.6 MC2: Conclusion 57

Chapter 5: Conclusion and Future Work 60
5.1 Summary 60
5.2 Future Work 61

Bibliography 65

Appendix A: Experimental Platform 71
A.1 Force Sensor 73
A.2 Robot Platform 73
A.3 Motion Capture and Coordinate Transformation 77

Appendix B: Online Human Position Estimation 79
B.1 Model-Error Sensitivity 81
B.2 Perturbation Simulation 81

Appendix C: Baseline-Model Simulation Study 88

LIST OF FIGURES

Figure Number | Page

1.1 A flexible ring structure is held by a robot gripper and a human partner. . . 2
1.2 Diagram of a flexible structure modeled as two masses connected by springs and dampers. 4
1.3 Block diagram of the closed-loop system integrating the flexible structure, admittance controller, and robot dynamics. 6
1.4 Stability maps of the closed-loop system with (a) the G_{x_r} two-mass-spring-damper flexible model, and (b) $G_{x_r} = K_{eq}$. Green denotes stable parameters and red denotes unstable parameters. 7
1.5 Contour plots of maximum error for a 0.4 Hz sinusoid with amplitude 1.00 for (a) the G_{x_r} two-mass-spring-damper flexible model, and (b) $G_{x_r} = G_{x_h} = K_{eq}$. 8
1.6 Research questions and main contributions in the thesis. 9
2.1 Research gap addressed by the thesis. 18
3.1 Experimental setup from above. The positions x_h and x_r are detected from an external motion capture system. 20
3.2 Closed-loop block diagram of robot control with a flexible structure. 21
3.3 Robot controller experimental frequency response and its fit, $G_r(j\omega) = \frac{V_r(j\omega)}{V_{r,d}(j\omega)}$. 22
3.4 Flexible beam experimental frequency response and its fit, $G_{x_r}(j\omega) = \frac{F(j\omega)}{X_r(j\omega)}$. 23
3.5 Diagram of flexible structure with two masses. 24
3.6 Simulated RMS deformation with standard control method, $C(s) = Y(s)$ for varying parameters. White areas are unstable. 25
3.7 Raw data and the model, $\hat{G}_{x_r}$ 26
3.8 Simulated RMS deformation with proposed (inverse-model) control method, $C(s) = Y(s)\hat{G}_{x_r}^{-1}(s)$ for varying parameters. White areas are unstable. 27
3.9 Experimental setup showing the on-screen reference trajectory (black rectangle) and the robot cursor (red), both displayed in pixel coordinates. 28

3.10 Summary of steady-state performance metrics. (a) Normalized root-mean-square beam deformation, δ_{rms}. (b) High-frequency vibration energy, P, integrated from 2 Hz to the Nyquist frequency. 30

3.11 Time series at the highest stable gain setting. Inverse-model compensation (blue) yields lower peak deformation and reduced force compared to baseline admittance control (black). 31

4.1 Overview of co-transport with admittance control. The UR10e robot grasps one end of the flexible object and measures interaction force/torque f using a force/torque (F/T) sensor while a human grasps the opposite end. The reference trajectory x_{ref} is displayed using the preview-tracking interface shown in Fig. 4.5, and the user attempts to track the provided reference. The interaction (admittance) controller generates desired robot motion $x_{r,d}$ from the measured force f. A motion capture system (MOCAP) measures positions on the flexible structure for performance analysis, but is not used for control. . 35

4.2 Block diagram of object co-transport with feedforward control u_c. The human motion and robot motion are mapped to force f through G_{x_h} and G_{x_r}, respectively. u_h is the integral of the admittance-controller Y output. The desired robot position $x_{r,d}$ is realized through the robot's internal controller G_r. F/T represents the force/torque sensor. 38

4.3 Experimental co-transport results with standard admittance control. (Left) Large differences between the robot position x_r and human position x_h leading to large flexible-object deformation, $\delta = x_h - x_r$. (Right) Error in estimating human position x_h from experimental data. Top: Spring-based estimated human position $\hat{x}_{h,spring}$ (dashed line) using Eq. (4.12) compared to measured human position x_h using MOCAP (solid line) Bottom: Error $e_{spring} = x_h - \hat{x}_{h,spring}$ in the spring-based estimate $\hat{x}_{h,spring}$ of human position. 39

4.4 Experimental setup for flexible-object co-transport. The UR10e grasps one end of the flexible object and measures interaction force/torque at the wrist while a human grasps the opposite end and repeats the task across iterations. A preview-tracking display is placed in front of the subject, and the subject attempts to track the moving reference with a five-second preview of the upcoming trajectory. 46

4.5 Preview-tracking display used in the iterative co-transport experiments. The blue marker shows the current human position x_h, the red square shows the current reference position x_{ref}, and the red curve shows the next 5 s of the reference trajectory. 48

4.6 Experimental data (dots) and identified model (lines) of: (left column) flexible-object dynamics $\hat{G}_{x_r}(j\omega)$ mapping robot position to measured force; and (right column) flexible-object dynamics $\hat{G}_{x_h}(j\omega)$ mapping human position to measured force. 49

4.7 Model uncertainty Δ_{ff} in magnitude and phase of $G_{ff}(j\omega)$ in Eq. (4.32) (top, middle). Maximum theoretical learning gain $\bar{\rho}$ from Eq. (4.33) (bottom, triangles) and chosen learning gain (bottom, circles). 54

4.8 Estimate of human motion, $\hat{x}_h$, using dynamics-based estimate in (4.14), and lumped spring-based estimate $\hat{x}_{h,spring}$ in (4.12): (left) for the first iteration (top) and final iteration (bottom); and (right) RMS estimation error over iteration steps k across the $N_u = 7$ subjects. Error bars denote the standard deviation across trials at each iteration. 55

4.9 Object deformation. Left: human position x_h and robot position x_r for the first iteration (top) and final iteration (bottom). Right: RMS deformation over iteration steps k across the $N_u = 7$ subjects; error bars denote the standard deviation across trials at each iteration of deformation $\delta = x_h - x_r$. . . 57

4.10 Human reference-tracking error. Left: human position x_h (from motion capture) vs. previewed reference trajectory x_{ref} for the first iteration (top) and final iteration (bottom). Right: RMS reference-tracking error $x_h - x_{ref}$ over iteration steps k across the $N_u = 7$ subjects; error bars denote the standard deviation across trials at each iteration. 58

A.1 Block diagram of the experimental pHRI platform. A human operator and a 6-DOF robot jointly manipulate a flexible object. The interaction force $\boldsymbol{F}$ sensed at the robot wrist is processed by an interaction controller that outputs a Cartesian reference velocity $\boldsymbol{v}_{r,d}$. The inverse Jacobian converts $\boldsymbol{v}_{r,d}$ to joint-space commands $\dot{\boldsymbol{\theta}}_d$, which are executed by the robot's internal velocity loops to realize the end-effector velocity $\boldsymbol{v}_r$. A marker-based motion-capture system records human and robot kinematics for offline analysis. 71

A.2 Labeled robot platform showing: (a) the end effector with gripper, motion capture markers, and force/torque sensor, and (b) the UR10e robot in its home position. 72

A.3 Block diagram of robot motion controller model. 74

A.4 Step response of the robot velocity controller. The robot is initially moving at 2.5 cm/s and is commanded to a 5.0 cm/s velocity. The velocity is based on the numerical differentiation of joint angles, so the step response is noisy. 75

A.5 Robot velocity tracking at different frequencies. 75

A.6 Frequency response of the robot controller, $G_r(j\omega)$. 76

A.7 Illustration of the robot and motion capture coordinate frames. 77

B.1 Online human-position-estimation controller. The red model path shows where $\hat{G}_{x_r}$ is used to reconstruct $\hat{X}_h$ from the measured force and robot motion. The controller then subtracts the measured robot position X_r directly. Model mismatch leaves the residual $G_{x_r} - \hat{G}_{x_r}$ inside the closed-loop characteristic equation. 80
B.2 Open-loop gain-margin comparison for the online estimator with a fixed fourth-order, 4 Hz Butterworth command filter. Black denotes the exact-model loop and red denotes the 2.0% pole-frequency perturbation. The exact-model loop has $\gamma_{\max} = 14.37$, while the perturbation reduces the allowable gain to $\gamma_{\max} = 4.68$. 83
B.3 Closed-loop 0.5 Hz tracking comparison using $\gamma = 0.9\gamma_{\max}$ for each case. The top panel shows exact-model tracking, the middle panel shows tracking with the 2.0% pole-frequency perturbation, and the bottom panel compares the resulting deformation $x_h - x_r$. The exact-model case has 18.07% RMS deformation because the command filter and finite gain remain in the loop, while the perturbation increases the RMS deformation to 50.94%. 85
B.4 Effect of uniform pole-frequency error on online tracking deformation with the fixed fourth-order, 4 Hz Butterworth command filter. Each point recomputes the open-loop gain margin of (B.9), sets $\gamma = 0.9\gamma_{\max}$, and evaluates the normalized 0.5 Hz RMS deformation from (B.13). 86

C.1 Closed-loop simulation architecture for the baseline-model sweep. The flexible-object model maps human and robot motion to the force measured at the robot wrist. The controller block is set to standard admittance, $C(s) = Y(s)$, or to the MC1-style inverse-compensated controller, $C(s) = Y(s)\hat{G}_{x_r}^{-1}(s)$. 89
C.2 Baseline-model natural-frequency sweep for a 0.5 Hz sinusoidal human input. The cutoff is fixed at $\omega_c = 10$ rad/s, and each point uses 90% of the largest stable gain in the controller grid to provide gain margin. The dotted vertical line marks the nominal MC1 object frequency. At the nominal object frequency, MC1 reduces the simulated RMS deformation from about 10.0% to 4.1%. When the flexible mode moves into the low-frequency range relevant to voluntary motion, both within-trial controllers produce large deformation. . . 91

LIST OF TABLES

Table Number Page

4.1 Human-position estimation error corresponding to the right panel of Fig. 4.8. Entries are mean ± standard deviation across trials, reported in centimeters. 56

4.2 RMS deformation and human reference-tracking error corresponding to the right panels of Figs. 4.9 and 4.10. Entries are mean ± standard deviation across trials, reported in centimeters. 59

NOMENCLATURE

KEY VARIABLES:

x'_h: Physical human-side grasp position before removal of the undeformed offset.

x_h: Offset-corrected human-side grasp position, $x_h = x'_h - x_0$.

$\hat{x}_h$: Dynamics-based estimate of the human-side grasp position.

x_r: Robot-side position.

x_0: Fixed separation between the human and robot grasp coordinates in the undeformed configuration.

x_{ref}: Previewed reference trajectory shown to the human subject.

δ: Flexible-object deformation, $\delta = x'_h - x_r - x_0 = x_h - x_r$. Note that $x_h = x_r$ denotes zero deformation, not the same grasp points.

e_k: Human-robot tracking error during iteration k.

$\hat{e}_k$: Estimated tracking error used by the learning update.

$u_{c,k}$: Learned feedforward correction applied during iteration k.

F, f: Interaction force measured at the robot end-effector along the task axis.

DYNAMICS AND MODELS:

$Y(s)$: Standard admittance dynamics used in the interaction controller.

$G_r(s)$: Robot motion-controller dynamics.

$G_{x_h}(s)$: Map from human-side motion to robot-side measured force.

$G_{x_r}(s)$: Map from robot-side motion to robot-side measured force.

$\hat{G}_{x_h}(s)$: Identified model of $G_{x_h}(s)$.

$\hat{G}_{x_r}(s)$: Identified model of $G_{x_r}(s)$.

$G_{ff}(s)$: Feedforward path from learned correction to robot motion.

$\hat{G}_{ff}(s)$: Identified feedforward-path model used in the iterative update.

$\Delta_{ff}(s)$: Multiplicative feedforward-model error $G_{ff}(s)/\hat{G}_{ff}(s)$.

$W(\omega)$: Magnitude of the iteration error multiplier in the convergence bound.

CONTROLLER PARAMETERS:

K_{eq}, k_{eq}: Equivalent low-frequency stiffness of the flexible object.

α: Admittance gain.

γ: Tracking gain in the ideal and online-estimator controllers.

$\rho(\omega)$: Frequency-dependent iteration gain used in the learning update.

ω_c: Admittance-filter cutoff frequency in radians per second.

N_u: Number of human subjects in the multi-user study.

ABBREVIATIONS:

F/T: Force/torque.

FRF: Frequency response function.

MC1: Main Contribution 1.

MC2: Main Contribution 2.

pHRI: Physical human-robot interaction.

RMS: Root mean square.

Chapter 1

INTRODUCTION

Collaborative robots are increasingly used in settings where humans and robots work in close physical proximity [1]. These systems combine human judgment and adaptability with robot precision, payload capacity, and repeatability, making them useful across manufacturing, logistics, and other industrial tasks. One application across these domains is object co-transport, where a human and robot jointly grasp and move an object. Object co-transport has been extensively explored in the literature for rigid objects [2–9]. Recently, there has been growing interest in the human-robot transport of flexible objects [10–16]; however, these approaches typically rely on external sensing, including motion capture and cameras. Relying on external sensing increases system complexity and can be challenging to deploy in many real-world applications. Industrial robots, by contrast, are often already equipped with end-effector force/torque (F/T) sensing that can be used directly for object transport tasks. When handling flexible structures, however, existing force-based methods can lead to large deformation or instability. The primary objective of this thesis is to reduce deformation during flexible-object co-transport using measured interaction force and robot motion, without direct human-motion feedback in the controller.

This thesis addresses the challenge of force-based collaborative transport of flexible objects through two approaches. First, flexible-object dynamics are incorporated directly into the admittance controller through inverse-model compensation so that the robot can operate with higher effective admittance while maintaining stability. Second, for repeated co-transport tasks, human motion is inferred from measured interaction force and robot motion, and this estimate is used in an iterative learning framework to improve coordination across trials.

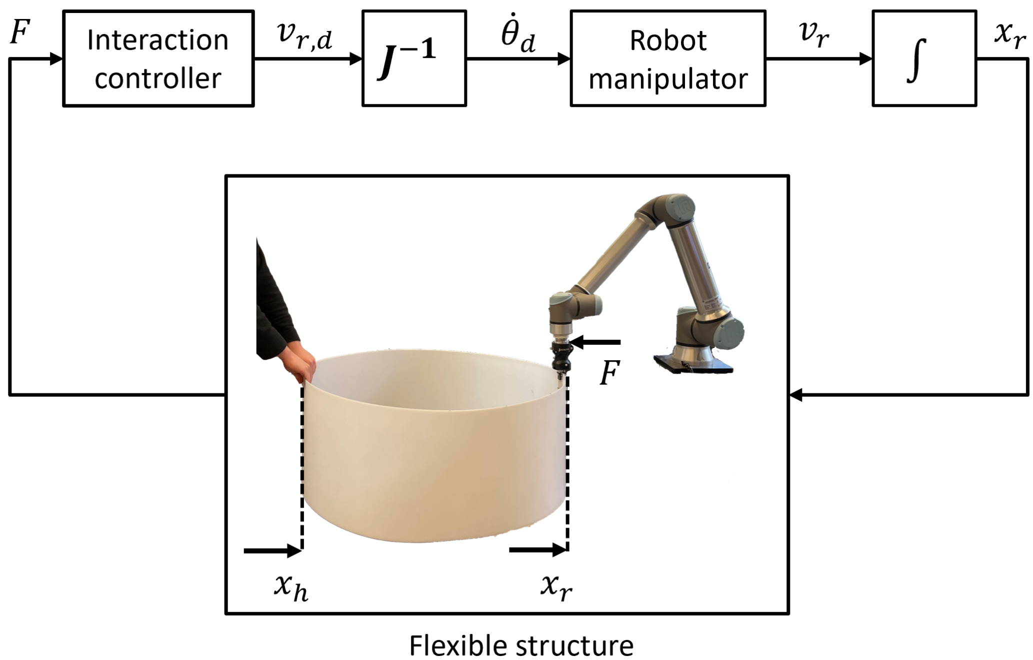

Figure 1.1: A flexible ring structure is held by a robot gripper and a human partner.

1.1 Motivating Example

Consider a scenario in which a human operator holds one end of a flexible structure while a robotic partner grasps the opposite end. The offset-corrected human position, x_h, induces forces in the object that are measured by a force sensor at the robot's end effector. In the ideal case, the object acts as a simple spring element and $F = K_{eq}(x_h - x_r)$, where K_{eq} is the equivalent lumped stiffness. These forces, F, generate the desired robot Cartesian velocities, $v_{r,d}$, through an interaction controller. Joint velocities are calculated using the inverse manipulator Jacobian and passed to the robot's internal velocity controllers. The aim during flexible-object transport is to minimize the deformation, defined in physical coordinates as $\delta = x'_h - x_r - x_0$, where x_0 is the fixed separation of the grasp coordinates in the undeformed state. For notational convenience, define $x_h = x'_h - x_0$, giving $\delta = x_h - x_r$. Note that $x_h = x_r$ denotes zero deformation; the physical grasp points remain separated by

x_0. The origin is selected so that $x_h = x_r = 0$ in the initial undeformed configuration. The goal is to design an interaction controller that minimizes deformation subject to the robot motion-controller dynamics and the flexible-structure dynamics. The following subsections describe the main blocks in Fig. 1.1.

1.1.1 Interaction Controller

Consider an ideal controller for the robot to achieve exponential tracking of the human user,

$$\dot{x}_r(t) = -\gamma[x_r(t) - x_h(t)] + \dot{x}_h(t) \tag{1.1}$$

where γ is the controller gain. In this case, exponential tracking is achieved and the deformation (error) dynamics are $\dot{\delta}(t) = -\gamma\delta(t)$. Although it is theoretically possible to estimate human velocity with $\dot{x}_h = \dot{x}_r - \frac{\dot{F}}{K_{eq}}$, real force measurements are noisy and using its derivative in this manner is not practical [17]. The human velocity $\dot{x}_h(t)$ cannot be directly sensed, so the following control law is used,

$$\begin{aligned}
\dot{x}_r &= -\gamma[x_r(t) - x_h(t)] && (1.2)\\
&= \frac{\gamma}{K_{eq}}F(t) && (1.3)\\
&= \alpha F(t) && (1.4)
\end{aligned}$$

where α is defined as the controller gain. The deformation dynamics become $\dot{\delta}(t)+\gamma\delta(t) = \dot{x}_h(t)$. Since measured force signals are noisy, the control law is filtered. In the Laplace domain, the control law is

$$V_r(s) = \alpha\frac{\omega_c}{s+\omega_c}F(s) = \frac{1}{m_a s + b_a}F(s). \tag{1.5}$$

where ω_c is the cutoff frequency of the first-order low-pass filter in radians/s and s is the Laplace variable. This is equivalent to a standard admittance controller that is commonly used in pHRI and for rigid-object co-transport (see Chapter 2). The equivalent mass and damping of the admittance controller are $m_a = \frac{1}{\omega_c \alpha}$ and $b_a = \frac{1}{\alpha}$.

1.1.2 Flexible Structure

The dynamics of the flexible object are modeled using a two-mass system, as depicted in Fig. 1.2. In the Laplace domain, the relationship between the applied force and the displacements is given by

$$F(s) = -G_{x_r}(s)X_r(s) + G_{x_h}(s)X_h(s), \tag{1.6}$$

with the transfer functions defined as

$$G_{x_r}(s) = m_2 s^2 + k_2 + c_2 s - \frac{(k_2 + c_2 s)^2}{D(s)}, \tag{1.7}$$

$$G_{x_h}(s) = \frac{(k_2 + c_2 s)(k_1 + c_1 s)}{D(s)}, \tag{1.8}$$

$$D(s) = m_1 s^2 + (c_1 + c_2)s + (k_1 + k_2). \tag{1.9}$$

A detailed derivation of this model is provided in Chapter 3.

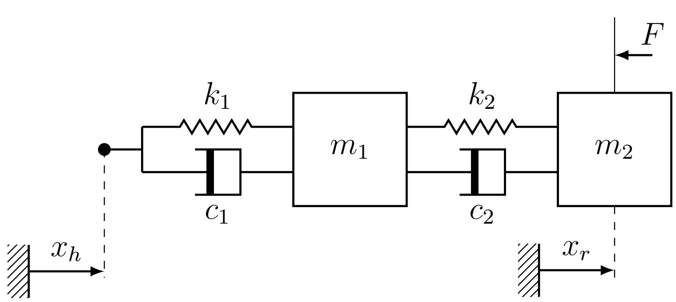

Figure 1.2: Diagram of a flexible structure modeled as two masses connected by springs and dampers.

1.1.3 Robot Manipulator

Fig. 1.3 illustrates the closed-loop architecture of the velocity-controlled robot, which receives desired TCP velocity commands $V_{r,d}$ and employs internal control loops to generate motion. In many industrial applications, the robot's proprietary control system precludes access to a detailed dynamical model. We simplify the system by assuming that the motion controller, R_c, operates as a high-gain proportional-integral (PI) controller, while the robot's inherent dynamics, R_d, can be approximated by a mass-damper system. The influence of the applied forces F on the robot dynamics is assumed to be negligible due to the high gear ratios and gains typically used in industrial robots.

The robot dynamics are modeled as

$$R_d(s) = \frac{1}{m_r s + b_r}, \tag{1.10}$$

and the controller is described by

$$R_c(s) = \frac{K_i}{s} + K_p, \tag{1.11}$$

where K_i and K_p denote the controller gains, and m_r and b_r represent the effective mass and damping, respectively. An actuation delay, τ_d, is incorporated using a first-order Pade approximation. This leads to the closed-loop robot dynamics:

$$G_r(s) = \frac{V_r(s)}{V_{r,d}(s)} = \frac{2 - \tau_d s}{2 + \tau_d s} \frac{K_p s + K_i}{m_r s^2 + (K_p + b_r)s + K_i}. \tag{1.12}$$

1.1.4 Closed Loop System

The overall closed-loop system, which integrates the robot controller, the robot dynamics, and the flexible structure, is depicted in Fig. 1.3. In our analysis, we focus on forces and motions along a single axis. Given that the stiffness of the human arm is typically greater than 2000 N/m [18] and that industrial robot manipulators are much stiffer than the object, the flexible object dynamics (with effective stiffness $K_{eq} < 200$ N/m) dominate the interaction. As a result, the intrinsic stiffness of both the human operator and the robot is neglected.

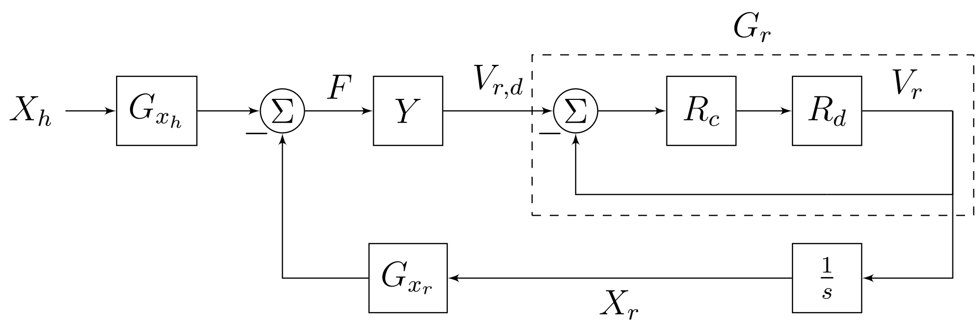

Figure 1.3: Block diagram of the closed-loop system integrating the flexible structure, admittance controller, and robot dynamics.

The closed-loop dynamics from the human input to the robot output can be expressed as

$$\frac{X_r(s)}{X_h(s)} = \frac{G_{x_h}(s)\, G_r(s)\, Y(s)}{s + G_{x_r}(s)\, G_r(s)\, Y(s)}, \tag{1.13}$$

and the deformation transfer function is defined by

$$T(s) = \frac{\delta(s)}{X_h(s)} = 1 - \frac{X_r(s)}{X_h(s)}. \tag{1.14}$$

The objective is to minimize the deformation (i.e., to ensure $\frac{X_r(s)}{X_h(s)} \approx 1$) over the range of expected human motion. Since the bandwidth of human voluntary movements is typically limited to approximately 2 Hz [19], the controller is designed to reduce object deformation within this frequency range.

1.1.5 Stability and Performance Analysis

An analytical expression for stability of this system in terms of the admittance parameters is challenging to derive because of the complexity of the roots of the characteristic polynomial

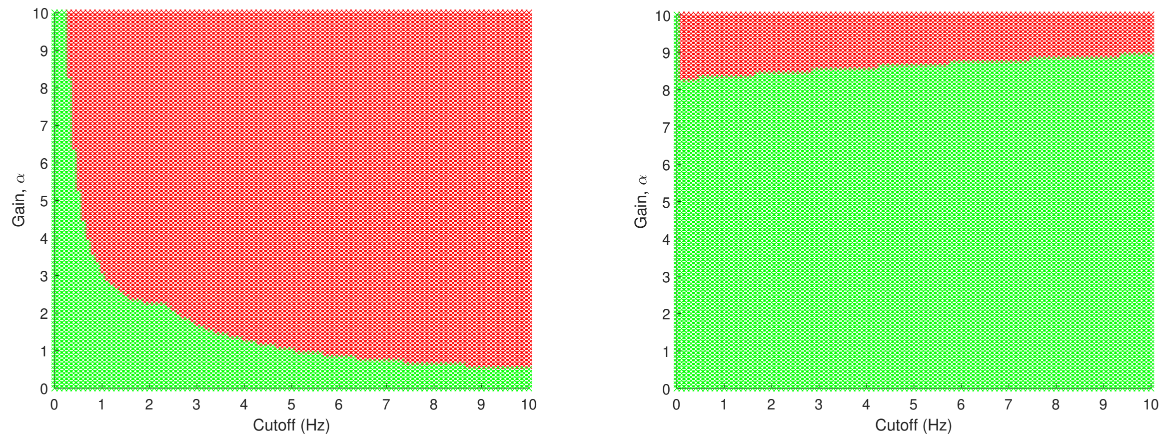

(a) With object dynamics

(b) Without object dynamics

Figure 1.4: Stability maps of the closed-loop system with (a) the G_{x_r} two-mass-spring-damper flexible model, and (b) $G_{x_r} = K_{eq}$. Green denotes stable parameters and red denotes unstable parameters.

of $T(s)$. Using fixed model parameters in (1.13), the admittance gain and cutoff (α, ω_c) are varied, and stability and performance of the system are found numerically. The robot dynamics and controller parameters fit from the experimental system are $m_r = 4.5$, $b_r = 50$, $K_i = 250000$, and $K_p = 200$. The structural dynamics are $m_1 = 0.0255$ kg, $k_1 = 12$ N/m, $c_1 = 0.04$ N $\cdot$ s/m, $m_2 = 0.008$ kg, $k_2 = 39$ N/m, and $c_2 = 0.07$ N $\cdot$ s/m. The poles of $T(s)$ are computed numerically for $\omega_c, \alpha \in [0, 10]$ using 0.1 increments. The system is considered unstable if any pole is in the closed right-half plane.

The plots in Fig. 1.4 illustrate the destabilizing effect of the flexible structure. With flexible-object dynamics included, the stable region becomes smaller. Lower filter cutoffs and lower gains are therefore required to stabilize the system, which increases deformation. These results indicate that, under the assumptions of the two-mass flexible-structure model, compensating for these dynamics can improve system performance.

We simulate $T(s)$ for a sinusoidal input, $x_h(t) = \sin(2\pi f t)$, with frequency $f = 0.4$ Hz for

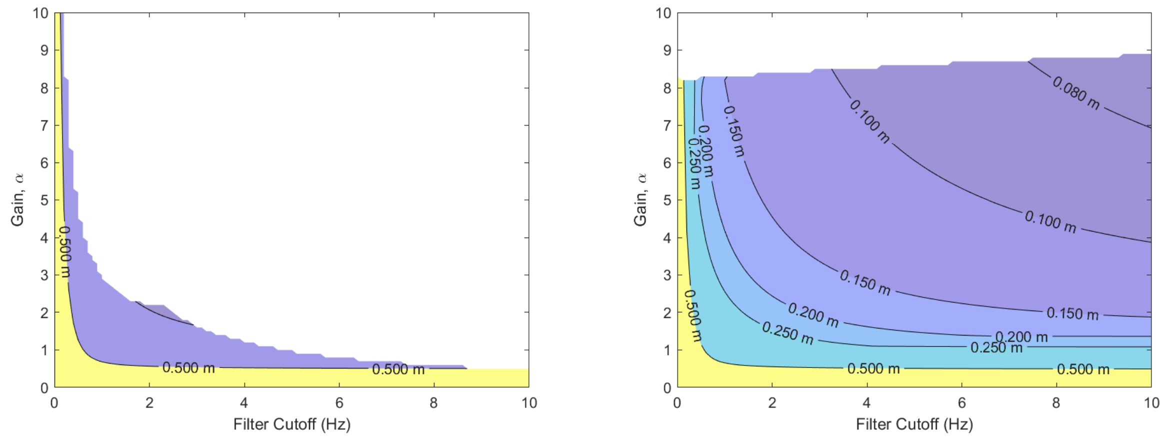

(a) With object dynamics (b) Without object dynamics

Figure 1.5: Contour plots of maximum error for a 0.4 Hz sinusoid with amplitude 1.00 for (a) the G_{x_r} two-mass-spring-damper flexible model, and (b) $G_{x_r} = G_{x_h} = K_{eq}$.

10 cycles and a sampling time of 2 ms. The maximum deformation contours are plotted in Fig. 1.5. The object dynamics increase the minimum achievable deformation in Fig. 1.5(a). Without object dynamics, the controller can use higher effective admittance and thereby reduce deformation during interaction. The remainder of this thesis develops tools to identify and compensate for flexible-structure dynamics to reduce deformation.

1.2 Research Goal and Contributions

1.2.1 Research Questions

RQ1: How Can Deformation Be Reduced During Force-Based Human-Robot Co-Transport of Flexible Structures?

Standard admittance control provides a practical force-based interface for pHRI, but flexible-object dynamics reduce stability margins and force the controller to operate at lower effective admittance. The first research question is therefore how to compensate those dynamics so

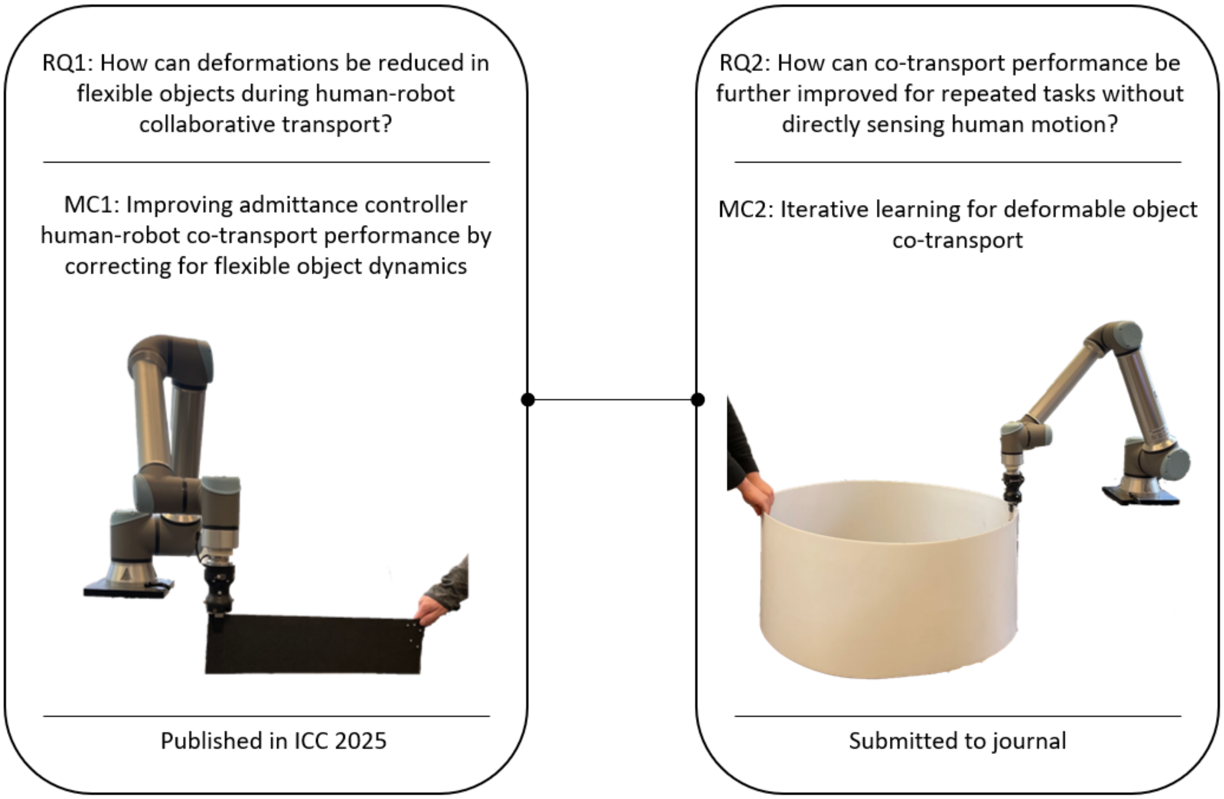

Figure 1.6: Research questions and main contributions in the thesis.

that deformation is reduced while preserving stable interaction.

RQ2: How Can Co-Transport Performance Be Further Improved for Repeated Tasks Without Directly Sensing Human Motion?

For repeated co-transport tasks, the robot should ideally use prior executions to improve coordination with the human. However, in the intended deployment setting the robot measures only end-effector force/torque and its own motion. This motivates three supporting questions:

1. RQ2.1: How can human motion be estimated from measured force and robot motion using flexible-object dynamics?

2. RQ2.2: How can this estimate be used to construct a stable iterative update that improves performance across trials?

3. RQ2.3: Can repeated interaction reduce deformation below the human reference-tracking error?

1.2.2 Main Contributions

- **MC1:** A dynamics-compensated admittance controller is developed by augmenting standard admittance control with an approximate inverse model of the flexible-object dynamics. This compensation increases the achievable effective admittance while preserving stable interaction, and reduces RMS deformation by 45% in human-subject experiments.

- **MC2:** A dynamics-based human-motion estimator and iterative learning framework are developed for repeated flexible-object co-transport tasks using only measured force and robot motion in the control loop. Across repeated trials in a seven-subject preview-tracking study, object deformation is reduced by 79%, and the final learned motion reduces deformation below the human RMS reference-tracking error.

1.3 Thesis Organization

The remainder of this document is organized as follows. Chapter 2 reviews related work on co-transport, admittance control, model-based compensation, vision-based flexible-object manipulation, parameter estimation, and iterative learning. Chapter 3 presents the first main contribution: a dynamics-compensated admittance controller for reducing deformation during flexible-object co-transport. Chapter 4 presents the second main contribution: a dynamics-based human-motion estimator together with an iterative learning framework for repeated co-transport tasks. Chapter 5 concludes the thesis with a summary of the main findings and directions for future work. Appendix A describes the experimental platform, robot model identification, and motion-capture calibration used for evaluation. Appendix B analyzes the robustness of using the human-position estimator as an online controller, and Appendix C simulates the performance of inverse-model compensation for different flexible-mode frequencies.

Chapter 2

BACKGROUND AND RELATED WORK

This chapter reviews the literature relevant to MC1 and MC2 and identifies the research gap addressed by the thesis.

2.1 Multi-robot Object Transport

The human-robot co-transport problem is closely related to multi-robot object transport because, in both cases, multiple agents must coordinate through a shared object. Multi-robot transport can be centralized, with explicit communication among agents, or decentralized, in which coordination occurs through local sensing and the object itself. In a human-robot team, explicit communication of intent is much harder to assume than in a robot network and often requires specialized interfaces such as electromyography (EMG) sensing [20] or invasive neural interfaces [21]. Therefore, the literature on decentralized leader-follower transport is more relevant for this thesis. In this case, the human plays the role of the leader, and the follower robot must infer how to respond from the interaction through the object [22].

Several decentralized methods coordinate robots through the forces and motion transmitted by a shared rigid load. Local contact-force feedback has been used to follow a leader or regulate object motion and internal force without exchanging position or force data [23–25]. These methods use only local force measurements (along with the follower's own position and velocity) and therefore avoid explicit online communication, but assume that the transported object is rigid.

Delayed self-reinforcement (DSR) extends this force-based approach to flexible-object transport [26–28]. The leader follows the desired trajectory, while each follower uses its measured force and delayed position and force measurements to update its motion. Experiments using mobile robots [26] and industrial robot manipulators [27,28] show that DSR can reduce deformation without direct robot-to-robot communication. This DSR update also applies to one leader and one follower and does not require explicit measurement of the leader trajectory. However, the controller design and stability analysis assume a linear stiffness relation between measured forces and displacements; the dynamics of the object are neglected. The reported transport trajectories are also slow, on the order of 1 cm/s in the experiments using industrial robots [27, 28]. This speed is much lower than the prescribed peak speeds used in the human co-transport experiments in this thesis, which are on the order of 30 cm/s. In this thesis, the measured force is instead described by object dynamics that include flexible modes. A stiffness approximation is appropriate when the task bandwidth lies well below the flexible modes, but not when those modes lie within the task bandwidth.

2.2 Admittance Control

2.2.1 Admittance Control Fundamentals

Admittance control is the standard way to realize compliant interaction on non-backdrivable industrial manipulators with wrist force/torque sensors [29, 30]. Impedance control maps imposed motion to commanded force, whereas admittance control maps measured external force to commanded motion. In co-transport problems this means that the robot motion is generated directly from the interaction force, which is appealing when human motion is not measured explicitly.

The general form of an admittance controller is

$$\frac{X_r(s)}{F(s)} = \frac{1}{M_a s^2 + B_a s + K_a}, \tag{2.1}$$

where X_r denotes robot motion, F denotes measured interaction force, and M_a, B_a, and K_a define the desired interaction dynamics. In collaborative carrying tasks, spring terms are often omitted so that the robot does not return to a fixed equilibrium. This gives the commonly used velocity form

$$Y(s) = \frac{V(s)}{F(s)} = \frac{1}{M_a s + B_a}. \tag{2.2}$$

For rigid-object co-carrying, this architecture is often effective because the measured force can be treated as a reasonably direct cue of human intent. For flexible objects, however, the force is filtered by the object dynamics, so the same admittance law must simultaneously interpret human intent and remain stable in the presence of flexible modes. In the broader pHRI literature, admittance design is often discussed from a passivity perspective because passivity gives a sufficient condition for stable interaction under uncertainty. However, passivity can be overly conservative when the goal is high performance: passivity-based approaches can sacrifice performance to maintain stability [31], and passivity covers only a subset of the stable interaction region [32]. For this reason, this thesis does not use passivity as the primary analysis tool. Instead, MC1 and MC2 analyze the closed-loop stability of the identified human-object-robot dynamics directly, since the design objective is to maximize usable admittance while reducing deformation.

2.2.2 Variable Admittance and Load Compensation

Once dynamic interaction starts to limit performance, the existing admittance literature mainly follows two directions. The first is variable or adaptive admittance, where the apparent inertia and damping are changed online to preserve stability [17, 33–35]. In practice, when oscillatory interaction is detected, these methods typically restore stability by lowering the effective admittance, for example by increasing the apparent inertia or damping. That tradeoff can be sensible when the main objective is stable physical interaction. In flexible-object co-transport, however, lowering the effective admittance causes the robot to lag the human more, which generally increases object deformation. Therefore, variable admittance addresses the stability objective but not the deformation objective of this thesis.

The second direction is to compensate dynamics that corrupt the force measured at the robot wrist. In walk-through programming and manual-guidance settings, tool or payload compensation is used so that the measured wrench more accurately reflects the operator input despite the inertia of a rigid attached load [36, 37]. Related work improves the rendered admittance of industrial robots using disturbance observers, inner-loop shaping, damping feedback, or robust control for heavy or unknown loads [3, 38–40]. These approaches show that modeling interaction dynamics can enlarge the usable operating range of admittance control. However, they compensate robot-side or rigid-payload dynamics to recover transparency, manual-guidance quality, or contact stability. MC1 differs in both the dynamics being compensated and the goal: it compensates the flexible object dynamics that couple human motion, robot motion, and measured force during co-transport, and it does so to reduce deformation while maintaining stable force-based interaction.

2.2.3 Admittance Control for Co-Transport

Most human-robot co-transport work has focused on rigid objects [2–9]. In the rigid case, force-based admittance control works well because the interaction force is a relatively direct indicator of the human's intended motion. The robot can therefore use the measured force both to generate motion and to infer how to follow the human without directly sensing human position. This basic force-based view appears throughout rigid-object co-carrying controllers [4–6] and is consistent with collaborative manipulation models used in human-robot interaction [41].

This reasoning does not carry over directly to flexible objects. When the shared object is flexible, the measured force is shaped by the object dynamics over the human-motion bandwidth. As a result, increasing the admittance can excite flexible modes or destabilize the interaction, and the force no longer gives as direct a measure of human motion as it does in the rigid case. Recent human-robot transport work for flexible objects has therefore often relied on motion capture, cameras, or other external sensing to estimate human motion or object deformation more directly [10–12]. Those approaches can improve transport quality, but they do so by changing the sensing modality.

2.3 Vision-Based Flexible-object Transport

The deformable-object manipulation literature often relies on external sensing. In that literature, successful manipulation depends on access to richer state information about the object's shape or deformation, supported by explicit models, planning methods, and perception [13, 42]. Dynamic models for deformable linear objects [43] and model-based co-manipulation frameworks for flexible materials [44] illustrate how such information can be used to improve manipulation when it is available. Highly deformable materials such as cloth and carbon-fiber plies convey little haptic information through the object, so cameras or motion-capture systems are often used to estimate human motion or object geometry directly [13–16].

In [10], a framework for co-transport of objects with arbitrary stiffness is developed. This work uses a hybrid approach that relies on both force sensing and motion capture to identify the object stiffness online. For a perfectly rigid object, standard admittance control is used, while for fully deformable objects, teleoperation via motion capture is used. For objects with intermediate stiffness, the admittance control and teleoperation are blended using a parameter based on object stiffness, which is determined online. Although this method successfully demonstrates deformable object transport, it relies on both a motion capture system and a force/torque sensor rather than a force/torque sensor alone.

2.4 Iterative Learning for Repeated Physical Interaction Tasks

Iterative learning control (ILC) is intended for finite-duration tasks that are repeated under similar conditions [45,46]. Let u_k, y_k, and $e_k = r - y_k$ denote the input, output, and tracking error during trial k. A common update has the form

$$u_{k+1} = Q\left(u_k + Le_k\right), \tag{2.3}$$

where L is the learning filter and Q limits learning in frequency ranges where noise or model uncertainty is large. For a linear plant P and $Q = 1$, the error evolves as $e_{k+1} = (1 - PL)e_k$.

An inverse-model update uses $L = \rho\hat{P}^{-1}$, giving the frequency-by-frequency convergence condition

$$\left|1 - \rho(\omega)\frac{P(j\omega)}{\hat{P}(j\omega)}\right| < 1. \tag{2.4}$$

The iteration gain therefore trades convergence speed against robustness to model error and nonrepeatable disturbances [47]. ILC uses data from a completed trial, which permits noncausal inversion when the update is computed offline. The main requirements are that the task repeats, the initial conditions are sufficiently consistent, and the tracking error is available to the learning controller.

The usual ILC assumption that the reference is known to the controller is relaxed in [48, 49]. In that work, the human sees the desired output and the measured system output, while the machine measures the system output and the human command is supplied through a motion-capture interface. A model of the human response relates the unknown desired output and the visible tracking error to the measured human command. Inverting this model provides an estimate of the human's intended output, which is then used in an inverse-model ILC update. In the force-based object-transport scenario considered in this thesis, the human position is not directly measurable and must be determined from the robot force and position.

2.5 Conclusion

This literature review points to a gap: force-based co-transport is well established for rigid objects, but once the shared object becomes flexible, the same force signal is no longer a direct proxy for human intent. One response in the literature is to lower the admittance or reshape the robot-side dynamics to recover stability. Another is to add cameras or motion capture so that the robot no longer has to rely on force alone. Neither directly addresses flexible-object co-transport using force and robot motion without direct human-motion feedback in the controller. MC1 compensates the flexible-object dynamics to improve performance within a single execution. MC2 uses trial-to-trial learning to further reduce deformation when those dynamics lie within the human-motion bandwidth.

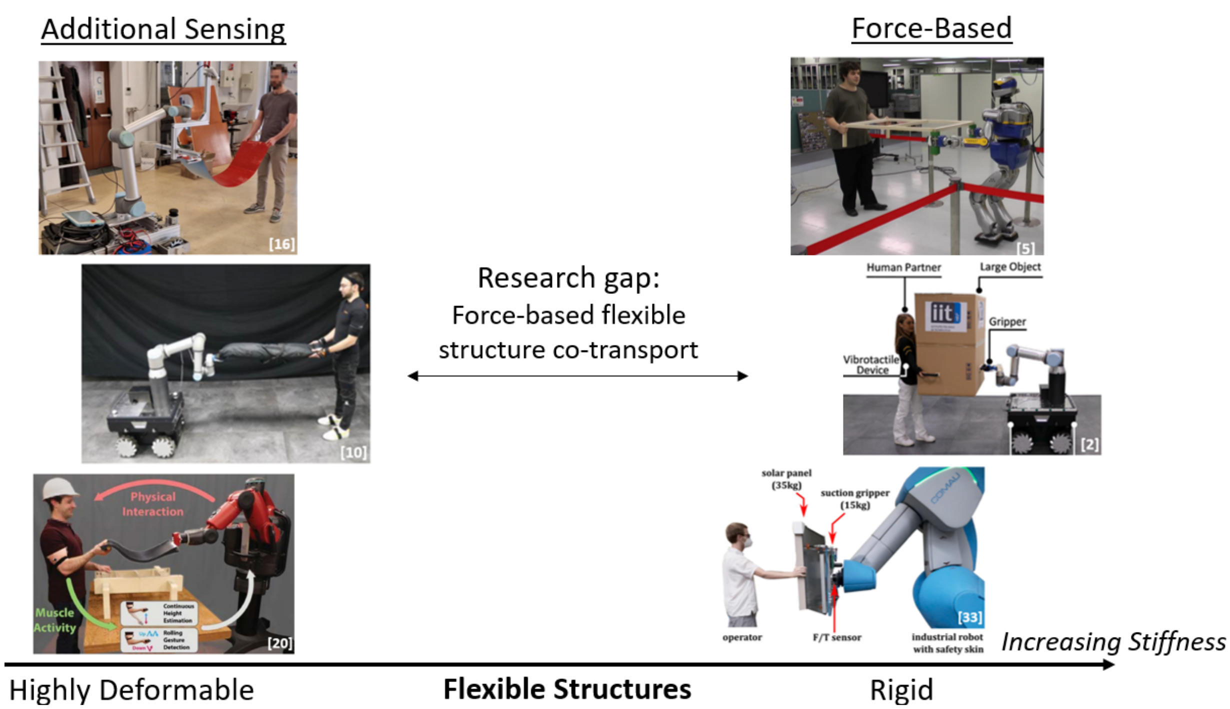

Figure 2.1: Research gap addressed by the thesis.

Chapter 3

MC1: IMPROVING HUMAN-ROBOT CO-TRANSPORT PERFORMANCE BY CORRECTING FOR FLEXIBLE OBJECT DYNAMICS

Chapter 3 develops a dynamics-compensated admittance controller for flexible-object co-transport. It formulates the force-based control problem, identifies the relevant robot and object dynamics, evaluates the controller in simulation, and reports experimental results from a human-subject trial. The chapter is based on work in [50].

3.1 Problem Statement

3.1.1 Ideal Control

Consider the case of a flexible beam with robot motion constrained to one axis. The robot position is x_r and the offset-corrected human position is $x_h = x'_h - x_0$, using the coordinate convention introduced in Chapter 1. The resultant force in the beam due to human and robot movement is measured as F. The control objective is to keep the deformation $\delta = x_h - x_r = x'_h - x_r - x_0$ as small as possible during movement. In particular, $x_h = x_r$ denotes zero deformation after accounting for the undeformed grasp-point separation x_0. In the ideal case, if the human position is known, a controller can be designed for exponential tracking,

$$\dot{x}_r(t) = -\gamma[x_r(t) - x_h(t)] + \dot{x}_h(t) \tag{3.1}$$

where γ is the controller gain. In this ideal case, we achieve the error dynamics $\dot{\delta}(t) = -\gamma\delta(t)$. Although it is theoretically possible to estimate human velocity with $\dot{x}_h = \dot{x}_r - \frac{\dot{F}}{K_{eq}}$, real force measurements are noisy and using its derivative in this manner is not practical [17]. Since $\dot{x}_h(t)$ cannot be directly sensed, we use the following control law,

$$\dot{x}_r = -\gamma[x_r(t) - x_h(t)] \tag{3.2}$$

which has the transfer function

$$\frac{X_r(s)}{X_h(s)} = \frac{\gamma}{s+\gamma} \tag{3.3}$$

and it can be implemented using force feedback and a velocity control as

$$v_r(t) = \dot{x}_r(t) = -\gamma[x_r(t) - x_h(t)] \tag{3.4}$$

$$= \frac{\gamma}{K_{eq}} F(t) \tag{3.5}$$

$$= \alpha F(t) \tag{3.6}$$

where α is defined as the controller gain. In general, the force signal is noisy and therefore a filter is required. The interaction control law in the Laplace domain is then

$$V_r(s) = \alpha \frac{\omega_c}{s+\omega_c} F(s) = \frac{1}{m_a s + b_a} F(s) = C(s)F(s) = Y(s)F(s), \tag{3.7}$$

where ω_c is the cutoff frequency of the first-order low-pass filter in radians/s, s is the Laplace variable, and the control law $C(s)$ is the admittance control $Y(s)$, i.e.,

$$C(s) = Y(s) = \alpha \frac{\omega_c}{s+\omega_c}. \tag{3.8}$$

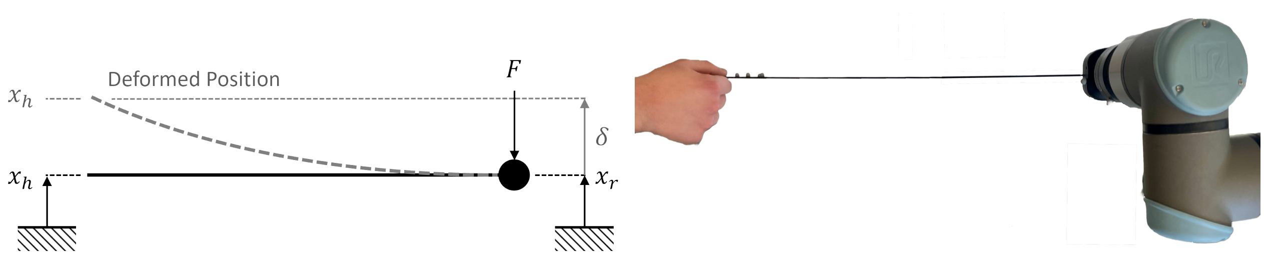

(a) Diagram of experiment (b) Photo of experiment

Figure 3.1: Experimental setup from above. The positions x_h and x_r are detected from an external motion capture system.

This is equivalent to a standard admittance controller commonly used for pHRI, with admittance mass and damping given by $m_a = \frac{1}{\omega_c \alpha}$ and $b_a = \frac{1}{\alpha}$.

Limitation of Ideal Control

The flexible dynamics restrict the value of α that can be achieved while maintaining stability. The sections below derive models for the flexible structure, illustrate the stability limit theoretically and experimentally, and show that compensating for the dynamics can reduce object deformation.

3.2 Control Architecture

The ideal controller is implemented first to show the deformation limits imposed by the flexible object dynamics.

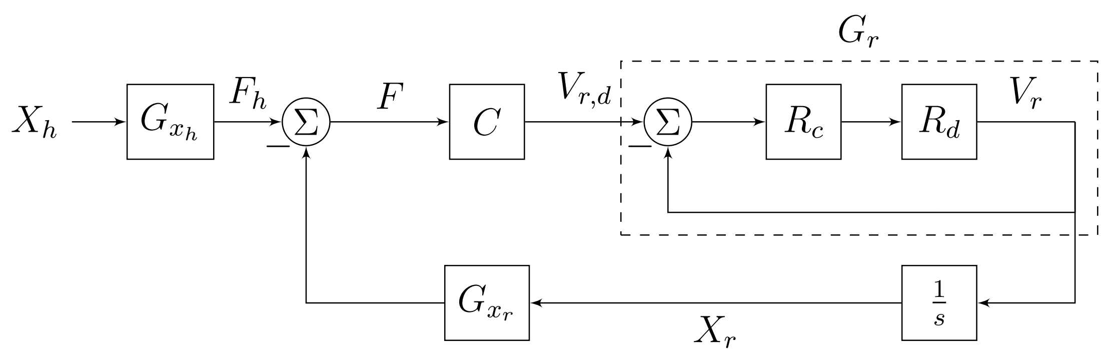

Figure 3.2: Closed-loop block diagram of robot control with a flexible structure.

Fig. 3.2 illustrates the admittance control architecture presented in this chapter. When the human moves the end of the object, a force F_h is generated through the flexible structure modeled by $G_{x_h}(s)$. This force along with that force generated by the robot movement is measured by a sensor mounted on the robot's end-effector and is subsequently provided to the controller $C(s)$, which generates the corresponding reference velocity $V_{r,d}$. The robot's

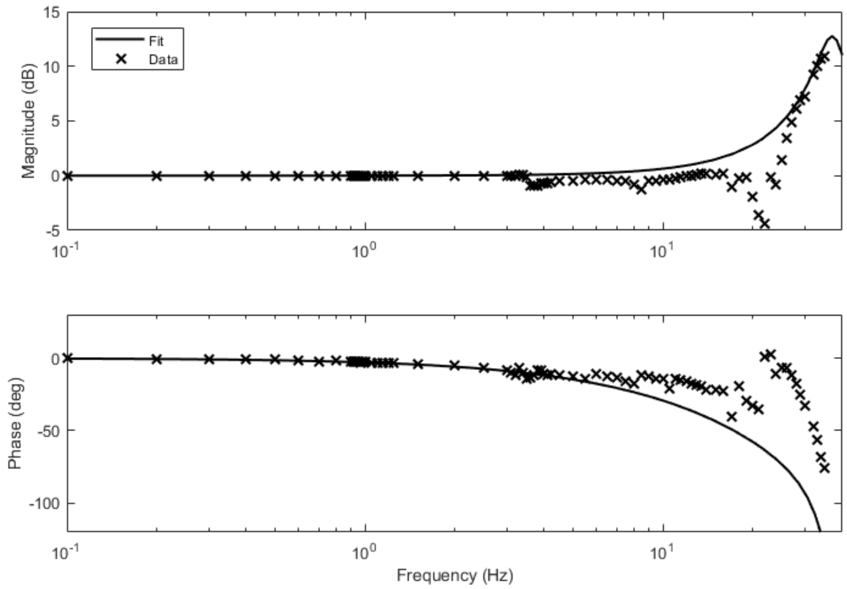

Figure 3.3: Robot controller experimental frequency response and its fit, $G_r(j\omega) = \frac{V_r(j\omega)}{V_{r,d}(j\omega)}$.

motion controller tracks the reference velocity through its internal control loop. The closed loop transfer function is,

$$\frac{X_r(s)}{X_h(s)} = \frac{G_{x_h}(s)G_r(s)C(s)}{s + G_{x_r}(s)G_r(s)C(s)}. \tag{3.9}$$

The following subsections describe the blocks in Fig. 3.2.

3.2.1 Robot Dynamics

The robot model is experimentally obtained along the x-axis for a specific joint configuration. The motion controller is assumed to be robust to forces acting on the end-effector, so these forces are neglected in the robot model. The transfer function between the commanded velocity $V_{r,d}$ and the measured velocity V_r is

$$G_r(s) = \frac{-44.44\, s^2 - 4.444 \times 10^4\, s + 1.389 \times 10^7}{s^3 + 305.6\, s^2 + 6.944 \times 10^4\, s + 1.389 \times 10^7} \tag{3.10}$$

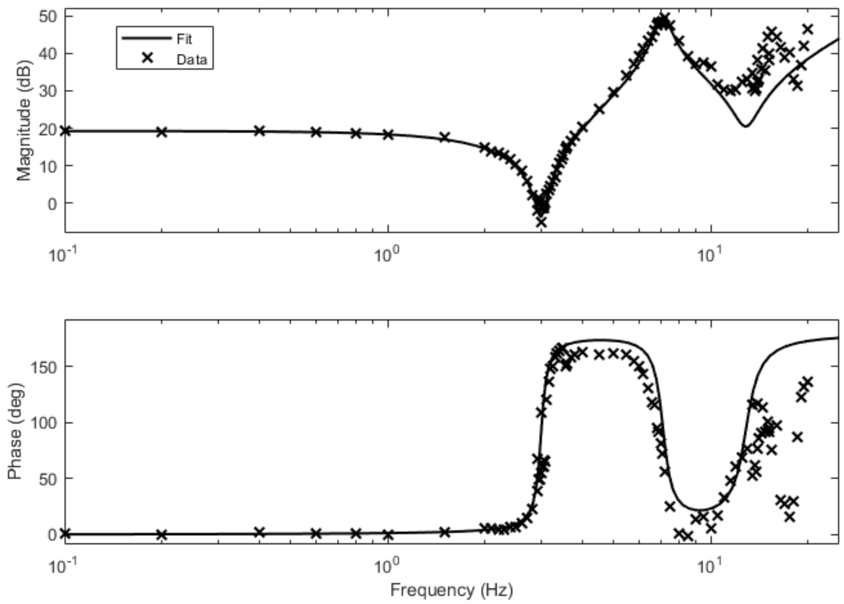

Figure 3.4: Flexible beam experimental frequency response and its fit, $G_{x_r}(j\omega) = \frac{F(j\omega)}{X_r(j\omega)}$.

3.2.2 Flexible Structure Dynamics

We begin with the flexible structure modeled in Figure 3.5,

$$m_2\ddot{x}_r = k_2(x_1 - x_r) + c_2(\dot{x}_1 - \dot{x}_r) - F, \tag{3.11}$$

$$m_1\ddot{x}_1 = k_2(x_r - x_1) + c_2(\dot{x}_r - \dot{x}_1) + k_1(x_h - x_1) + c_1(\dot{x}_h - \dot{x}_1). \tag{3.12}$$

we take the Laplace transform of Equation (3.11):

$$m_2s^2X_r(s) = (k_2 + c_2s)[X_1(s) - X_r(s)] - F(s), \tag{3.13}$$

which can be rearranged as

$$F(s) = -(m_2s^2 + k_2 + c_2s)X_r(s) + (k_2 + c_2s)X_1(s). \tag{3.14}$$

Next, Equation (3.12) gives:

$$m_1s^2X_1(s) = (k_2 + c_2s)[X_r(s) - X_1(s)] + (k_1 + c_1s)[X_h(s) - X_1(s)]. \tag{3.15}$$

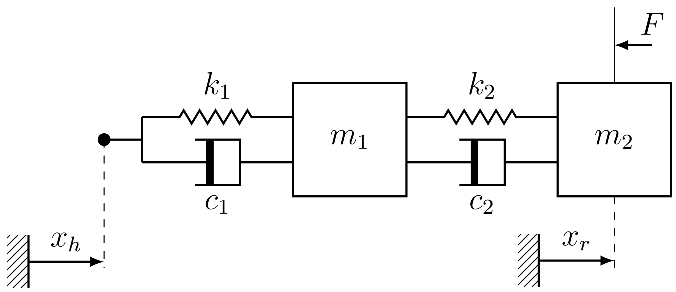

Figure 3.5: Diagram of flexible structure with two masses.

Expanding and collecting like terms:

$$m_1s^2X_1(s) + (k_2 + c_2s + k_1 + c_1s)X_1(s) = (k_2 + c_2s)X_r(s) + (k_1 + c_1s)X_h(s). \quad (3.16)$$

Define

$$D(s) = m_1s^2 + (c_1 + c_2)s + (k_1 + k_2). \quad (3.17)$$

Then we obtain:

$$X_1(s) = \frac{(k_2 + c_2s)X_r(s) + (k_1 + c_1s)X_h(s)}{D(s)}. \quad (3.18)$$

Substitute Equation (3.18) into Equation (3.14):

$$F(s) = -(m_2s^2 + k_2 + c_2s)X_r(s) + (k_2 + c_2s)\frac{(k_2 + c_2s)X_r(s) + (k_1 + c_1s)X_h(s)}{D(s)}. \quad (3.19)$$

Grouping terms,

$$F(s) = \left\{-(m_2s^2 + k_2 + c_2s) + \frac{(k_2 + c_2s)^2}{D(s)}\right\}X_r(s) + \frac{(k_2 + c_2s)(k_1 + c_1s)}{D(s)}X_h(s). \quad (3.20)$$

We express the output $F(s)$ as:

$$F(s) = -G_{x_r}(s)X_r(s) + G_{x_h}(s)X_h(s), \quad (3.21)$$

where the transfer functions are:

$$G_{x_r}(s) = m_2s^2 + k_2 + c_2s - \frac{(k_2 + c_2s)^2}{D(s)}, \quad (3.22)$$

$$G_{x_h}(s) = \frac{(k_2 + c_2s)(k_1 + c_1s)}{D(s)}. \quad (3.23)$$

The parameters are fit from the frequency response and are $m_1 = 0.0255$ kg, $k_1 = 12$ N/m, $c_1 = 0.04$ N $\cdot$ s/m, $m_2 = 0.008$ kg, $k_2 = 39$ N/m, and $c_2 = 0.07$ N $\cdot$ s/m.

3.2.3 Simulated Deformations with Standard Method

The deformation transfer function based on the model is,

$$T(s) = \frac{\delta(s)}{X_h(s)} = 1 - \frac{X_r(s)}{X_h(s)} = 1 - \frac{G_{x_h}(s)G_r(s)C(s)}{s + G_{x_r}(s)G_r(s)C(s)}. \tag{3.24}$$

where G_r and G_{x_r} are from the fits in the previous section. The human component of the transfer function is not directly observable, and is found using the parameters from the fit of G_{x_r}. The controller $C(s)$ is the standard admittance controller $Y(s)$, parametrized by cutoff ω_c and gain. We simulate the deformation for a sinusoidal human reference trajectory, $x_h = \sin(2\pi f t)$, with $f = 0.4$ Hz, which is within human bandwidth.

The next step is to modify $C(s)$ so that deformation is reduced while maintaining stability.

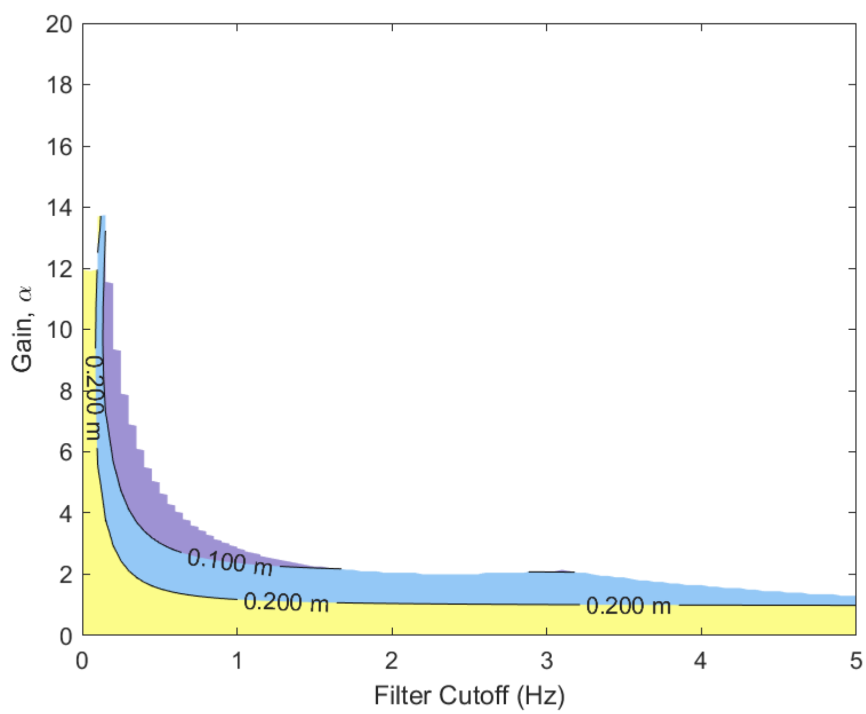

Figure 3.6: Simulated RMS deformation with standard control method, $C(s) = Y(s)$ for varying parameters. White areas are unstable.

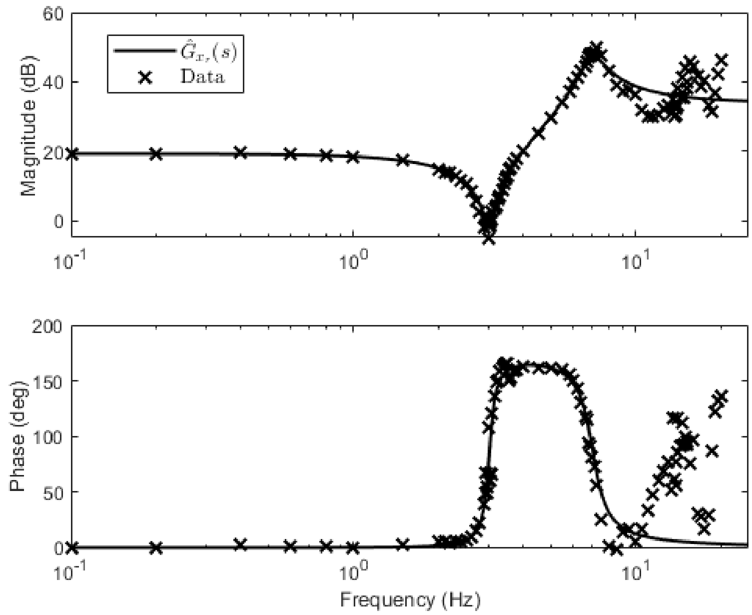

Figure 3.7: Raw data and the model, $\hat{G}_{x_r}$

3.3 Proposed Approach

To reduce deformation, the controller compensates for the flexible-object dynamics. An approximate inverse model $\hat{G}_{x_r}^{-1}(s)$ of the flexible dynamics is used with the standard admittance controller, modifying the control law in Eq. (3.8) as

$$C(s) = Y(s)\hat{G}_{x_r}^{-1}(s). \tag{3.25}$$

Since the high-frequency dynamics approach the bandwidth of the robot dynamics, they are difficult to capture accurately. The inverse model therefore captures the dominant resonance/anti-resonance behavior,

$$\hat{G}_{x_r}(s) = K_{eq}\left(\frac{\omega_p}{\omega_z}\right)^2 \frac{s^2 + 2\zeta_z\omega_z s + \omega_z^2}{s^2 + 2\zeta_p\omega_p s + \omega_p^2} \tag{3.26}$$

where the fitted frequencies are $f_z = 3.0$ Hz and $f_p = 7.1$ Hz, with $\omega_z = 2\pi f_z$ and

$\omega_p = 2\pi f_p$. The fitted damping ratios are $\zeta_z = 0.02$ and $\zeta_p = 0.065$.

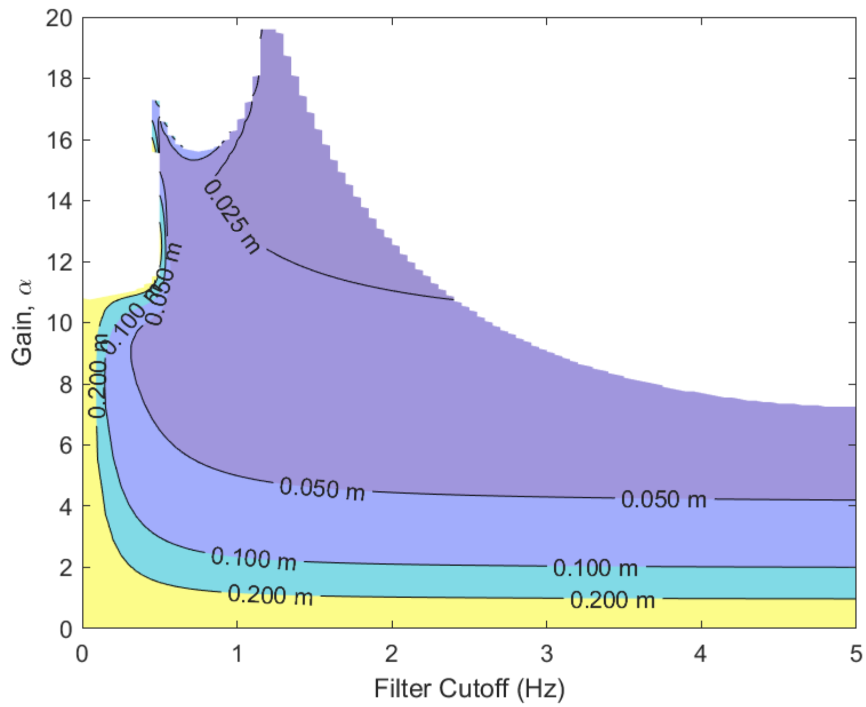

Figure 3.8: Simulated RMS deformation with proposed (inverse-model) control method, $C(s) = Y(s)\hat{G}_{x_r}^{-1}(s)$ for varying parameters. White areas are unstable.

In the inverse model, we omit the spring constant so the DC gain is one and therefore α does not need to be scaled between the standard and proposed approaches. The inverse model is therefore,

$$\hat{G}_{x_r}^{-1}(s) = \left(\frac{\omega_z}{\omega_p}\right)^2 \frac{s^2 + 2\zeta_p\omega_p s + \omega_p^2}{s^2 + 2\zeta_z\omega_z s + \omega_z^2} \tag{3.27}$$

Simulated Results with Proposed Method

With inverse-model compensation, the simulated deformation is reduced. Fig. 3.8 shows a 54% reduction in RMS deformation relative to standard admittance control.

3.4 Experiment

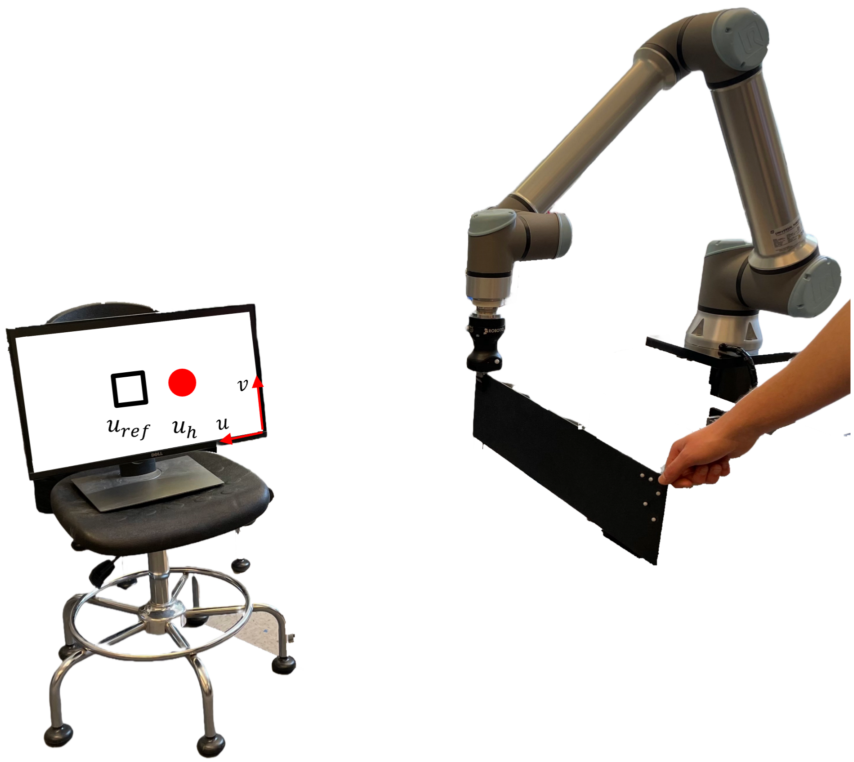

Figure 3.9: Experimental setup showing the on-screen reference trajectory (black rectangle) and the robot cursor (red), both displayed in pixel coordinates.

A sinusoidal reference trajectory

$$x_{\mathrm{ref}}(t) = 0.12\sin(0.4 \times 2\pi\, t) + x_0$$

was defined in robot coordinates. The amplitude (0.12 m) was chosen to use 80% of the robot's reachable workspace without colliding with its stand or reaching singularity. The frequency (0.4 Hz) lies within the human's voluntary tracking bandwidth while still challenging the human-robot interaction.

The corresponding peak reference speed is

$$\max_t |\dot{x}_{\mathrm{ref}}(t)| = 0.12(2\pi)(0.4) = 0.302 \text{ m/s}, \tag{3.28}$$

or approximately 30 cm/s. Note that this is the reference trajectory maximum speed, and participant and robot measured peak speeds can differ because of human tracking error.

The reference trajectory was converted to screen coordinates via

$$u(t) = \frac{0.8 \times 1920}{2 \times 0.12}\,(x_{\text{ref}}(t) - x_0) + \frac{1920}{2}, \quad v(t) = 0,$$

and displayed on a 60 Hz, 1920x1080 pixel monitor. The human participant attempted to follow the moving cursor by manipulating the robot end-effector; the robot's actual position $x_r(t)$ was likewise transformed to screen coordinates and overlaid on the same display, analogous to a pursuit-tracking paradigm [51]. The robot motion was in front of the user, approximately in their transverse plane. Each trial lasted 70 s, with the initial 30 s regarded as familiarization and excluded from analysis. Gain settings for the admittance/inverse-model controllers were presented in randomized order. A single subject completed the trial.

3.5 Results

Beam deformation was quantified as

$$\delta_{\text{rms}} = 100\% \times \frac{1}{A}\sqrt{\frac{1}{N}\sum_{i=1}^{N}\delta_i^2},$$

where $A = 0.12$ m is the sine amplitude and $\delta_i = x_h(t_i) - x_r(t_i)$. Fig. 3.10(a) shows that the inverse-model controller reduced deformation by approximately 45% compared to the baseline admittance controller.

High-frequency vibration energy was computed as

$$P = \sum_{\omega=2\text{ Hz}}^{f_s/2} |F(\omega)|^2,$$

where $F(\omega)$ is the Fourier transform of the force signal and $f_s = 500$ Hz is the sampling rate. Figure 3.10(b) indicates an increase in P as controller gain increased.

Fig. 3.11 presents representative time traces at the maximal stable gain. The inverse model also reduced average forces, with total work, $\int F dx$, reduced from 0.66 J to 0.20 J.

3.6 MC1: Conclusion

MC1 showed that an approximate inverse of the flexible-beam dynamics integrated into an admittance controller substantially reduced both deformation and high-frequency vibration in the human-robot task. Theoretical predictions of deformation reduction aligned with experimental observations, demonstrating up to a 45% decrease in δ_{rms} while maintaining stability. Time-domain traces confirmed attenuation of peak deformation and force. These results validate the efficacy of inverse-model compensation for collaborative transport of flexible objects using only end-effector force sensing.

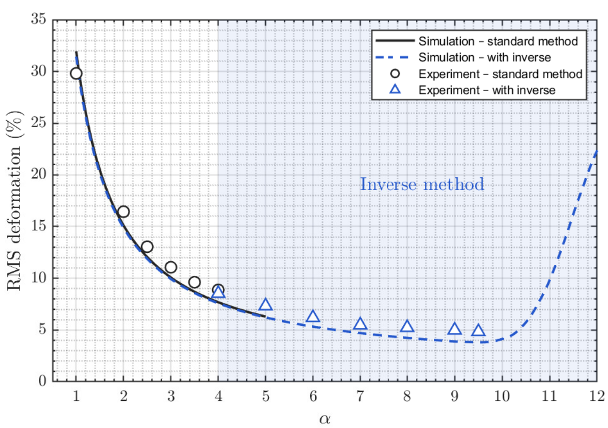

(a) RMS deformation percentage

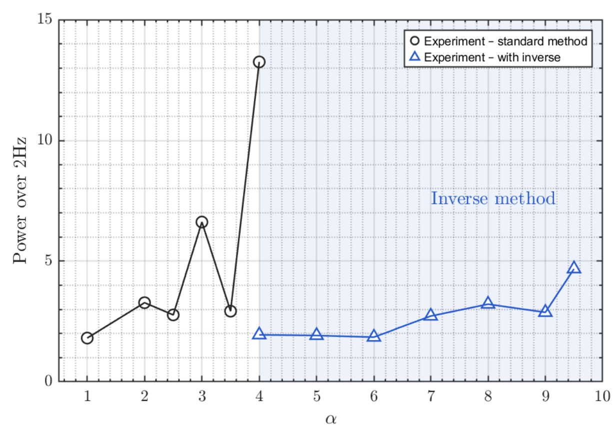

(b) Spectral power above 2 Hz

Figure 3.10: Summary of steady-state performance metrics. (a) Normalized root-mean-square beam deformation, δ_{rms}. (b) High-frequency vibration energy, P, integrated from 2 Hz to the Nyquist frequency.

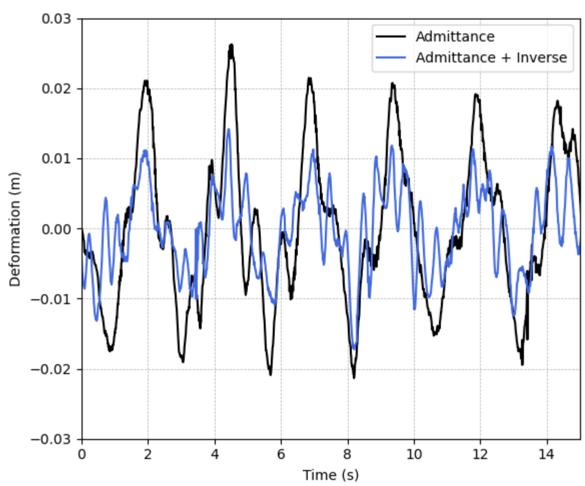

(a) Beam deformation over time

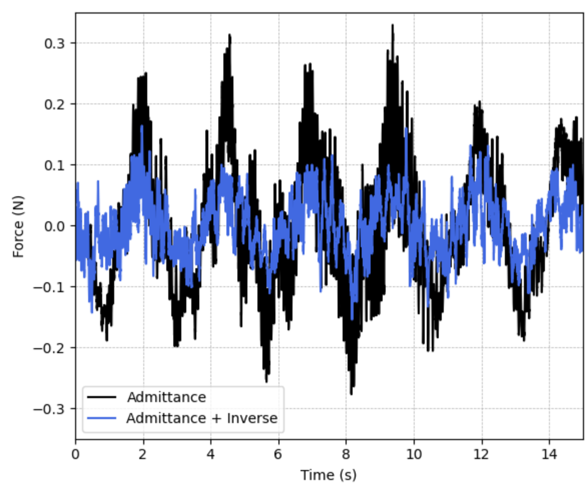

(b) End-effector force over time

Figure 3.11: Time series at the highest stable gain setting. Inverse-model compensation (blue) yields lower peak deformation and reduced force compared to baseline admittance control (black).

Chapter 4

MC2: ITERATIVE LEARNING FOR FLEXIBLE OBJECT CO-TRANSPORT

Chapter 4 develops the second main contribution of the thesis, an iterative learning method for flexible-object co-transport based on the author's work in [52]. MC2 extends the within-trial dynamics compensation of Chapter 3 to repeated-task improvement across trials: instead of relying only on higher effective admittance, the robot uses measured force and its own motion to infer human position and iteratively reduce deformation over repeated executions.

This contribution is particularly relevant when flexible-object dynamics remain significant within the bandwidth of human motion, so that online compensation alone is insufficient to achieve small deformation. The chapter therefore develops a dynamics-based human-motion estimator together with an iterative feedforward update, and shows how repeated interaction can improve co-transport performance beyond a single demonstration.

4.1 Introduction

Chapter 3 addressed the case where compensating the flexible-object dynamics inside the admittance controller can improve within-trial performance. MC2 considers a different regime: repeated co-transport tasks in which the flexible-object dynamics remain significant within the bandwidth of human motion, so within-trial admittance control alone is insufficient to achieve small deformation. In this setting, the robot measures only end-effector force/torque and its own motion during execution, while human motion is available only for offline evaluation.

Ignoring additional filters, standard admittance control gives the closed-loop map

$$\frac{x_r(s)}{x_h(s)} = \frac{Y(s)G_r(s)G_{x_h}(s)}{s + Y(s)G_r(s)G_{x_r}(s)}. \tag{4.1}$$

If inverse-model compensation is added as in MC1, the corresponding map becomes

$$\frac{x_r(s)}{x_h(s)} = \frac{Y(s)G_r(s)\hat{G}_{x_r}^{-1}(s)G_{x_h}(s)}{s + Y(s)G_r(s)\hat{G}_{x_r}^{-1}(s)G_{x_r}(s)}. \tag{4.2}$$

Under perfect model match, $\hat{G}_{x_r}(s) = G_{x_r}(s)$, this reduces to

$$\frac{x_r(s)}{x_h(s)} = \frac{Y(s)G_r(s)G_{x_r}^{-1}(s)G_{x_h}(s)}{s + Y(s)G_r(s)}. \tag{4.3}$$

Thus, inverse compensation can recover a denominator similar to that of the rigid-object case, which explains why compensation can increase the allowable gain and improve stability margins. However, even with perfect compensation, the numerator still contains the factor $G_{x_r}^{-1}(s)G_{x_h}(s)$. When the flexible-object dynamics are sufficiently high in frequency, this factor is approximately constant over the bandwidth of voluntary human motion, so the compensation used in MC1 can achieve low deformation. When the dominant flexible dynamics move into the human-motion bandwidth, however, this numerator term is no longer approximately constant, and increasing the effective admittance alone does not guarantee small deformation. This situation can arise for heavier or more compliant structures, since increasing mass or reducing stiffness lowers the natural frequencies and moves the object dynamics closer to the bandwidth of human motion. Appendix C formalizes this point with the baseline model by showing that the high-gain tracking limit depends on $G_{x_h}(s)/G_{x_r}(s)$, which degrades as the object natural frequency enters the human-motion band. This is the regime considered in MC2, and it motivates improving performance across repeated trials rather than relying only on within-trial compensation.

The goal of this chapter is to use repetition across trials to improve coordination between the human and robot without direct sensing of human motion in the control loop. To do so, the chapter develops a dynamics-based estimator of human motion from measured force and robot motion, and then uses this estimate in an iterative learning scheme that updates a feedforward correction between trials. The central question is whether repeated interaction can reduce deformation beyond what is achievable with admittance control alone.

The main contributions of this chapter are the following.

- **Inversion-based human-motion trajectory inference:** The human motion is estimated from measured force and robot motion using the flexible-object dynamics rather than relying on additional sensing.

- **Iterative update for improved tracking:** The standard admittance controller is augmented with an iterative feedforward input to enable accurate co-transport with reduced deformation over repeated executions.

- **Experimental validation:** The method is validated on a UR10e co-transport task and shows reduced object deformation together with improved co-transport precision compared with the standard admittance approach.

4.2 Problem Formulation

4.2.1 System Description

Consider the case where a human operator holds a flexible object and moves it by x_h while a robotic partner grasps another location (on the undeformed flexible object) and moves it by x_r, as illustrated in Fig. 4.1. The task objective is to reduce the flexible object deformation, which corresponds to the relative displacement

$$\delta(t) = x_h(t) - x_r(t). \tag{4.4}$$

For notational convenience, define $x_h = x'_h - x_0$ such that $x_h = x_r = 0$ when the object is undeformed; the offset in the undeformed state is x_0. In the admittance controller setting, the robot has access to (i) end-effector force/torque (F/T) sensing and (ii) robot state, including end-effector position/velocity, which are readily available for industrial robotic manipulators. Direct sensing of the human position $x_h(t)$ (via motion capture) is not available during

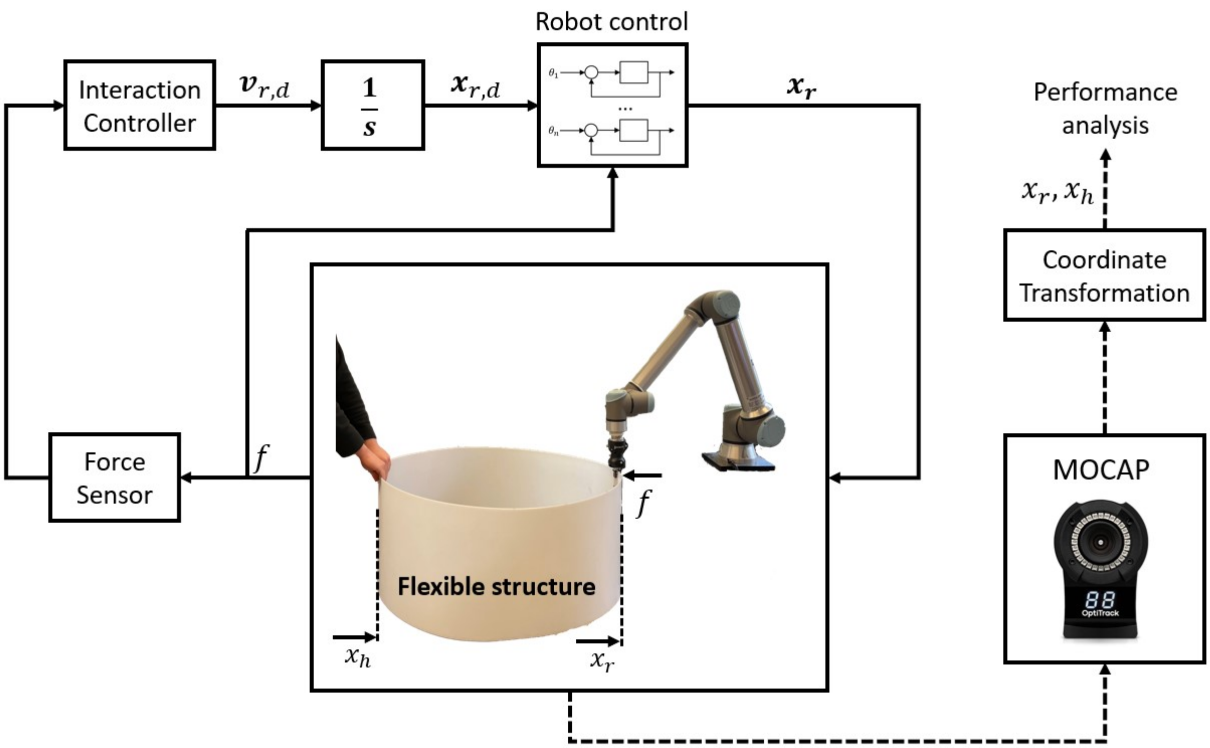

Figure 4.1: Overview of co-transport with admittance control. The UR10e robot grasps one end of the flexible object and measures interaction force/torque f using a force/torque (F/T) sensor while a human grasps the opposite end. The reference trajectory x_{ref} is displayed using the preview-tracking interface shown in Fig. 4.5, and the user attempts to track the provided reference. The interaction (admittance) controller generates desired robot motion $x_{r,d}$ from the measured force f. A motion capture system (MOCAP) measures positions on the flexible structure for performance analysis, but is not used for control.

deployment, but is available for offline evaluation of performance. Therefore, the reduction in the deformation δ needs to be achieved using the sensed force.

4.2.2 Standard Admittance Controller

With a standard admittance controller Y, the commanded robot end-effector velocity $v_{r,d}$ is selected to be proportional to a filtered version of the sensed force f by the robot, i.e.,

$$v_{r,d}(s) = Y(s)f(s) \tag{4.5}$$

where the admittance controller is

$$Y(s) = \alpha\frac{\omega_c}{s+\omega_c} = \frac{1}{m_a s + b_a}, \tag{4.6}$$

with gain α, and cutoff frequency ω_c (rad/s).

Remark 1 (Rigid Object Case)**.** *For a rigid object the admittance controller leads to a specified effective mass $m_a = 1/(\alpha\omega_c)$ and effective damping $b_a = 1/\alpha$ as in Eq.* (4.6) *between the human force f and the robot velocity $v_{r,d}$.*

4.2.3 Flexible Object Case

For a general flexible object, the force applied f by the robot end effector and the force f_h applied by the human are related to the displacements x_r and x_h at the robot and human grasp positions from a nominal undeformed position (along the axis of motion) as

$$\begin{bmatrix} x_h(s) \\ x_r(s) \end{bmatrix} = \begin{bmatrix} G_{hh}(s) & G_{hr}(s) \\ G_{rh}(s) & G_{rr}(s) \end{bmatrix} \begin{bmatrix} f_h(s) \\ -f(s) \end{bmatrix}, \tag{4.7}$$

where G_{hh}, G_{rr} are minimum phase since they correspond to displacement and force being collocated and G_{hr}, G_{rh} are nonminimum phase since they correspond to displacement and force being non-collocated – all these transfer functions have the same poles. Eliminating the human force $f_h(s)$ from the two equations in Eq. (4.7) results in

$$\begin{aligned} f(s) &= \frac{G_{rh}(s)x_h(s) - G_{hh}(s)x_r(s)}{G_{hh}(s)G_{rr}(s) - G_{rh}(s)G_{hr}(s)} \\ &= G_{x_h}(s)\, x_h(s) - G_{x_r}(s)\, x_r(s), \end{aligned} \tag{4.8}$$

where G_{x_h} and G_{x_r} capture the mapping from motions of the human grasp position x_h and robot grasp position x_r, respectively, to the measured force f as shown in Fig. 4.2.

Remark 2 (Nonminimum-phase Dynamics)**.** *The mapping G_{x_h} from motion x_h of the human grasp position to the measured force f is nonminimum phase since*

$$G_{x_h}(s) = \frac{G_{rh}(s)}{G_{hh}(s)G_{rr}(s) - G_{rh}(s)G_{hr}(s)} \tag{4.9}$$

from Eq. (4.8) *and the non-collocated transfer function G_{rh} is nonminimum phase.*

In general, the nonminimum-phase zeros may not lie inside the bandwidth of the task. For non-collocated flexible-structure dynamics, right-half-plane zeros can lie well outside the desired closed-loop bandwidth, so identified models can appear minimum phase [53].

Remark 3 (Low-Frequency Approximation)**.** *At low frequency, both transfer functions G_{x_h} and G_{x_r} in Eq.* (4.8) *converge to an equivalent stiffness k_{eq}, so that Eq.* (4.8) *becomes*

$$f(s) \approx k_{eq}\,[x_h(s) - x_r(s)], \tag{4.10}$$

which is a simplified single spring approximation of the flexible structure.

Applying the admittance controller in Eq. (4.5) to the flexible object in Fig. 4.2 results in the following closed-loop transfer function from the human motion x_h to the robot motion x_r

$$\frac{x_r(s)}{x_h(s)} = G_{x_{r,h}}(s) = \frac{Y(s)G_r(s)G_{x_h}(s)}{s + Y(s)G_r(s)G_{x_r}(s)}, \tag{4.11}$$

where $G_r = x_r(s)/x_{r,d}(s)$ represents the robot's dynamics from the commanded robot grasp position $x_{r,d}(s)$ to the actual robot grasp position $x_r(s)$.

4.2.4 Challenge and Research Problem

The objective in co-transport is to make the robot track the human motion so that $x_r \approx x_h$ and therefore, the object deformation δ in Eq. (4.4) is small. This can be achieved if the admittance controller Y in Eq. (4.11) has a sufficiently-high gain α. However, the challenge is that the maximum gain of the admittance controller Y is limited by the flexible-object dynamics in the closed loop; increasing α can excite the flexible dynamics and reduce the

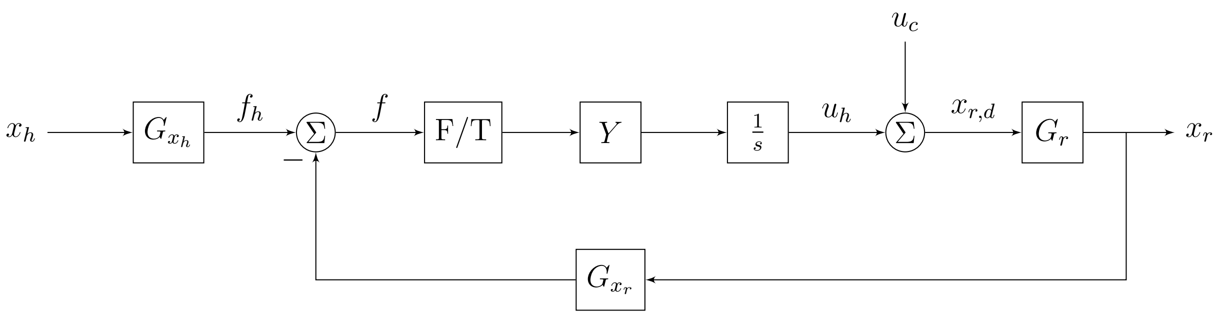

Figure 4.2: Block diagram of object co-transport with feedforward control u_c. The human motion and robot motion are mapped to force f through G_{x_h} and G_{x_r}, respectively. u_h is the integral of the admittance-controller Y output. The desired robot position $x_{r,d}$ is realized through the robot's internal controller G_r. F/T represents the force/torque sensor.

stability margin, as shown in [50]. Moreover, the human-motion path G_{x_h} in Eq. (4.8) is nonminimum phase (see Remark 2), so a direct causal stable inverse of this non-collocated path cannot be used to remove the deformation in one trial. The limited gain implies that the object deformation δ during the co-transport can be large, e.g., error of 0.079 m, as shown in Fig. 4.3.

The research problem is to reduce the object deformation δ when using the force-based admittance controller. This problem has the following two research issues.

The first research issue is that the object dynamics affects the relationship between measured force f and the object deformation. Specifically, from the static (low-frequency) relation in Eq. (4.10), the human motion x_h can be estimated as

$$\hat{x}_{h,spring}(t) = \frac{1}{k_{eq}} f(t) + x_r(t). \tag{4.12}$$

Note that the error e_{spring} in this estimate

$$e_{spring}(t) = x_h(t) - \hat{x}_{h,spring}(t) \tag{4.13}$$

can be substantial as shown in Fig. 4.3 with a root-mean-square (RMS) value 1.89cm and max value 4.57cm. The first research problem is to correct such object-dynamics-caused

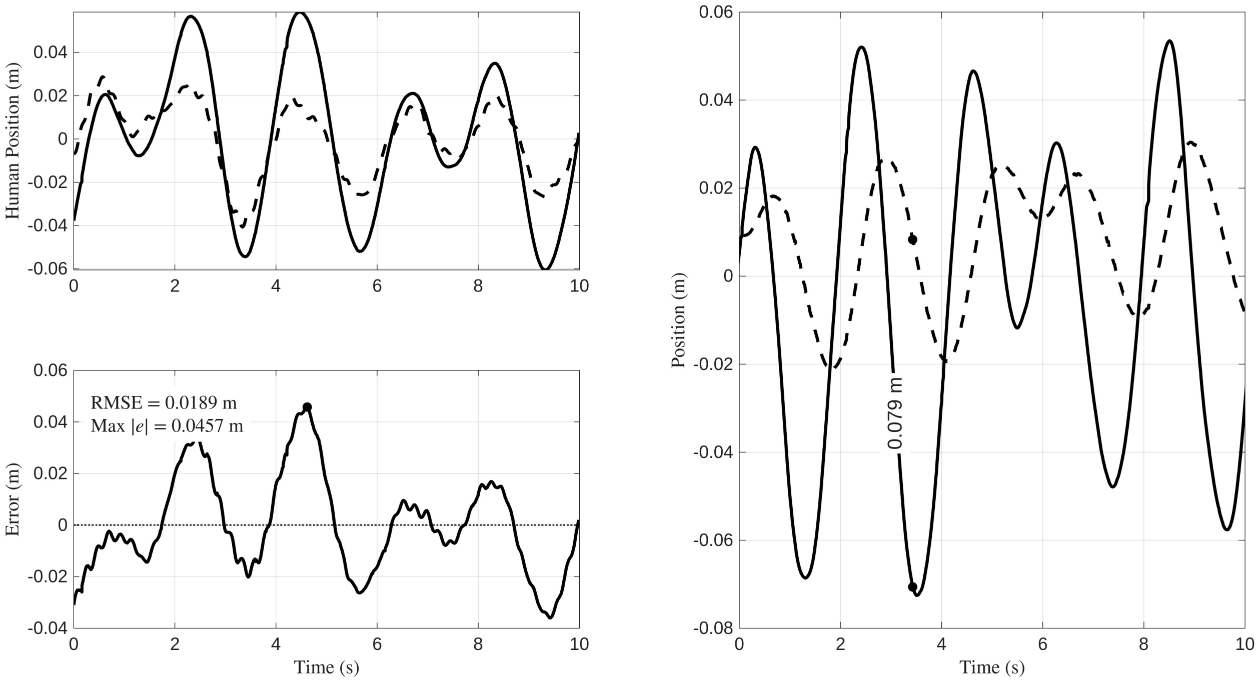

Figure 4.3: Experimental co-transport results with standard admittance control. (Left) Large differences between the robot position x_r and human position x_h leading to large flexible-object deformation, $\delta = x_h - x_r$. (Right) Error in estimating human position x_h from experimental data. Top: Spring-based estimated human position $\hat{x}_{h,spring}$ (dashed line) using Eq. (4.12) compared to measured human position x_h using MOCAP (solid line) Bottom: Error $e_{spring} = x_h - \hat{x}_{h,spring}$ in the spring-based estimate $\hat{x}_{h,spring}$ of human position.

error when estimating the human position x_h. The second research issue is to correct error in tracking the human action x_h by the robot grasp position x_r, i.e., to ensure $x_r = x_h$ for reducing the object deformation δ. These are addressed in the following section.

4.3 Proposed Approach

The proposed method addresses the two components identified as research problems. First, the human motion is estimated from the measured interaction force and robot motion using identified flexible-object dynamics, so direct sensing of the human position is not required during execution. Second, this estimated motion is used to iteratively update a corrective feedforward input between trials. The admittance controller preserves stability, while the learned feedforward term improves tracking of the repeated human motion across trials.

4.3.1 Human-Position Estimation

The human position x_h is estimated from the measured force and robot motion using identified models $\hat{G}_{x_h}$ and $\hat{G}_{x_r}$ of the object dynamics G_{x_h} and G_{x_r} in Eq. (4.8), as

$$\hat{x}_h(s) = \hat{G}_{x_h}^{-1}(s)[f(s) + \hat{G}_{x_r}(s)x_r(s)]. \tag{4.14}$$

The estimated human position $\hat{x}_h$ is computed in the Fourier domain $\mathcal{F}$ at the end of a co-transport task as

$$\hat{x}_h(t) = \mathcal{F}^{-1}\{\hat{G}_{x_h}^{-1}(j\omega)[f(j\omega) + \hat{G}_{x_r}(j\omega)x_r(j\omega)]\} \tag{4.15}$$

The inverse is applied offline in the Fourier domain, rather than as a causal real-time inverse, because $\hat{G}_{x_h}$ is nonminimum phase in general, as discussed earlier. In the following, it is assumed that the estimated flexible-object dynamics, $\hat{G}_{x_h}$ and $\hat{G}_{x_r}$ in Eq. (4.14), are available, either through finite element techniques or experimental offline identification.

4.3.2 Iterative Correction of Robot Tracking

The proposed approach seeks to reduce the tracking error e between the human and robot positions by adding a feedforward compensation u_c to the desired-output position $u_h(s) = Y(s)f(s)/s$ generated by the admittance controller to obtain the desired robot position $x_{r,d} = u_c + u_h$, as illustrated in Fig. 4.2. The resulting robot position x_r satisfies

$$x_r(s) = G_r(s)(u_c(s) + u_h(s)) \tag{4.16}$$

$$= \underbrace{\frac{sG_r(s)}{s + YG_rG_{xr}}}_{G_{ff}(s)} u_c(s) + \underbrace{\frac{YG_rG_{xh}}{s + YG_rG_{xr}}}_{G_{fb}(s)} x_h(s) \tag{4.17}$$

$$= G_{ff}(s)u_c(s) + G_{fb}(s)x_h(s). \tag{4.18}$$

Then, the tracking error e, between the human and robot positions, is given by

$$e(s) = x_h(s) - x_r(s) = [1 - G_{fb}(s)]x_h(s) - G_{ff}(s)\, u_c(s). \tag{4.19}$$

The above tracking error e is reduced in an iterative manner. During each trial k, (where $k = 0, 1, 2, \ldots$), the robot runs an online admittance controller together with a feedforward position input $u_{c,k}$. The resulting robot motion $x_{r,k}$ is

$$x_{r,k}(s) = G_{fb}(s)\, x_{h,k}(s) + G_{ff}(s)\, u_{c,k}(s), \tag{4.20}$$

and the tracking error $e_k = x_{h,k} - x_{r,k}$ between the human and robot during trial k is, from Eq. (4.19) and Eq. (4.20),

$$e_k(s) = [1 - G_{fb}(s)]x_{h,k}(s) - G_{ff}(s)\, u_{c,k}(s). \tag{4.21}$$

Writing a similar expression for e_{k+1} and subtracting the two gives

$$e_{k+1}(s) = e_k(s) - G_{ff}(s)[u_{c,k+1}(s) - u_{c,k}(s)], \tag{4.22}$$

when the demonstrated human trajectory is assumed to be consistent between trials, i.e., $x_h = x_{h,k+1} = x_{h,k}$. If the human trajectory is not exactly repeated and $\eta_k(s) = x_{h,k+1}(s) - x_{h,k}(s)$, then the corresponding recursion is

$$e_{k+1}(s) = e_k(s) - G_{ff}(s)[u_{c,k+1}(s) - u_{c,k}(s)] + [1 - G_{fb}(s)]\, \eta_k(s). \tag{4.23}$$

Ideally, the tracking error at iteration trial $k + 1$ can be made zero by selecting the feedforward input $u_{c,k+1}$ as, from Eq. (4.22),

$$u_{c,k+1}(s) = u_{c,k}(s) + G_{ff}^{-1}(s)e_k(s). \tag{4.24}$$

This ideal update, however, requires knowledge of the error e_k, which depends on the human motion x_h and knowledge of the transfer function G_{ff}, neither of which are known exactly. Therefore, in the following, estimated error $\hat{e}_k$ and estimated feedforward transfer function $\hat{G}_{ff}$ are used to iteratively correct the tracking error, as

$$u_{c,k+1}(s) = u_{c,k}(s) + \rho(s)\, \hat{G}_{ff}^{-1}(s)\, \hat{e}_k(s), \tag{4.25}$$

where $\rho(s)$ is a frequency dependent iteration gain and $\hat{G}_{ff}$ is the estimated feedforward model. The estimated error $\hat{e}_k$

$$\hat{e}_k(s) = \hat{x}_{h,k}(s) - x_{r,k}(s). \tag{4.26}$$

is found from the estimated human position $\hat{x}_{h,k}$. The estimated human position from Eq. (4.14) is

$$\hat{x}_{h,k}(s) = \hat{G}_{x_h}^{-1}(s)[f_k(s) + \hat{G}_{x_r}(s)x_{r,k}(s)], \tag{4.27}$$

using identified models $\hat{G}_{x_h}$ and $\hat{G}_{x_r}$.

4.3.3 Convergence Analysis of Iterative Robot Tracking

The following lemma gives the convergence result when the human motion is repeated and the human-motion estimate is exact. This ideal case gives the contraction condition used to select the iteration gain. The effects of estimator error and imperfect human repeatability are considered in Remark 4.

Lemma 1. *For a fixed co-transport task with repeated human input*

$$x_{h,k}(s) = x_h(s), \tag{4.28}$$

and a perfect error estimate

$$\hat{e}_k(s) = e_k(s), \tag{4.29}$$

the tracking error at each frequency converges to zero, i.e.,

$$\lim_{k\to\infty} e_k(j\omega) = 0 \tag{4.30}$$

if at each frequency,

$$|1 - \rho(\omega)\Delta_{ff}(j\omega)| < 1, \tag{4.31}$$

where

$$\Delta_{ff}(j\omega) = \frac{G_{ff}(j\omega)}{\hat{G}_{ff}(j\omega)} = \Delta_{ff,m}(\omega)e^{j\Delta_{ff,\theta}(\omega)}. \tag{4.32}$$

For real positive $\rho(\omega)$, this is satisfied by

$$0 < \rho(\omega) < \frac{2\cos(\Delta_{ff,\theta}(\omega))}{\Delta_{ff,m}(\omega)} = \bar{\rho}(\omega), \tag{4.33}$$

provided the phase error satisfies $\Delta_{ff,\theta}(\omega) \in (-\pi/2, \pi/2)$.

Proof: For a fixed repeated task, Eq. (4.22) gives

$$e_{k+1}(s) = e_k(s) - G_{ff}(s)[u_{c,k+1}(s) - u_{c,k}(s)]. \tag{4.34}$$

With a perfect error estimate, the update law in Eq. (4.25) becomes

$$u_{c,k+1}(s) - u_{c,k}(s) = \rho(s)\hat{G}_{ff}^{-1}(s)e_k(s). \tag{4.35}$$

Substituting this into Eq. (4.34) gives

$$\begin{aligned} e_{k+1}(s) &= \left(1 - \rho(s)\frac{G_{ff}(s)}{\hat{G}_{ff}(s)}\right) e_k(s) \\ &= \left(1 - \rho(s)\Delta_{ff}(s)\right) e_k(s). \end{aligned} \tag{4.36}$$

At each frequency, repeated substitution gives

$$e_k(j\omega) = \left(1 - \rho(\omega)\Delta_{ff}(j\omega)\right)^k e_0(j\omega), \tag{4.37}$$

so $e_k(j\omega) \to 0$ if (4.31) holds. Writing $\Delta_{ff} = \Delta_{ff,m}e^{j\Delta_{ff,\theta}}$, the condition $|1 - \rho\Delta_{ff}| < 1$ is equivalent to

$$1 + \rho^2\Delta_{ff,m}^2 - 2\rho\Delta_{ff,m}\cos(\Delta_{ff,\theta}) < 1. \tag{4.38}$$

For real positive ρ, this gives

$$0 < \rho(\omega) < \frac{2\cos(\Delta_{ff,\theta}(\omega))}{\Delta_{ff,m}(\omega)} \tag{4.39}$$

when $\Delta_{ff,\theta}(\omega) \in (-\pi/2, \pi/2)$. $\square$

Lemma 1 shows that the iterative update removes the deformation in the ideal case where the human trajectory is exactly repeated and the error estimate is exact. In the physical experiment the estimated human motion has error, and the human does not reproduce exactly the same trajectory every trial. These effects can be treated as bounded disturbances.

Remark 4 (Noise and Variability)**.** *Let the human-motion estimation error be*

$$\varepsilon_k(s) = \hat{x}_{h,k}(s) - x_{h,k}(s), \tag{4.40}$$

so that

$$\hat{e}_k(s) = e_k(s) + \varepsilon_k(s). \tag{4.41}$$

This term includes errors caused by imperfect object models and measurement noise in the human-position estimator. For example, substituting the true force relation $f_k = G_{x_h} x_{h,k} - G_{x_r} x_{r,k}$ into Eq. (4.27) *gives*

$$\hat{x}_{h,k} = \hat{G}_{x_h}^{-1} \left[G_{x_h} x_{h,k} + \left(\hat{G}_{x_r} - G_{x_r} \right) x_{r,k} \right], \tag{4.42}$$

which shows that model mismatch can make ε_k depend on the robot motion $x_{r,k}$. Also let

$$\eta_k(s) = x_{h,k+1}(s) - x_{h,k}(s) \tag{4.43}$$

denote the run-to-run change in the human motion. Substituting the update law in Eq. (4.25) *into the non-repeated-task recursion in Eq.* (4.23) *gives*

$$e_{k+1}(j\omega) = [1 - \rho(\omega)\Delta_{ff}(j\omega)]\, e_k(j\omega) + d_k(j\omega). \tag{4.44}$$

The disturbance term is

$$d_k(j\omega) = -\rho(\omega)\Delta_{ff}(j\omega)\varepsilon_k(j\omega) + [1 - G_{fb}(j\omega)]\, \eta_k(j\omega), \tag{4.45}$$

where the first term is due to estimation error and the second term is due to imperfect human repeatability. If the estimator error and human repeatability error are bounded by $|\varepsilon_k(j\omega)| \leq N_\varepsilon(\omega)$ and $|\eta_k(j\omega)| \leq N_\eta(\omega)$, then the disturbance is bounded by

$$|d_k(j\omega)| \leq \rho(\omega)|\Delta_{ff}(j\omega)|N_\varepsilon(\omega) + |1 - G_{fb}(j\omega)|N_\eta(\omega). \tag{4.46}$$

then solving the linear recursion gives

$$\begin{aligned} e_k(j\omega) = {} & [1 - \rho(\omega)\Delta_{ff}(j\omega)]^k\, e_0(j\omega) \\ & + \sum_{i=0}^{k-1} [1 - \rho(\omega)\Delta_{ff}(j\omega)]^{k-1-i}\, d_i(j\omega). \end{aligned} \tag{4.47}$$

If this disturbance is bounded,

$$|d_k(j\omega)| \leq D(\omega), \tag{4.48}$$

and

$$W(\omega) = |1 - \rho(\omega)\Delta_{ff}(j\omega)| < 1, \tag{4.49}$$

then taking magnitudes and using the finite geometric series gives the bound

$$\begin{aligned} |e_k(j\omega)| \leq W(\omega)^k &|e_0(j\omega)| \\ &+ D(\omega)\frac{1 - W(\omega)^k}{1 - W(\omega)}. \end{aligned} \tag{4.50}$$

Therefore,

$$\limsup_{k\to\infty} |e_k(j\omega)| \leq \frac{D(\omega)}{1 - W(\omega)}. \tag{4.51}$$

The estimator error, measurement noise, and imperfect human repeatability cause the iterative method to be bounded rather than converge exactly to zero.

4.4 Experimental Methods

4.4.1 Platform and Hardware

Experiments are performed on a Universal Robots UR10e collaborative industrial manipulator. The robot grasps one endpoint of a flexible hoop (UHMW, 4 mm thick, 1000 mm diameter, 455 mm height) while a human grasps the opposite endpoint and performs repeated co-transport motions along a primary axis. Interaction forces are measured using a wrist-mounted force/torque sensor (ATI mini 45), which is projected onto the task axis for admittance control and learning. Motion capture is used only for offline evaluation of $x_h(t)$ and is not required by the proposed method.

Figure 4.4: Experimental setup for flexible-object co-transport. The UR10e grasps one end of the flexible object and measures interaction force/torque at the wrist while a human grasps the opposite end and repeats the task across iterations. A preview-tracking display is placed in front of the subject, and the subject attempts to track the moving reference with a five-second preview of the upcoming trajectory.

4.4.2 Preview-Tracking Display and Task

The repeated co-transport task was presented as a preview-tracking task, as shown in Fig. 4.5. The current reference position x_{ref} was shown as a red square, and the measured human position x_h was shown as a blue circle. The display also showed the upcoming 5 s of the reference trajectory as a red curve extending upward from the current reference point. Subjects could use information about the future trajectory to anticipate upcoming motion, rather than reacting only to the instantaneous target position. This type of display is consistent with manual preview-tracking tasks, where future target information changes human control behavior relative to pursuit displays [54]. A preview was added in MC2 (compared to pursuit in MC1) because the multi-sine trajectory is less predictable, and therefore harder for users to track, than the single sine trajectory used in MC1.

Each subject completed seven repeated iterations of the same reference trajectory,

$$x_{ref}(t) = 0.05\sin(2\pi \cdot 0.5t) + 0.05\sin(2\pi \cdot 0.34t), \tag{4.52}$$

over a 60 s trial. The peak reference speed is

$$\max_t |\dot{x}_{ref}(t)| = 0.264 \text{ m/s}, \tag{4.53}$$

or approximately 26.4 cm/s. After each trial, the subject returned to the initial configuration, and the feedforward input $u_{c,k}$ was updated using the logged force and robot-motion signals from trial k. Seven subjects ($N_u = 7$) completed the protocol. Exemption of research for this human-subjects study was granted by the UW Institutional Review Board (#STUDY00025413).

4.4.3 Selection of Admittance-Controller Parameters

The parameters (α, ω_c) of the admittance controller in Eq. (4.6) were selected to achieve the lowest deformation. An offline parameter sweep with a 0.5 Hz frequency grid size indicated that $\omega_c = 10\pi$ rad/s (5 Hz) provided the best result for the identified experimental system. With the cutoff fixed, a separate experiment increased α until persistent oscillations occurred. The empirical stability boundary was found to be $\bar{\alpha} = 0.8$. The experimental gain was set to $\alpha = 0.7$, which is approximately 90% of the maximum stable gain, to provide gain margin for robustness.

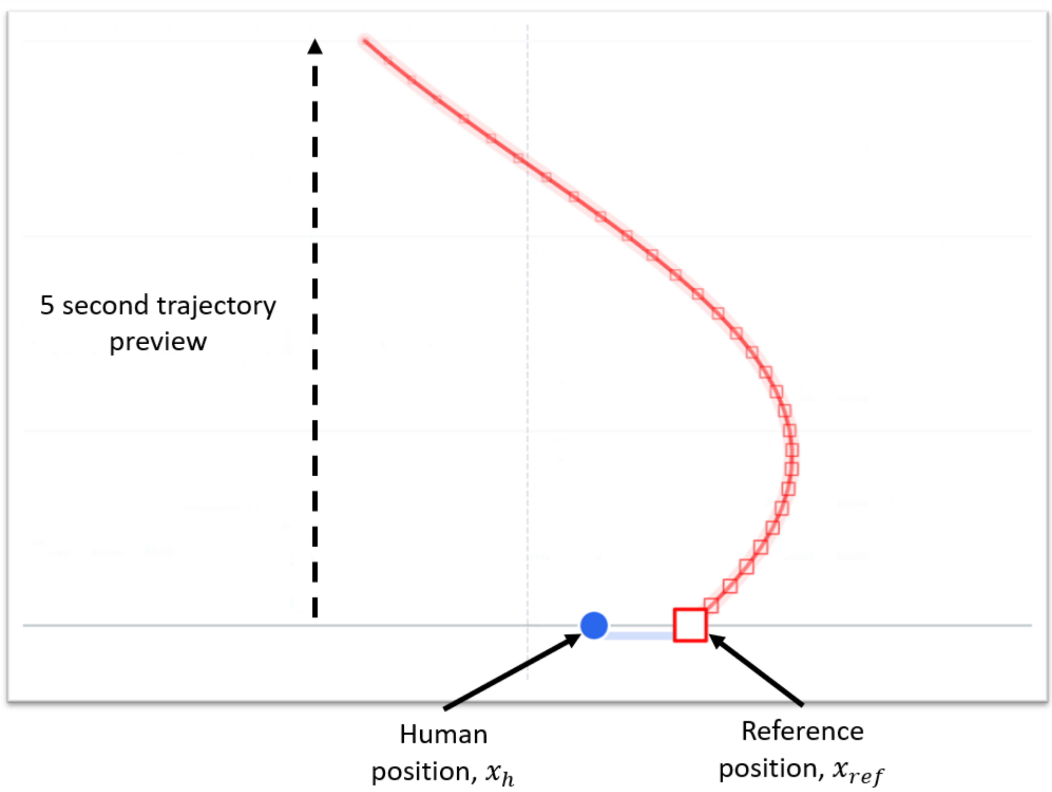

Figure 4.5: Preview-tracking display used in the iterative co-transport experiments. The blue marker shows the current human position x_h, the red square shows the current reference position x_{ref}, and the red curve shows the next 5 s of the reference trajectory.

4.4.4 Model Identification

The models needed for the iterative approach can be found using a model of the flexible object as in Eq. (4.7) or experimentally. In this subsection, the experimentally determined object models are presented.

Robot-position-to-force dynamics: The dynamics $G_{x_r}(s)$, which maps robot end-point motion to the measured force and is used in the closed-loop models (such as G_{ff} in Eq. (4.17)) and in the model-based human-motion estimator in Eq. (4.14), was estimated from measured force f when the robot position was changed using excitation frequencies

(0.1:0.05:30 Hz) with the human-side position held constant. The measured experimental response and that of the identified model are shown in Fig. 4.6.

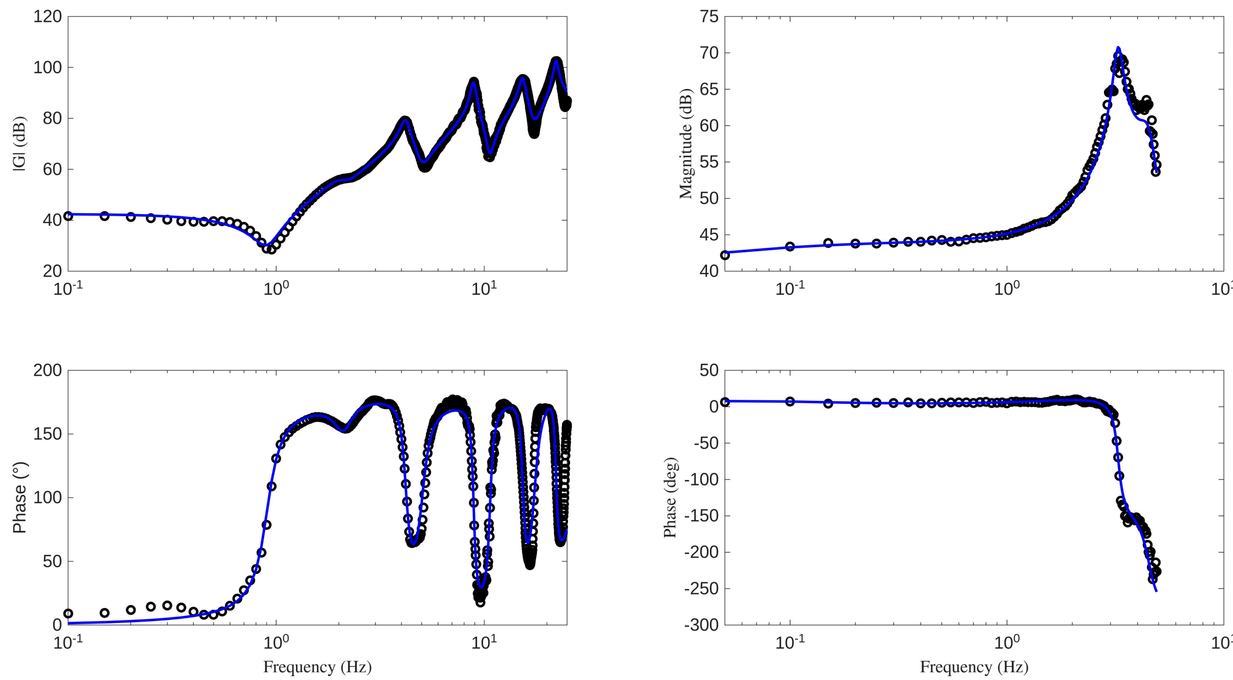

Figure 4.6: Experimental data (dots) and identified model (lines) of: (left column) flexible-object dynamics $\hat{G}_{x_r}(j\omega)$ mapping robot position to measured force; and (right column) flexible-object dynamics $\hat{G}_{x_h}(j\omega)$ mapping human position to measured force.

The robot-side FRF was identified from four multisine experiments collected using excitation frequencies (0.1:0.05:30 Hz). For each run, ten cycles of the fundamental frequency $f_0 = 0.05$ Hz were used. The measured force and robot position were then resampled onto a common uniform grid at 500 Hz using linear interpolation.

For each run m, a nonparametric FRF from robot endpoint position $x_r(t)$ to measured force $F(t)$ was computed using Welch's method with a Hann window of length 10 s and 50% overlap:

$$\hat{G}_{x_r,m}(j\omega) = \frac{S_{Fx_r,m}(j\omega)}{S_{x_rx_r,m}(j\omega)}. \tag{4.54}$$

The corresponding magnitude-squared coherence was computed as

$$\gamma_m^2(\omega) = \frac{|S_{Fx_r,m}(j\omega)|^2}{S_{x_rx_r,m}(j\omega)\, S_{FF,m}(j\omega)}. \tag{4.55}$$

To reduce run-to-run variance, the complex FRFs from all runs were combined using a coherence-weighted complex average at each frequency:

$$\hat{G}_{x_r,\mathrm{avg}}(j\omega_i) = \frac{\sum_{m=1}^{M} \gamma_m^2(\omega_i)\, \hat{G}_{x_r,m}(j\omega_i)}{\sum_{m=1}^{M} \gamma_m^2(\omega_i)}, \tag{4.56}$$

This preserves both magnitude and phase while weighting each run according to FRF reliability.

The stitched FRF was then fit with a stable transfer function model consisting of a cascade of second-order zero/pole pairs and a DC gain:

$$\hat{G}_{x_r}(s, \mathbf{p}) = K \prod_{i=1}^{N} \frac{s^2 + 2\zeta_{z,i}\omega_{z,i}s + \omega_{z,i}^2}{s^2 + 2\zeta_{p,i}\omega_{p,i}s + \omega_{p,i}^2}. \tag{4.57}$$

In the implementation, $N = 6$, yielding a 12th-order numerator and 12th-order denominator model plus an overall gain term. The model parameters were obtained by bounded nonlinear least-squares fitting to the complex FRF samples over the stitched FRD frequency grid, with the objective minimizing the weighted complex residual

$$\min_{\mathbf{p}} \left\| W(\omega)\left(\hat{G}_{x_r}(j\omega, \mathbf{p}) - \hat{G}_{x_r,\mathrm{avg}}(j\omega)\right) \right\|_2. \tag{4.58}$$

In addition to the coherence weighting used in the FRF stitching step, a low-pass fit-emphasis weight was applied during optimization to prioritize the low frequencies.

$$W(s) = \left(\frac{2\pi f_c}{s + 2\pi f_c}\right)^3. \tag{4.59}$$

where $f_c = 1.5$ Hz. The resulting fitted model is denoted $\hat{G}_{x_r}(s)$.

Human-position-to-force dynamics: The dynamics $G_{x_h}(s)$, which maps human motion to the measured force and is required for the human-motion estimator in (4.14), was estimated from measured force f when the robot position was held stationary and the human manually excites the flexible object. The human position in these trials is measured by the motion capture system, and the force is measured at the robot end effector. The measured experimental response and that of the identified model are shown in Fig. 4.6.

The motion-capture measurement is used only for offline model identification and evaluation, not in the online control loop or the iterative update. The experiments test whether the robot can execute the repeated task using only force and robot-motion measurements once the object model has been identified. If the human-side dynamics are approximated by the lumped stiffness, $\hat{G}_{x_h} = K_{eq}$, the resulting spring-based estimate neglects the flexible-object dynamics and produces the larger estimation errors shown later in Fig. 4.8.

Both the force stream (sampled at 500 Hz) and the human position stream (from motion capture at 125 Hz) were then resampled onto a common uniform 125 Hz grid using linear interpolation.

A Welch-based FRF from human position $x_h(t)$ to force $F_x(t)$ was then computed using a Hann window with 20 s block length and 66% overlap to improve low-frequency resolution and reduce variance for the manually generated human-side excitation, which is less repeatable than the robot-side multisine excitation.

$$\hat{G}_{x_h}(j\omega) = \frac{S_{F_x x_h}(j\omega)}{S_{x_h x_h}(j\omega)}. \tag{4.60}$$

The corresponding magnitude-squared coherence was computed as

$$\gamma^2(\omega) = \frac{|S_{F_x x_h}(j\omega)|^2}{S_{x_h x_h}(j\omega)\, S_{F_x F_x}(j\omega)}. \tag{4.61}$$

Only frequency bins satisfying the coherence threshold were retained for fitting:

$$\gamma^2(\omega) \geq 0.4. \tag{4.62}$$

The forward model fit is 6th order with relative degree of 2. The resulting fit $\hat{G}_{x_h}(s)$ is shown in Fig. 4.6.

4.4.5 Iteration-Gain Design $\rho(\omega)$

The model uncertainty needed to find the allowable upper bound $\bar{\rho}(\omega)$ was estimated from the multiple experimentally identified feedforward models $\hat{G}_{ff}$, based on Eq. (4.17). The bound was computed as the minimum over the different model-identification trials i:

$$\bar{\rho}(\omega) = \min_i \left\{ \frac{2\cos\left(\angle\Delta_{ff,i}(j\omega)\right)}{|\Delta_{ff,i}(j\omega)|} \right\}, \tag{4.63}$$

which is shown in Fig. 4.7.

The nominal iteration gain $\rho_0 = 0.5$ was selected as a conservative value for the learning update. The uncertainty-based limit in Eq. (4.63) gives the largest real positive gain that satisfies the ideal contraction condition

$$W(\rho,\omega) = |1 - \rho(\omega)\Delta_{ff}(j\omega)| < 1, \tag{4.64}$$

where

$$\Delta_{ff}(j\omega) = \Delta_{ff,m}(\omega)e^{j\Delta_{ff,\theta}(\omega)}. \tag{4.65}$$

Thus,

$$0 < \rho(\omega) < \bar{\rho}(\omega), \qquad \bar{\rho}(\omega) = \frac{2\cos(\Delta_{ff,\theta}(\omega))}{\Delta_{ff,m}(\omega)}. \tag{4.66}$$

This upper bound is a stability limit, not an optimal iteration gain. For frequencies where $\cos(\Delta_{ff,\theta}) > 0$, minimizing the ideal squared iteration multiplier gives

$$\begin{aligned} \rho^\star(\omega) &= \arg\min_{\rho>0} \left|1 - \rho\Delta_{ff,m}e^{j\Delta_{ff,\theta}}\right|^2 && (4.67)\\ &= \arg\min_{\rho>0} \left[1 - 2\rho\Delta_{ff,m}\cos(\Delta_{ff,\theta}) + \rho^2\Delta_{ff,m}^2\right] && (4.68)\\ &= \frac{\cos(\Delta_{ff,\theta}(\omega))}{\Delta_{ff,m}(\omega)} = \frac{\bar{\rho}(\omega)}{2}. && (4.69)\end{aligned}$$

where $\rho^\star$ is the ideal minimizing gain. A theoretical upper bound of $\bar{\rho} = 1.9$ corresponds to an ideal gain of $\rho^\star = 0.95$. The physical experiment uses an estimated tracking error and the human motion is only approximately repeated across trials, so a gain below this ideal value was selected. As discussed in Remark 4, estimator error and trial-to-trial human variability enter the iteration as disturbances, including an estimator-error term that is scaled by ρ. For the nominal model, $\rho_0 = 0.5$ gives $W = |1 - \rho_0| = 0.5$, so the repeatable component of the error is halved on each update. The selected value provides useful learning while maintaining margin against human-position-estimation error and imperfect human repeatability.

The gain ρ was then selected to be frequency dependent:

$$\rho = \begin{cases} 0, & \omega/(2\pi) < 0.05 \text{ Hz}, \\ \rho_0 = 0.5, & 0.10 \text{ Hz} \leq \ \omega/(2\pi) \leq 2.00 \text{ Hz}, \\ 0, & \omega/(2\pi) > 2.10 \text{ Hz}, \end{cases} \tag{4.70}$$

and linearly interpolated over the intervals [0.05, 0.10] Hz and [2.00, 2.10] Hz to avoid sharp spectral edges. The upper frequency bound of the iteration gain is near the voluntary human bandwidth [19] and the lower frequency bound acts as a high-pass filter to reduce force sensor drift.

4.5 Experimental Results

4.5.1 Multi-User Summary Metrics

The results below summarize the seven-subject preview-tracking experiment described in Fig. 4.5. The left panels in Figs. 4.8–4.10 show representative first- and final-iteration time traces, while the right panels summarize RMS metrics over all trials at each iteration index k. Error bars denote the standard deviation across trials at that iteration. This captures both learning across iterations and the subject-to-subject variability in how the previewed trajectory was executed.

4.5.2 Human Position Estimate

The human position is estimated from the measured interaction force and robot motion using the identified flexible-object dynamics in Eq. (4.14). This estimate is computed after each trial in the Fourier domain using Eq. (4.15). Fig. 4.8 compares the measured human

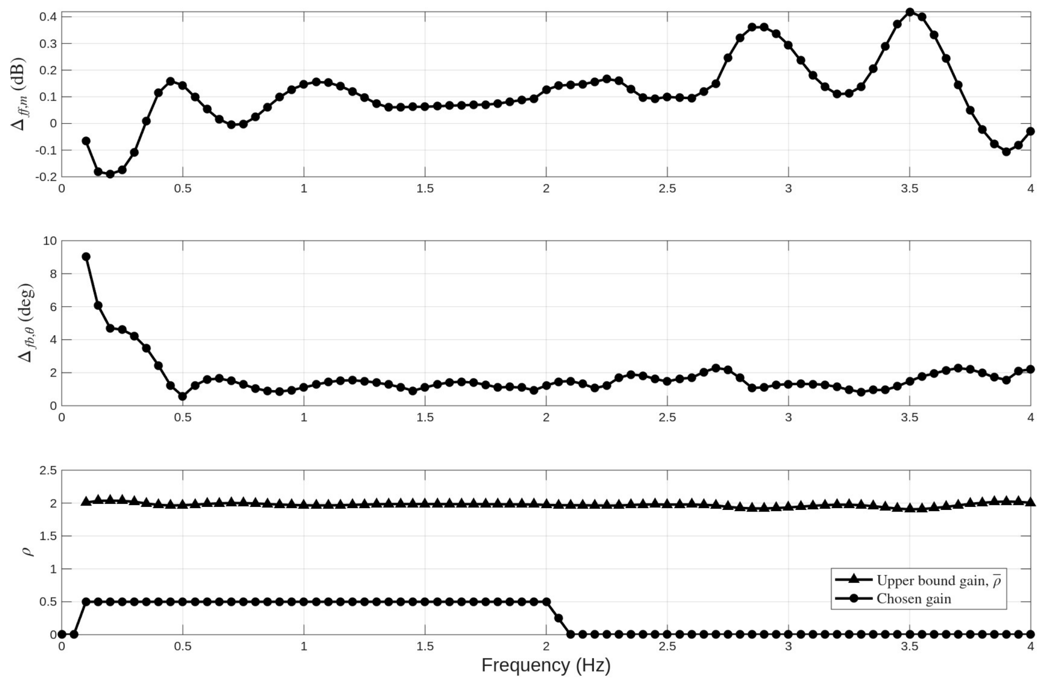

Figure 4.7: Model uncertainty Δ_{ff} in magnitude and phase of $G_{ff}(j\omega)$ in Eq. (4.32) (top, middle). Maximum theoretical learning gain $\bar{\rho}$ from Eq. (4.33) (bottom, triangles) and chosen learning gain (bottom, circles).

motion with the dynamics-based and spring-based estimates for the first and final iterations, and summarizes the RMS estimation error across the seven-subject study. In the first iteration, the spring-based estimate shows larger errors, while the dynamics-based estimate more closely follows the measured trajectory. However, the dynamics-based estimate is still imperfect initially because the object is operating in a relatively deformed state that differs from the low-deformation condition used during system identification. Figure 4.8 shows this effect quantitatively: the RMS estimation error of the dynamics-based estimate decreases by approximately 53% from the initial to the final iteration. This shows the estimator becomes more accurate as the iterative update reduces deformation and moves the object closer to

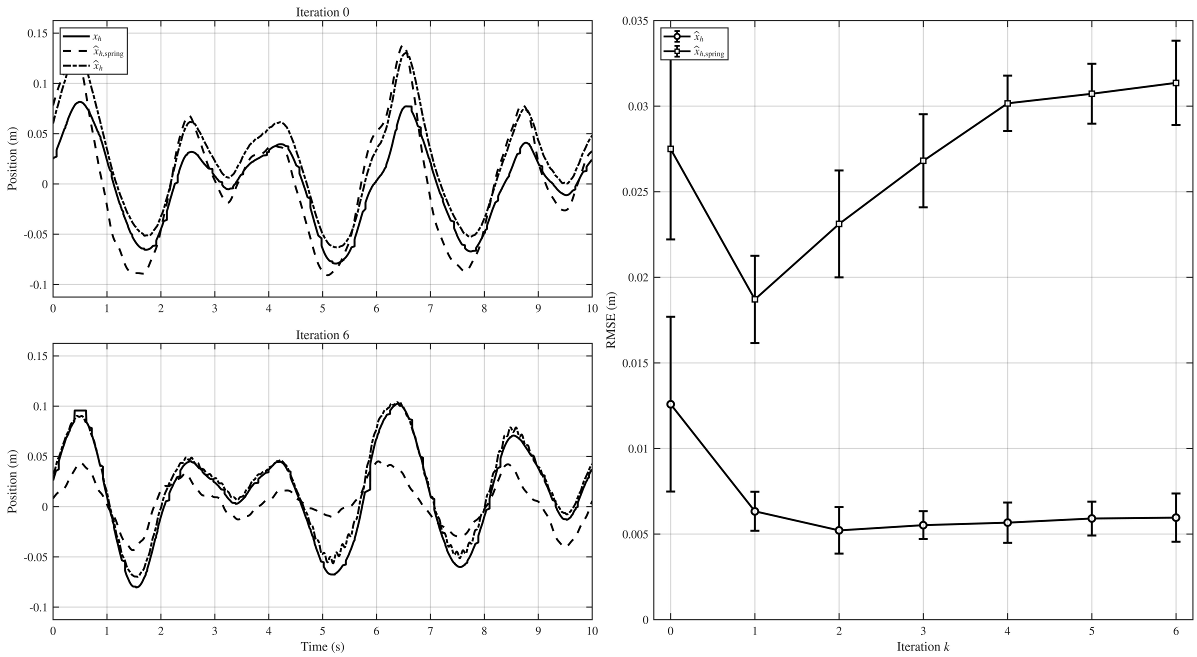

Figure 4.8: Estimate of human motion, $\hat{x}_h$, using dynamics-based estimate in (4.14), and lumped spring-based estimate $\hat{x}_{h,spring}$ in (4.12): (left) for the first iteration (top) and final iteration (bottom); and (right) RMS estimation error over iteration steps k across the $N_u = 7$ subjects. Error bars denote the standard deviation across trials at each iteration.

the condition where the dynamics were identified. By the final iteration, the dynamics-based estimate is nearly coincident with the measured motion over most of the trajectory, whereas the spring-based estimate still shows visible errors. The corresponding numerical values are listed in Table 4.1.

4.5.3 Improvement with Iterative Update

Figure 4.9 compares the human position x_h and the robot position x_r for the zeroth iteration (standard admittance control) and the final iteration, and summarizes the RMS deformation across the seven-subject study. Starting from the initial execution (iteration $k = 0$) under admittance alone, the iterative update progressively reduces deformation by 79%. In

Table 4.1: Human-position estimation error corresponding to the right panel of Fig. 4.8. Entries are mean $\pm$ standard deviation across trials, reported in centimeters.

Iteration k	Dynamics-based estimate	Spring-based estimate
0	1.24 ± 0.51	2.72 ± 0.53
1	0.65 ± 0.11	1.90 ± 0.26
2	0.52 ± 0.14	2.31 ± 0.31
3	0.55 ± 0.08	2.68 ± 0.27
4	0.57 ± 0.12	3.01 ± 0.16
5	0.59 ± 0.10	3.07 ± 0.18
6	0.59 ± 0.14	3.13 ± 0.25

the representative time traces, the robot motion lags the human motion during the initial admittance-only trial, while the final learned trajectory is nearly coincident with the human motion. In the aggregate results, most of the deformation reduction occurs over the first several learned updates, after which the RMS deformation remains near its final low value. This nonzero residual is expected because estimator error, model mismatch, and imperfect human repeatability prevent exact convergence to zero deformation in the physical experiment.

Reduction beyond human tracking error: The flexible-object deformation $\delta = x_h - x_r$ is reduced to a level below the human reference-tracking error, i.e., the error $x_h - x_{ref}$ between human position x_h and the reference trajectory x_{ref}. Fig. 4.10 shows that the human position tracking error $x_h - x_{ref}$ also decreases across iterations, which is expected because subjects repeat the same preview-tracking task. The object deformation δ is reduced further than the reduction in human reference tracking error, as shown in Fig. 4.9. By the final iteration, the RMS deformation is below the RMS human tracking error. The corresponding deformation and tracking metrics are listed in Table 4.2.

4.6 MC2: Conclusion

MC2 developed an iterative method for human-robot co-transport of flexible objects without requiring cameras or other external sensing in the control loop. During each trial, the online controller remains an admittance controller. Between trials, the robot estimates human motion from measured force and robot motion, then updates a learned feedforward correction using the identified flexible-object dynamics. Experiments across seven subjects using a preview-tracking display showed that object deformation was reduced by 79% relative to the initial admittance-only execution. The final learned behavior also reduced deformation below the human RMS reference-tracking error, indicating that repeated interaction can isolate consistent human intent and improve performance beyond a single execution. These

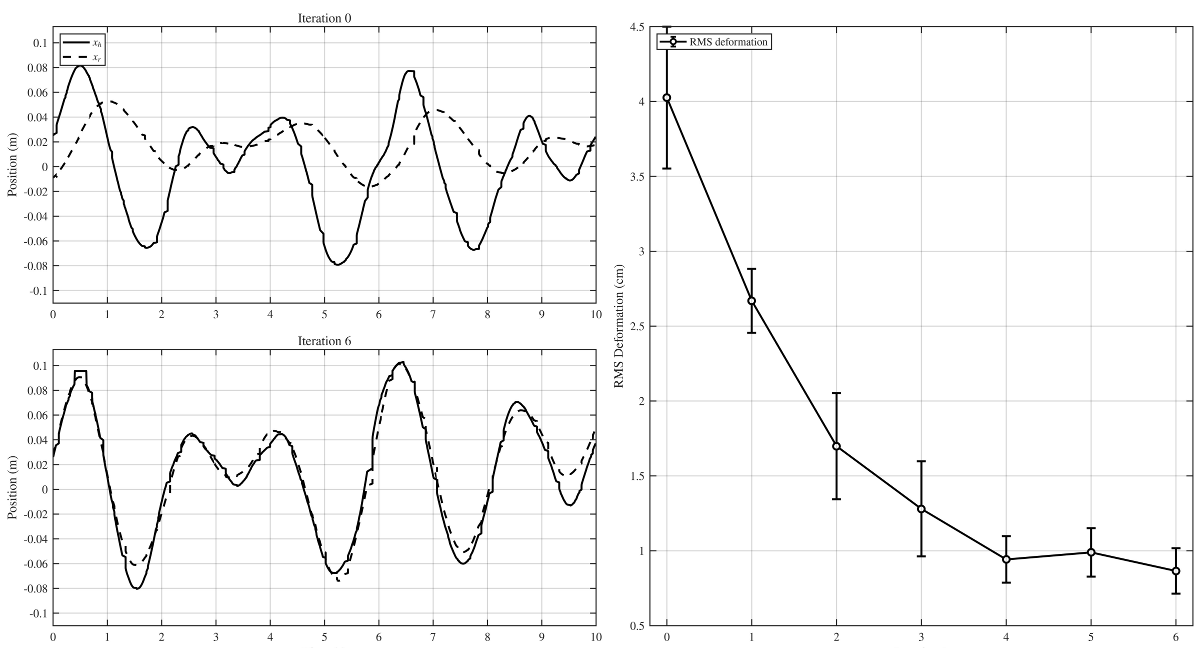

Figure 4.9: Object deformation. Left: human position x_h and robot position x_r for the first iteration (top) and final iteration (bottom). Right: RMS deformation over iteration steps k across the $N_u = 7$ subjects; error bars denote the standard deviation across trials at each iteration of deformation $\delta = x_h - x_r$.

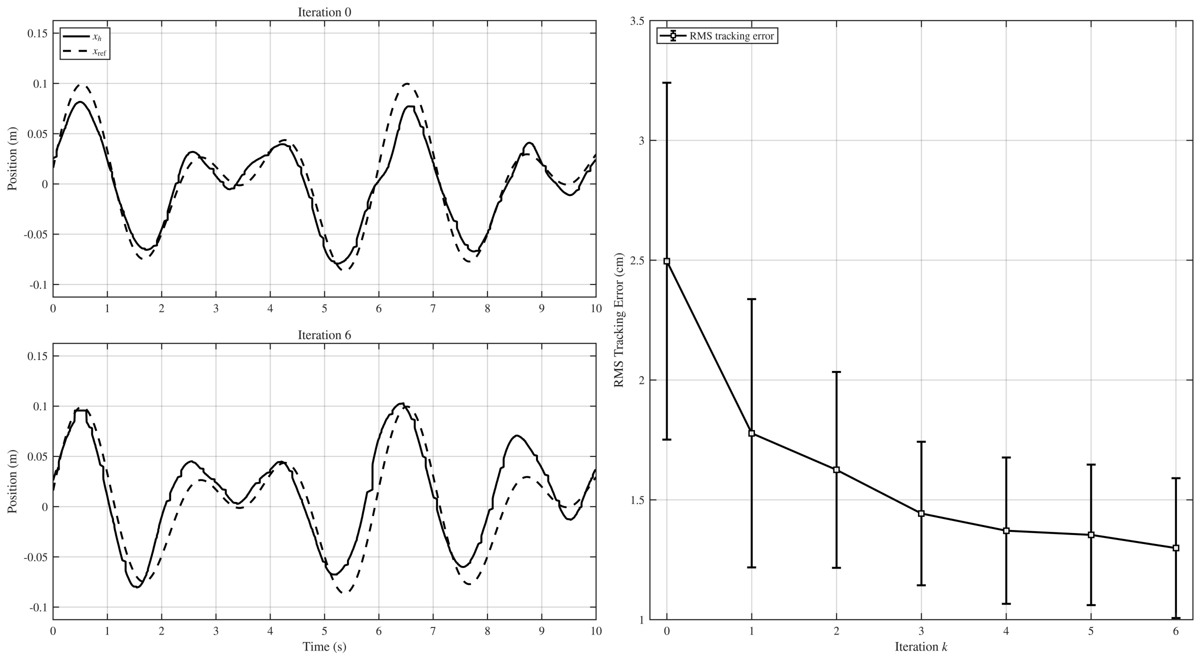

Figure 4.10: Human reference-tracking error. Left: human position x_h (from motion capture) vs. previewed reference trajectory x_{ref} for the first iteration (top) and final iteration (bottom). Right: RMS reference-tracking error $x_h - x_{ref}$ over iteration steps k across the $N_u = 7$ subjects; error bars denote the standard deviation across trials at each iteration.

results show that iterative control can improve flexible object transport when direct human motion sensing is unavailable.

Table 4.2: RMS deformation and human reference-tracking error corresponding to the right panels of Figs. 4.9 and 4.10. Entries are mean $\pm$ standard deviation across trials, reported in centimeters.

Iteration k	RMS deformation	RMS tracking error
0	3.98 ± 0.40	2.47 ± 0.75
1	2.69 ± 0.21	1.80 ± 0.56
2	1.72 ± 0.36	1.62 ± 0.41
3	1.28 ± 0.32	1.44 ± 0.30
4	0.95 ± 0.16	1.37 ± 0.31
5	0.99 ± 0.16	1.35 ± 0.29
6	0.86 ± 0.15	1.30 ± 0.29

Chapter 5

CONCLUSION AND FUTURE WORK

5.1 Summary

This thesis studied force-based human-robot co-transport of flexible objects using the force sensing already available on many industrial manipulators. Flexible objects introduce dynamics that limit the performance of existing force-based methods. MC1 improves the online controller when the object modes are high enough in frequency relative to the human interaction bandwidth. MC2 addresses repeated tasks where the object dynamics sit closer to the range of human motion, using an iterative feedforward correction computed between trials.

5.1.1 MC1: Dynamics-Compensated Admittance Control

MC1 showed that lowering the admittance is not the only way to keep the interaction stable. For the flexible beam used in Chapter 3, the object dynamics were high frequency, so they could be compensated directly inside the admittance controller. This allowed the robot to behave more responsively without crossing into the unstable region that appears with standard admittance control. The experiment showed a 45% reduction in normalized RMS deformation compared with standard admittance control.

5.1.2 MC2: Human-Motion Estimation and Iterative Learning

MC2 addressed the case where the flexible dynamics are in the same frequency range as human motion. After each trial, the robot used the measured force and its own motion to estimate the human position. That estimate was then used to update a feedforward correction for the next trial. During each trial, the online controller remained an admittance controller, while the model inversion was applied between trials.

In the seven-subject preview-tracking experiment, the dynamics-based human-position estimate was much more accurate than the spring approximation. The iterative update reduced RMS deformation by 79% relative to the initial admittance-only trial. By the final iteration, the deformation was also below the human RMS reference-tracking error, showing that repeated interaction can extract the repeatable part of the human motion from force data and use it to improve co-transport without direct human-motion sensing in the control loop.

5.2 Future Work

5.2.1 Limitations of Force-Based Modeling

A limitation of this thesis is that the proposed methods were evaluated on flexible structures that produced a measurable, repeatable force response at the robot. These methods rely on the force/torque sensor to provide enough information about the flexible-object dynamics. Therefore, future work should identify when this force-based assumption breaks down. One likely case where this fails is low force signal-to-noise ratio. As the object becomes more compliant, or as the required deformation becomes smaller, the repeatable force caused by object deformation may approach the noise floor and resolution limits of the force/torque sensor. In that case, the identified models G_{xr} and G_{xh} may become unreliable, and inverse-model compensation or human-motion estimation can amplify sensor noise rather than recover meaningful deformation information. A future study should therefore determine the practical limits of object stiffness and force sensor resolution where the methods can be applied. Some materials are clearly outside the range of the current force-only approach. Cloth, slack rope, and other materials with hysteresis can change shape without producing a reliable force at the robot. Rope is one example: motion in one direction creates tension and a measurable force, while motion in the opposite direction can produce little or no signal. In these cases, the robot-side force will not contain enough information to estimate human motion or object deformation, so additional sensing such as vision or motion capture is required.

Another limitation is the assumption of linear models in the analysis. The physical object does not need to be globally linear, but it must behave approximately linearly over the range of deformation used for control or learning. The iterative method in MC2 may still work for moderately nonlinear objects if each update reduces deformation and moves the object toward a region where the local linear model is more accurate. However, this convergence has not been proven. Future work should analyze nonlinear force-motion relationships in which G_{xh} and G_{xr} are local approximations rather than global linear models. The analysis should determine when repeated learning keeps the system within the same local model region, and when low signal-to-noise ratio or hysteresis prevent convergence.

5.2.2 Model Identification Without Motion Capture

A key next step is to remove the remaining dependence on motion capture during model identification. The robot-side force response used in MC1 and MC2 can already be identified from robot motion and force measurements. The remaining deployment challenge is the human-side force response, which was identified in Chapter 4 using measured human motion from motion capture. Since this human-side response is needed for the human-motion estimator in MC2, the next step is to estimate it without directly measuring the human position. One approach is to infer the human-side response from the robot-side response and a flexible-object model. Robot-side motions could identify the dominant flexible modes, damping, and effective stiffness of the object. A reduced-order physical model could then be fit to these data and used to predict the corresponding human-side response.

5.2.3 Robust Online Use of the Human-Motion Estimate

MC2 used the human-motion estimate between trials rather than as a direct online tracking signal. Appendix B showed why the human estimate was not used online: placing the estimate directly inside the feedback loop can make the system sensitive to small modeling errors, especially near flexible modes. A useful next step may be to use the estimate as an outer-loop assistance signal. The robot could continue to respond primarily through admittance control, while the model-based estimate provides a filtered correction when the model is reliable. If the force signal shows unexpected vibration, or if the measured force no longer agrees well with the model prediction, the correction could be reduced and the robot could return toward standard admittance behavior. The goal would not be perfect online reconstruction of human motion as in MC2, but rather an improvement over standard admittance control similar to MC1, but applied online to objects where the dynamics are low frequency.

5.2.4 Multi-axis and Multi-robot Transport

The experiments in this thesis were limited to a single axis. Chapter 3 used a sinusoidal task to provide a baseline for comparison. Chapter 4 used a repeated multisine preview-tracking task to evaluate the human-motion estimation and iterative learning update. These experiments were useful for validating MC1 and MC2, but practical co-transport will involve less structured motion. Appendix A describes the six-degree-of-freedom robot platform with force and torque sensing, which would allow experiments with motion in multiple axes. This extension would replace the scalar transfer functions in Chapters 3 and 4 with matrix-valued models that map Cartesian motion to measured force and torque.

The same idea can be extended to multi-robot flexible-object transport, but the model identification problem becomes larger. Suppose a leader, either a human or a leader robot, moves the object while N follower robots grasp other locations. Let x_L denote the leader motion, x_i denote the motion of follower robot i, and f_i denote the force measured by follower robot i. A direct extension of the force model used in this thesis is

$$f_i(s) = G_{iL}(s)x_L(s) - G_{ii}(s)x_i(s) - \sum_{\substack{j=1 \\ j\neq i}}^{N} G_{ij}(s)x_j(s) \tag{5.1}$$

where G_{ii} is the local self-response at robot i, similar to G_{xr} in this thesis; G_{iL} maps leader motion to the force measured at robot i, similar to G_{xh}; G_{ij} captures the effect of follower robot j on the force measured by follower robot i. The multi-robot case would require identifying not only a local stiffness or local dynamics model for each robot, but also the leader-to-follower and follower-to-follower coupling through the flexible object. Therefore, in a multi-axis, multi-robot application, the system identification problem grows substantially. The DSR methods reviewed in Chapter 2 are attractive because they reduce deformation without requiring full communication, but they rely on stiffness-based behavior and have been demonstrated at slow transport speeds. The methods in this thesis suggest a possible way to move faster: replace the quasi-static force-displacement model with a dynamic force model that includes flexible modes. Future work should test whether dynamics compensation or iterative feedforward learning can increase the speed of multi-robot flexible-object transport while still limiting deformation and internal force.

BIBLIOGRAPHY

[1] Arash Ajoudani, Andrea Maria Zanchettin, Serena Ivaldi, Alin Albu-Schäffer, Kazuhiro Kosuge, and Oussama Khatib. Progress and prospects of the human–robot collaboration. *Autonomous robots*, 42:957–975, 2018.

[2] Doganay Sirintuna, Theodora Kastritsi, Idil Ozdamar, Juan M Gandarias, and Arash Ajoudani. Enhancing human–robot collaborative transportation through obstacle-aware vibrotactile warning and virtual fixtures. *Robotics and Autonomous Systems*, 178:104725, 2024.

[3] Martín Mujica, Martín Crespo, Mourad Benoussaad, Sergio Junco, and Jean-Yves Fourquet. Robust variable admittance control for human–robot co-manipulation of objects with unknown load. *Robotics and Computer-Integrated Manufacturing*, 79:102408, 2023.

[4] L. Roveda, N. Castaman, S. Ghidoni, P. Franceschi, N. Boscolo, E. Pagello, and N. Pedrocchi. Human-robot cooperative interaction control for the installation of heavy and bulky components. In *Proc. IEEE Int. Conf. on Systems, Man, and Cybernetics (SMC)*, pages 339–344, 2018.

[5] A. Bussy, P. Gergondet, A. Kheddar, F. Keith, and A. Crosnier. Proactive behavior of a humanoid robot in a haptic transportation task with a human partner. In *Proc. 21st IEEE Int. Symp. on Robot and Human Interactive Communication (RO-MAN)*, pages 962–967, 2012.

[6] D. J. Agravante, A. Cherubini, A. Bussy, P. Gergondet, and A. Kheddar. Collaborative human-humanoid carrying using vision and haptic sensing. In *Proc. IEEE Int. Conf. on Robotics and Automation (ICRA)*, pages 607–612, 2014.

[7] X. Yu, W. He, Q. Li, Y. Li, and B. Li. Human-robot co-carrying using visual and force sensing. *IEEE Transactions on Industrial Electronics*, 68(9):8657–8666, 2021.

[8] T. Tsumugiwa, R. Yokogawa, and K. Yoshida. Stability analysis for impedance control of robot for human-robot cooperative task system. In *2004 IEEE/RSJ International Conference on Intelligent Robots and Systems (IROS) (IEEE Cat. No.04CH37566)*, volume 4, pages 3883–3888 vol.4, 2004.

[9] Chris A. C. Parker and Elizabeth A. Croft. Design & personalization of a cooperative carrying robot controller. In *2012 IEEE International Conference on Robotics and Automation*, pages 3916–3921, 2012.

[10] D. Sirintuna, A. Giammarino, and A. Ajoudani. An object deformation-agnostic framework for human–robot collaborative transportation. *IEEE Transactions on Automation Science and Engineering*, 21(2):1986–1999, 2024.

[11] Doganay Sirintuna, Idil Ozdamar, and Arash Ajoudani. Carrying the uncarriable: a deformation-agnostic and human-cooperative framework for unwieldy objects using multiple robots. In *2023 IEEE International Conference on Robotics and Automation (ICRA)*, pages 7497–7503, 2023.

[12] Giovanni Cortigiani, Monica Malvezzi, Domenico Prattichizzo, and Maria Pozzi. Human-robot collaborative cable-suspended manipulation with contact distinction. *IEEE Robotics and Automation Letters*, 10(1):740–747, 2025.

[13] Hang Yin, Anastasia Varava, and Danica Kragic. Modeling, learning, perception, and control methods for deformable object manipulation. *Science Robotics*, 6(54):eabd8803, 2021.

[14] Matteo Terreran, Alberto Gottardi, Emanuele Menegatti, and Stefano Ghidoni. Human-robot collaborative transportation via distance-based role allocation for precise positioning of flexible materials. In *2024 IEEE 29th International Conference on Emerging Technologies and Factory Automation (ETFA)*, pages 1–8, 2024.

[15] Daniel Kruse, Richard J. Radke, and John T. Wen. Collaborative human-robot manipulation of highly deformable materials. In *2015 IEEE International Conference on Robotics and Automation (ICRA)*, pages 3782–3787, 2015.

[16] Giorgio Nicola, Stefano Mutti, Enrico Villagrossi, and Nicola Pedrocchi. Depth image-based deformation estimation of deformable objects for collaborative mobile transportation. In *2023 32nd IEEE International Conference on Robot and Human Interactive Communication (RO-MAN)*, pages 2658–2664, 2023.

[17] Alexandre Lecours, Boris Mayer-St-Onge, and Clément Gosselin. Variable admittance control of a four-degree-of-freedom intelligent assist device. In *2012 IEEE International Conference on Robotics and Automation*, pages 3903–3908, 2012.

[18] V. Duchaine and C. M. Gosselin. Safe, stable and intuitive control for physical human-robot interaction. In *Proc. IEEE Int. Conf. on Robotics and Automation (ICRA)*, pages 3383–3388, 2009.

[19] E. J. Perreault, R. F. Kirsch, and P. E. Crago. Effects of voluntary force generation on the elastic components of endpoint stiffness. *Exp. Brain Res.*, 141:312–323, 2001.

[20] Joseph DelPreto and Daniela Rus. Sharing the load: Human-robot team lifting using muscle activity. In *2019 international conference on robotics and automation (ICRA)*, pages 7906–7912. IEEE, 2019.

[21] Leigh R Hochberg, Daniel Bacher, Beata Jarosiewicz, Nicolas Y Masse, John D Simeral, Joern Vogel, Sami Haddadin, Jie Liu, Sydney S Cash, Patrick Van Der Smagt, et al. Reach and grasp by people with tetraplegia using a neurally controlled robotic arm. *Nature*, 485(7398):372–375, 2012.

[22] Elio Tuci, Muhanad H. M. Alkilabi, and Otar Akanyeti. Cooperative object transport in multi-robot systems: A review of the state-of-the-art. *Frontiers in Robotics and AI*, 5, 2018.

[23] M. Koga, K. Kosuge, K. Furuta, and K. Nosaki. Coordinated motion control of robot arms based on the virtual internal model. *IEEE Transactions on Robotics and Automation*, 8(1):77–85, 1992.

[24] Kazuhiro Kosuge and Tomohiro Oosumi. Decentralized control of multiple robots handling an object. In *Proceedings of IEEE/RSJ International Conference on Intelligent Robots and Systems. IROS'96*, volume 1, pages 318–323. IEEE, 1996.

[25] G. Montemayor and J.T. Wen. Decentralized collaborative load transport by multiple robots. In *Proceedings of the 2005 IEEE International Conference on Robotics and Automation*, pages 372–377, 2005.

[26] Yoshua Gombo, Anuj Tiwari, and Santosh Devasia. Accelerated-gradient-based flexible-object transport with decentralized robot teams. *IEEE Robotics and Automation Letters*, 6(1):151–158, 2021.

[27] Yoshua Gombo, Anuj Tiwari, Mohamed Safwat, Henry Chang, and Santosh Devasia. Delayed self-reinforcement to reduce deformation during decentralized flexible-object transport. *IEEE Transactions on Robotics*, 40:999–1018, 2024.

[28] Yoshua Gombo, Anuj Tiwari, Mohamed Safwat, Henry Chang, and Santosh Devasia. Communication-free decentralized controller design for flexible object transport. *IEEE/ASME Transactions on Mechatronics*, 29(4):2973–2982, 2024.

[29] N. Hogan. Impedance control: An approach to manipulation. part I–theory. *Journal of Dynamic Systems, Measurement, and Control*, 107(1):1–7, 1985.

[30] A. Q. L. Keemink, H. van der Kooij, and A. H. A. Stienen. Admittance control for physical human–robot interaction. *International Journal of Robotics Research*, 37(11):1421–1444, 2018.

[31] X. Guo, Z. Liu, V. Crocher, Y. Tan, D. Oetomo, and A. H. A. Stienen. Ultimate passivity: Balancing performance and stability in physical human-robot interaction. *IEEE Transactions on Robotics*, 41:2050–2066, 2025.

[32] A. Jafari and J. H. Ryu. Input-to-state stable approach to release the conservatism of passivity-based stable haptic interaction. In *2015 IEEE International Conference on Robotics and Automation (ICRA)*, pages 285–290, 2015.

[33] R. Ikeura and H. Inooka. Variable impedance control of a robot for cooperation with a human. In *Proc. IEEE Int. Conf. on Robotics and Automation (ICRA)*, pages 3097–3102, 1995.

[34] S. Grafakos, F. Dimeas, and N. Aspragathos. Variable admittance control in pHRI using EMG-based arm muscles co-activation. In *Proc. IEEE Int. Conf. on Systems, Man, and Cybernetics (SMC)*, pages 003900–003905, 2016.

[35] F. Ferraguti, C. Talignani Landi, L. Sabattini, M. Bonfè, C. Fantuzzi, and C. Secchi. A variable admittance control strategy for stable physical human–robot interaction. *International Journal of Robotics Research*, 38(6):747–765, 2019.

[36] Chiara Talignani Landi, Federica Ferraguti, Cristian Secchi, and Cesare Fantuzzi. Tool compensation in walk-through programming for admittance-controlled robots. In *IECON 2016 - 42nd Annual Conference of the IEEE Industrial Electronics Society*, pages 5335–5340, 2016.

[37] S. Farsoni, C. Talignani Landi, F. Ferraguti, C. Secchi, and M. Bonfè. Compensation of load dynamics for admittance controlled interactive industrial robots using a quaternion-based Kalman filter. *IEEE Robotics and Automation Letters*, 2(2):672–679, 2017.

[38] K. Samuel, K. Haninger, and S. Oh. High-performance admittance control of an industrial robot via disturbance observer. pages 1–6, 2022.

[39] K. Samuel, K. Haninger, and S. Oh. Increasing admittance of industrial robots by velocity feedback inner-loop shaping. pages 5228–5234, 2023.

[40] K. Haninger, M. Radke, A. Vick, and J. Krüger. Towards high-payload admittance control for manual guidance with environmental contact. *IEEE Robotics and Automation Letters*, 7(2):4275–4282, 2022.

[41] E. Noohi, M. Zefran, and J. L. Patton. A model for human-human collaborative object manipulation and its application to human-robot interaction. *IEEE Transactions on Robotics*, 32(4):880–896, 2016.

[42] J. Zhu, A. Cherubini, C. Dune, D. Navarro-Alarcon, F. Alambeigi, D. Berenson, F. Ficuciello, K. Harada, J. Kober, X. Li, J. Pan, W. Yuan, and M. Gienger. Challenges and outlook in robotic manipulation of deformable objects. *IEEE Robotics & Automation Magazine*, 29(3):67–77, 2022.

[43] N. Lv, J. Liu, and Y. Jia. Dynamic modeling and control of deformable linear objects for single-arm and dual-arm robot manipulations. *IEEE Transactions on Robotics*, 38(4):2341–2353, 2022.

[44] Dionisis Andronas, Emmanouil Kampourakis, Katerina Bakopoulou, Christos Gkournelos, Panagiotis Angelakis, and Sotiris Makris. Model-based robot control for human-robot flexible material co-manipulation. In *2021 26th IEEE International Conference on Emerging Technologies and Factory Automation (ETFA)*, pages 1–8, 2021.

[45] Douglas A. Bristow, Marina Tharayil, and Andrew G. Alleyne. A survey of iterative learning control: A learning-based method for high-performance tracking control. *IEEE Control Systems Magazine*, 26(3):96–114, 2006.

[46] Hyo-Sung Ahn, YangQuan Chen, and Kevin L. Moore. Iterative learning control: Brief survey and categorization. *IEEE Transactions on Systems, Man, and Cybernetics, Part C (Applications and Reviews)*, 37(6):1099–1121, 2007.

[47] S. Tien, Q. Zou, and S. Devasia. Iterative control of dynamics-coupling-caused errors in piezoscanners during high-speed AFM operation. *IEEE Transactions on Control Systems Technology*, 13(6):921–931, Nov 2005.

[48] Rahul B. Warrier and Santosh Devasia. Iterative learning from novice human demonstrations for output tracking. *IEEE Transactions on Human-Machine Systems*, 46(4):510–521, 2016.

[49] Rahul B. Warrier and Santosh Devasia. Inferring intent for novice human-in-the-loop iterative learning control. *IEEE Transactions on Control Systems Technology*, 25(5):1698–1710, 2017.

[50] Kyle Schultz and Santosh Devasia. Improving admittance controller human-robot co-transport performance by correcting for flexible object dynamics. In *Indian Control Conference, Bangalore*, 2025.

[51] R.Wade Allen and Duane McRuer. The man/machine control interface–pursuit control. *Automatica*, 15(6):683–686, 1979.

[52] Kyle Schultz, Alex M. Turner, Logan Castro, and Santosh Devasia. Human action estimation and iterative admittance-controller correction for human-robot flexible-object co-transport. *ASME Letters in Dynamic Systems and Control*, 2026.

[53] André Preumont. *Vibration control of active structures: an introduction*. Springer, 2002.

[54] Kasper van der El, Daan M. Pool, Herman J. Damveld, Marinus M. van Paassen, and Max Mulder. An empirical human controller model for preview tracking tasks. *IEEE Transactions on Cybernetics*, 46(11):2609–2621, 2016.

[55] Ljung Lennart. System identification: theory for the user. *PTR Prentice Hall, Upper Saddle River, NJ*, 28:540, 1999.

[56] Benson H. Tongue. *Principles of Vibration*. Oxford University Press, New York, 2 edition, 2002.

Appendix A

EXPERIMENTAL PLATFORM

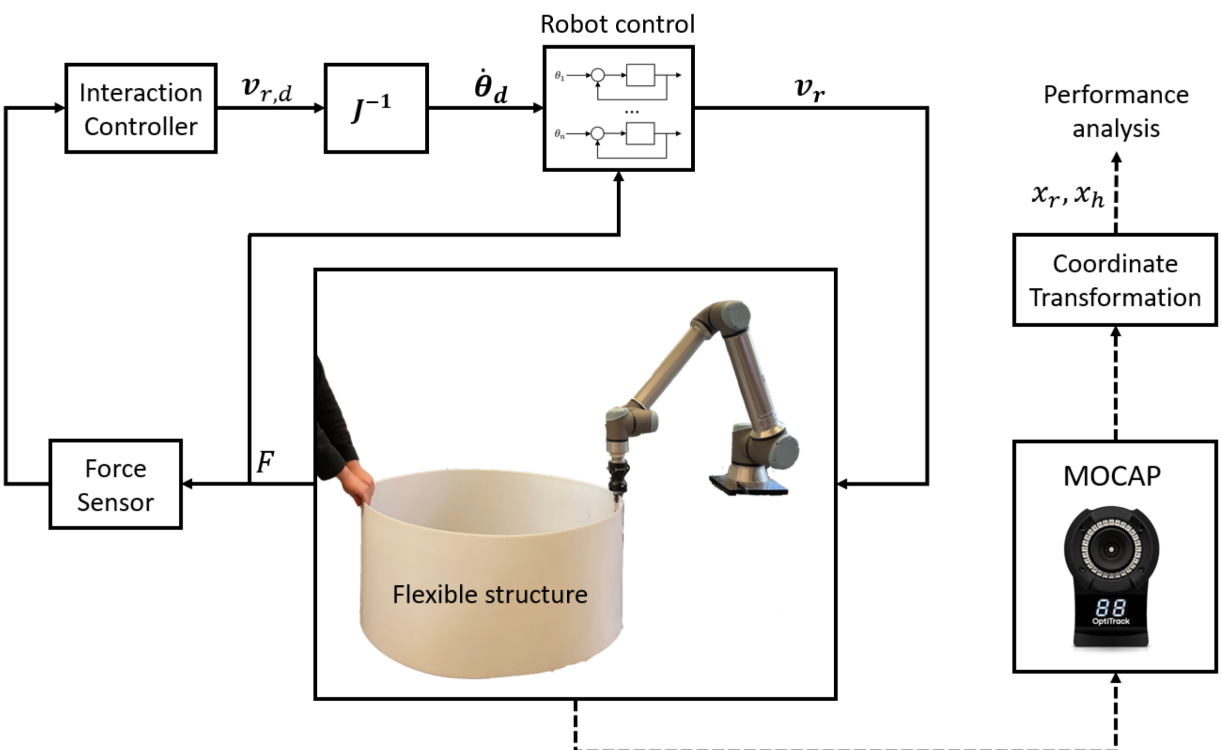

Figure A.1: Block diagram of the experimental pHRI platform. A human operator and a 6-DOF robot jointly manipulate a flexible object. The interaction force $\boldsymbol{F}$ sensed at the robot wrist is processed by an interaction controller that outputs a Cartesian reference velocity $\boldsymbol{v}_{r,d}$. The inverse Jacobian converts $\boldsymbol{v}_{r,d}$ to joint-space commands $\dot{\boldsymbol{\theta}}_d$, which are executed by the robot's internal velocity loops to realize the end-effector velocity $\boldsymbol{v}_r$. A marker-based motion-capture system records human and robot kinematics for offline analysis.

The experimental platform used in this thesis is illustrated in Fig. A.1. A human collaborator and a six-degree-of-freedom industrial manipulator grasp the ends of an elastic structure that serves as the physical coupling between them. Deformation of the structure gives rise to an interaction force $\boldsymbol{F}$ that is measured by a six-axis force/torque sensor mounted at the robot end effector. This force measurement is supplied to an interaction controller, which computes the desired Cartesian end-effector velocity $\boldsymbol{v}_{r,d}$. The inverse manipulator Jacobian maps $\boldsymbol{v}_{r,d}$ to the desired joint-space velocity vector $\dot{\boldsymbol{\theta}}_d$. These joint-velocity commands are executed by the robot's internal velocity loop, generating the realized end-effector velocity $\boldsymbol{v}_r$ and closing the pHRI control loop. An external optical motion capture system tracks the human and robot positions for model identification, the MC2 participant display, and performance evaluation. Human-position measurements are not supplied to the robot controller or the MC2 learning update during task execution. The following sections describe the experimental platform in more detail.

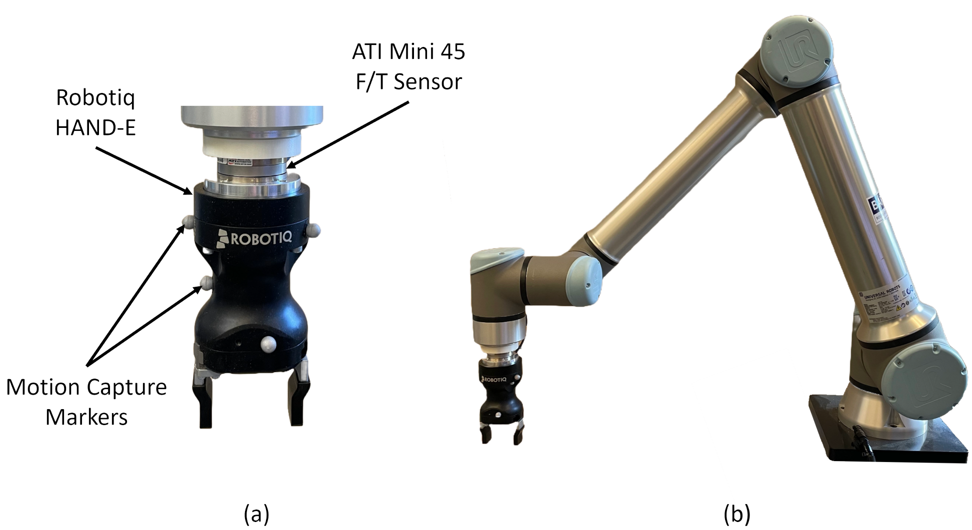

Figure A.2: Labeled robot platform showing: (a) the end effector with gripper, motion capture markers, and force/torque sensor, and (b) the UR10e robot in its home position.

A.1 Force Sensor

The force/torque (F/T) sensor is an ATI mini-45 with a SI-290-10 calibration. It is sampled at 500 Hz using a local network connection. The F/T sensor is mechanically aligned with the robot TCP axes using a custom coupler plate. It is attached between the gripper and the robot tool flange, as shown in Fig. A.2.

A.2 Robot Platform

A.2.1 Robot Kinematics

Communication with the Universal Robots UR10e is established via TCP/IP using the RTDE protocol. Commands are transmitted from a Linux system running a real-time kernel. A high-frequency 500 Hz control loop computes and sends the desired joint velocities to the robot controller. These joint velocities are determined by the inverse manipulator Jacobian matrix,

$$\dot{\theta} = J^{-1}(\boldsymbol{\theta})\dot{\boldsymbol{x}}_d, \tag{A.1}$$

where

- $J \in \mathbb{R}^{6\times 6}$ is the manipulator Jacobian matrix
- $\boldsymbol{\theta} \in \mathbb{R}^6$ is the vector of joint angles for the six-degree-of-freedom (DOF) robot
- $\dot{\boldsymbol{x}}_d \in \mathbb{R}^6$ is the desired tool center point (TCP) velocity vector

A.2.2 Robot Motion Controller

Since the dynamical model of the robot is not provided by the manufacturer, it is obtained experimentally along the horizontal axis for a specific joint configuration. We command a desired robot velocity, $\boldsymbol{v}_{r,d} = (v_{r,d}, ..., 0)$, and measure the actual velocity, $\boldsymbol{v}_r = (v_r, ..., 0)$, to find the transfer function $G_r(s)$.

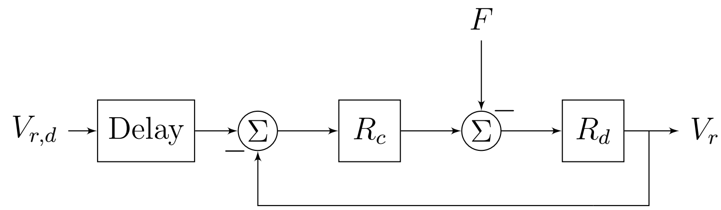

Figure A.3: Block diagram of robot motion controller model.

We assume a grey-box form of the robot velocity controller consisting of a time delay, a PI controller, and a damped mass. The delay system is first estimated from the step response by averaging over three step trials. We use a first-order Pade approximation of the delay,

$$e^{-\tau_d s} \approx \frac{2 - \tau_d s}{2 + \tau_d s} \tag{A.2}$$

where the delay is $\tau_d = 8\,\mathrm{ms}$. The robot controller and dynamics are given by

$$R_d(s) = \frac{1}{m_r s + b_r}, \tag{A.3}$$

$$R_c(s) = \frac{K_i}{s} + K_p, \tag{A.4}$$

The block diagram of the robot controller is shown in Fig. A.3. To determine the robot's frequency response, a sine-wave testing approach is used [55]. The robot controller receives a sinusoidal reference velocity,

$$v_{r,d}(t) = m\cos(\omega t) \tag{A.5}$$

The actual robot velocity $v_r(t)$ is then measured. Robot velocity tracking after transients have attenuated is shown for three frequencies in Fig. A.5. The empirical transfer function estimate is

$$\hat{G}_r(j\omega) = \frac{V_r(j\omega)}{V_{r,d}(j\omega)} \tag{A.6}$$

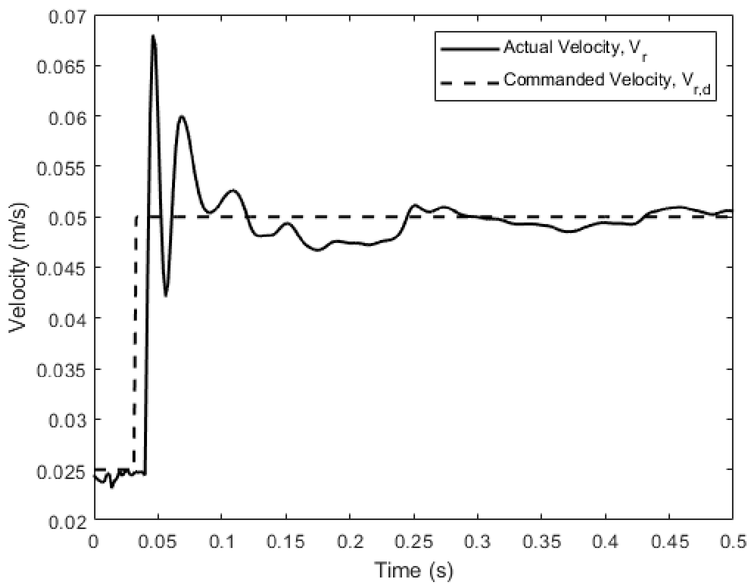

Figure A.4: Step response of the robot velocity controller. The robot is initially moving at 2.5 cm/s and is commanded to a 5.0 cm/s velocity. The velocity is based on the numerical differentiation of joint angles, so the step response is noisy.

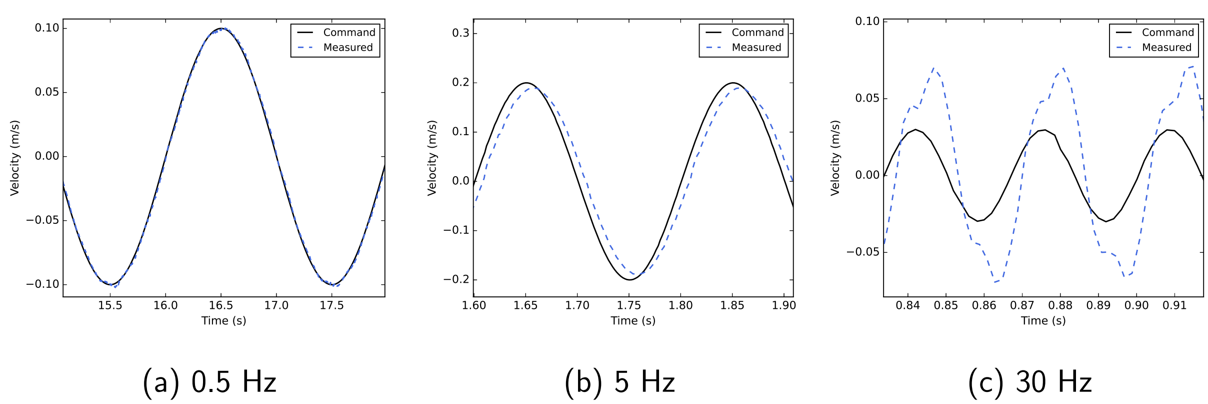

Figure A.5: Robot velocity tracking at different frequencies.

where V_r and $V_{r,d}$ are the FFTs of the actual and desired robot velocities. The time signals are truncated to minimize transients, and a Hann window is applied. This process is

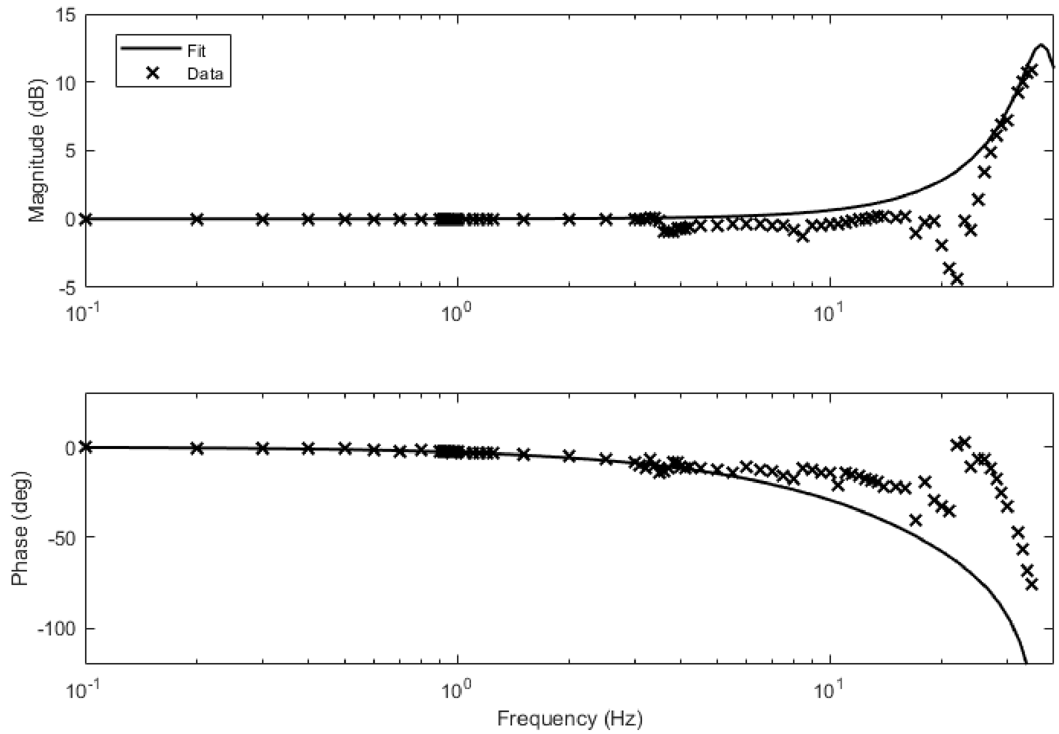

Figure A.6: Frequency response of the robot controller, $G_r(j\omega)$.

repeated for frequencies between 0.1 Hz and 35 Hz. The empirical transfer function estimate is shown in Fig. A.6.

The robot model parameters other than the delay, $\theta = (m_r, b_r, K_i, K_p)$, are then found using the collected data,

$$Z^N = \{V_r(\omega_k), V_{r,d}(\omega_k),\ k = 1, ...N\} \tag{A.7}$$

and solving the following minimization,

$$\hat{\theta} = \arg\min_{\theta} \sum_{k=1}^{N} \|V_r(\omega_k) - G_r(j\omega, \theta)V_{r,d}(\omega_k)\|^2 \tag{A.8}$$

which gives $\hat{\theta} = (4.5, 50, 250000, 200)$.

A.3 Motion Capture and Coordinate Transformation

A motion capture system (OptiTrack Flex 13) is used to determine the relative displacement between the robot end effector and a flexible structure. The motion capture system broadcasts the location of rigid bodies via UDP at 125 Hz and has a rated accuracy of ±0.2 mm. The motion capture system provides the positions of rigid bodies within its own measurement frame, denoted O_m. To transform these measurements into the robot TCP coordinate frame, O_r, a calibration routine is executed.

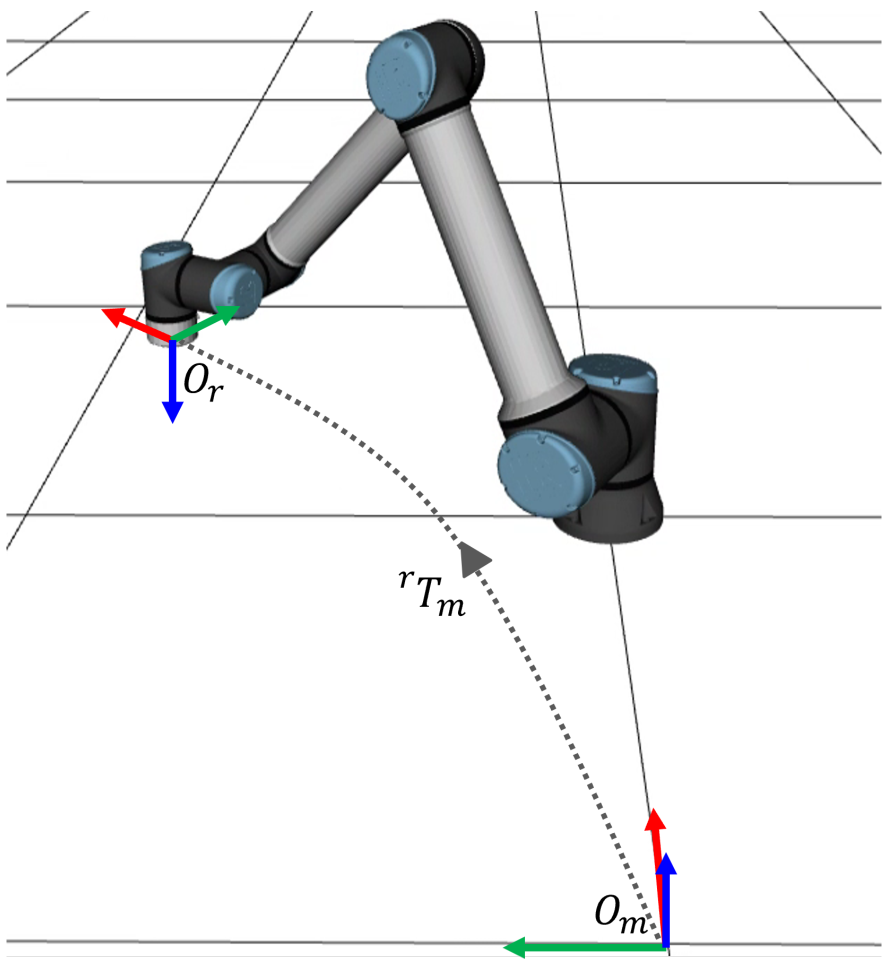

Figure A.7: Illustration of the robot and motion capture coordinate frames.

During the calibration procedure, the robot is manually jogged while recording the end-effector positions computed via the robot controller's forward kinematics, denoted as ${}^{r}\mathbf{p}_i$ for the i-th sample. The points are represented as $\mathbf{p}_i = (x, y, z, 1)^{\intercal}$. In parallel, the corresponding positions are captured by the motion capture system, ${}^{m}\mathbf{p}_i$. Given that the motion capture system operates at 125 Hz and the robot controller at 500 Hz, the data are temporally aligned by down-sampling the robot data to the motion capture rate through linear interpolation based on a common clock.

The 4×4 homogeneous transformation matrix ${}^{r}T_m$, which maps points from the motion capture frame O_m to the robot TCP frame O_r, is determined by solving the following least-squares optimization problem:

$$ {}^{r}T_m = \underset{{}^{r}T_m}{\arg\min} \sum_{i=1}^{N} \left\| {}^{r}\mathbf{p}_i - {}^{r}T_m \, {}^{m}\mathbf{p}_i \right\|^2 . \tag{A.9} $$

The least-squares transformation is computed using the Kabsch algorithm. This transformation is applied to all subsequent motion capture measurements to convert the flexible structure measurements to the robot's coordinate frame.

Appendix B
ONLINE HUMAN POSITION ESTIMATION

In MC2, human position is estimated after each trial and used to update the next trial. A natural question is whether the same estimate could be used online. In principle, this would let the robot track the human position directly, making the iterative method unnecessary. In practice, this approach is difficult to make robust. Higher-order object modes that are not modeled accurately can make the system unstable. The analysis below shows that small shifts in the identified modal frequencies can sharply reduce the stable online gain. Once that gain is reduced, or once the command filter is made more conservative to recover robustness, the online estimator no longer gives low deformation.

The flexible-object force model is

$$F(s) = G_{x_h}(s)X_h(s) - G_{x_r}(s)X_r(s), \tag{B.1}$$

so, with perfect knowledge of the object dynamics, the human position is

$$X_h(s) = G_{x_h}^{-1}(s)\left[F(s) + G_{x_r}(s)X_r(s)\right]. \tag{B.2}$$

Chapter 4 uses the model-based estimate

$$\hat{X}_h(s) = \hat{G}_{x_h}^{-1}(s)H_1(s)\left[F(s) + \hat{G}_{x_r}(s)X_r(s)\right], \tag{B.3}$$

where $H_1(s)$ is a realizable low-pass filter. It limits noise amplification and makes the inverse implementable. If $\hat{G}_{x_h}$ is nonminimum phase, then $\hat{G}_{x_h}^{-1}H_1$ denotes a stable, proper approximate inverse, not an exact unstable inverse. An online controller based on this estimate would command

$$V_{r,d}(s) = \gamma H_2(s)\left[\hat{X}_h(s) - X_r(s)\right], \tag{B.4}$$

where $H_2(s)$ is a command filter and γ sets the desired tracking rate. Fig. B.1 shows the closed-loop structure. The measured force contains the true robot-side dynamics G_{x_r}, while the estimator adds the model term $\hat{G}_{x_r} X_r$.

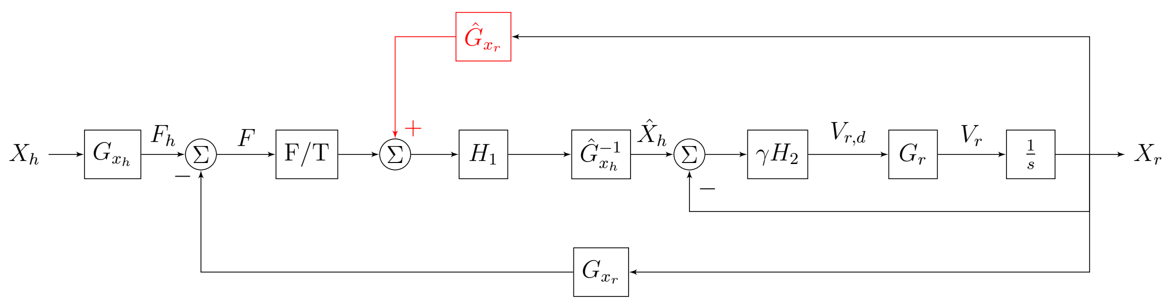

Figure B.1: Online human-position-estimation controller. The red model path shows where $\hat{G}_{x_r}$ is used to reconstruct $\hat{X}_h$ from the measured force and robot motion. The controller then subtracts the measured robot position X_r directly. Model mismatch leaves the residual $G_{x_r} - \hat{G}_{x_r}$ inside the closed-loop characteristic equation.

Using $sX_r(s) = G_r(s)V_{r,d}(s)$ and substituting (B.1) into (B.3) gives

$$\frac{X_r(s)}{X_h(s)} = \frac{\gamma H_1(s) H_2(s) G_r(s) G_{x_h}(s) \hat{G}_{x_h}^{-1}(s)}{s + \gamma G_r(s) H_2(s) \left[1 + H_1(s) \hat{G}_{x_h}^{-1}(s) \left(G_{x_r}(s) - \hat{G}_{x_r}(s)\right)\right]}. \tag{B.5}$$

With exact models and no filtering, $\hat{G}_{x_h} = G_{x_h}$, $\hat{G}_{x_r} = G_{x_r}$, and $H_1 = H_2 = 1$, (B.5) reduces to

$$\frac{X_r(s)}{X_h(s)} = \frac{\gamma G_r(s)}{s + \gamma G_r(s)}. \tag{B.6}$$

If the robot bandwidth is high enough that $G_r(s) \approx 1$ over the human-motion bandwidth, the deformation transfer function becomes

$$\frac{X_h(s) - X_r(s)}{X_h(s)} = \frac{s}{s + \gamma}, \tag{B.7}$$

which can be made small over the human-motion bandwidth by increasing γ. With perfect cancellation, the flexible-object dynamics disappear from the denominator.

B.1 Model-Error Sensitivity

The difficulty is the residual robot-side model error

$$\Delta_r(s) = G_{x_r}(s) - \hat{G}_{x_r}(s). \tag{B.8}$$

This term appears in feedback because the measured force contains the true robot-side force $-G_{x_r}X_r$, while the estimator adds back the modeled term $+\hat{G}_{x_r}X_r$. Collecting the terms that multiply X_r gives the characteristic equation

$$1 + \gamma L_\gamma(s; \Delta_r) = 0, \qquad L_\gamma(s; \Delta_r) = \frac{G_r(s)H_2(s)}{s}\left[1 + H_1(s)\hat{G}_{x_h}^{-1}(s)\Delta_r(s)\right], \tag{B.9}$$

so L_γ is the open-loop transfer function used for the standard SISO gain-margin calculation. For a fixed model, the upper gain margin is the largest positive value of γ that can be used before the online estimator becomes unstable. The gain margin gives a direct stability test for each model in the structured perturbation family.

With $\Delta_r = 0$, $G_r = 1$, and the fourth-order Butterworth filter used below, $L_\gamma = H_2/s$ has an upper gain margin of 14.37. Thus the exact-model loop remains stable for a useful range of positive γ. A small margin in the perturbed case comes from the phase and magnitude added by the model-error feedback term.

B.2 Perturbation Simulation

The study uses the identified 12th-order robot-side object model $\hat{G}_{x_r}$ from Fig. 4.6, the identified inverse $\hat{G}_{x_h}^{-1}$ used in Chapter 4, and the simplified robot model $G_r = 1$. The estimator filter is set to $H_1 = 1$ so the effect of robot-side model error is not hidden by another filter. The command filter H_2 is a standard fourth-order Butterworth low-pass filter with cutoff $f_c = 4$ Hz.

The perturbation is simple: every pole frequency of $\hat{G}_{x_r}$ is shifted by the same percentage while preserving damping ratios, zeros, and DC stiffness. The additive error is

$$\Delta_r(s; \epsilon) = G_{x_r,\epsilon}(s) - \hat{G}_{x_r}(s). \tag{B.10}$$

For the representative case used below, $\epsilon = 2.0\%$. This level of pole-frequency error is reasonable for a hand-held flexible object. The identified model is obtained for one grasp and nominal configuration, while the online controller would be used with a human holding the object, possibly at a different grip location, grip stiffness, preload, or deformed operating point. From standard modal analysis, a flexible-mode frequency satisfies

$$\omega_i^2 = \frac{\phi_i^T K \phi_i}{\phi_i^T M \phi_i}, \tag{B.11}$$

where ϕ_i is the mode shape and K and M are the stiffness and mass matrices [56]. Thus, to first order, $\Delta\omega_i/\omega_i \approx \frac{1}{2}(\Delta k_i/k_i - \Delta m_i/m_i)$ for the corresponding modal stiffness and modal mass. A 2% pole-frequency shift therefore corresponds to only about a 4% change in effective modal stiffness or mass. Small changes in boundary stiffness, grip location, or nominal shape can easily create shifts of this size, especially for higher-order modes. The resulting perturbed model remains close to the identified model in the low-frequency range and preserves the same static stiffness.

For each ϵ, $\Delta_r(s;\epsilon)$ is substituted into (B.9). Figure B.2 shows the corresponding open-loop calculation. With no model error, the exact-model loop has $\gamma_{\max} = 14.37$. With a 2.0% pole-frequency perturbation, the smallest gain margin drops to $\gamma_{\max} = 4.68$, limited by a crossing near 23.4 Hz. The exact-model loop is not fragile because of the integrator alone. The loss of margin comes from the residual model-error term in (B.9).

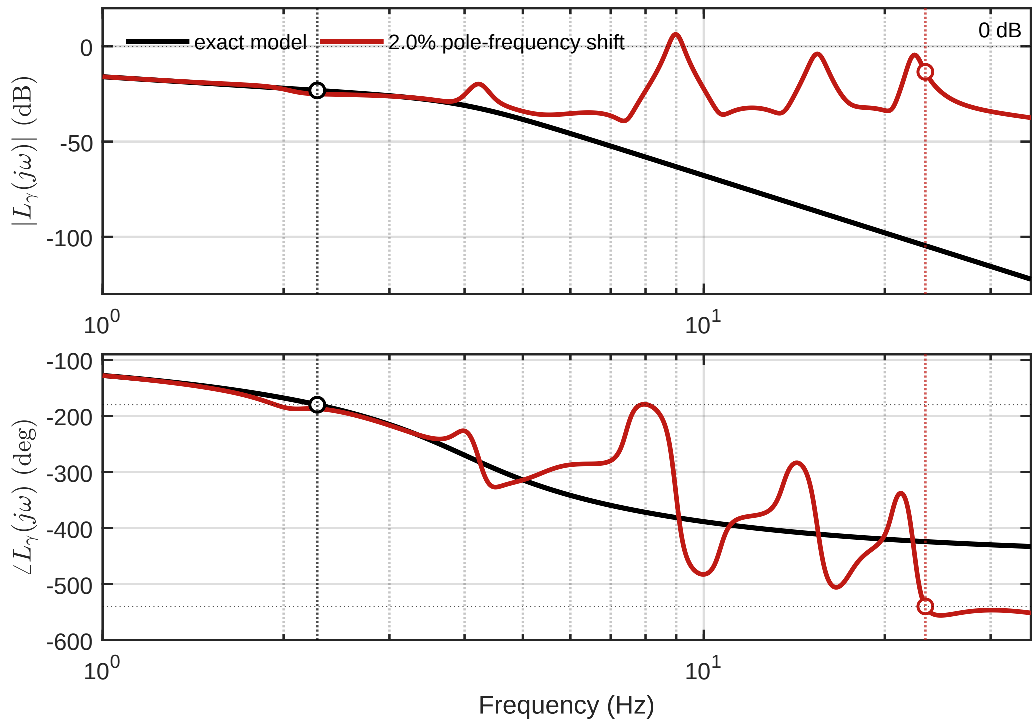

Figure B.2: Open-loop gain-margin comparison for the online estimator with a fixed fourth-order, 4 Hz Butterworth command filter. Black denotes the exact-model loop and red denotes the 2.0% pole-frequency perturbation. The exact-model loop has $\gamma_{\max} = 14.37$, while the perturbation reduces the allowable gain to $\gamma_{\max} = 4.68$.

The closed-loop tracking transfer function for the same perturbation is

$$T_\epsilon(s) = \frac{\gamma H_2(s)}{s + \gamma H_2(s)\left[1 + \hat{G}_{x_h}^{-1}(s)\Delta_r(s;\epsilon)\right]}. \tag{B.12}$$

For a sinusoidal human motion $x_h(t) = A\sin(2\pi \cdot 0.5t)$, the RMS deformation percentage is normalized by the sinusoid amplitude, as in the main chapters:

$$\delta_{\mathrm{rms},0.5}(\epsilon) = \frac{100}{\sqrt{2}}\left|1 - T_\epsilon\left(j2\pi \cdot 0.5\right)\right|. \tag{B.13}$$

This metric includes both magnitude error and phase lag. Figure B.3 uses $\gamma = 0.9\gamma_{\max}$ for each case to provide gain margin. The exact-model case still has 18.07% RMS deformation because it includes the same fourth-order 4 Hz command filter and finite gain margin. The "exact model" does not mean zero deformation; it means the object model is correct ($G_{xr}(s) = \hat{G}_{xr}(s)$). With the 2.0% pole-frequency perturbation, the RMS deformation increases to 50.94% even though the gain is reduced below the perturbed stability limit.

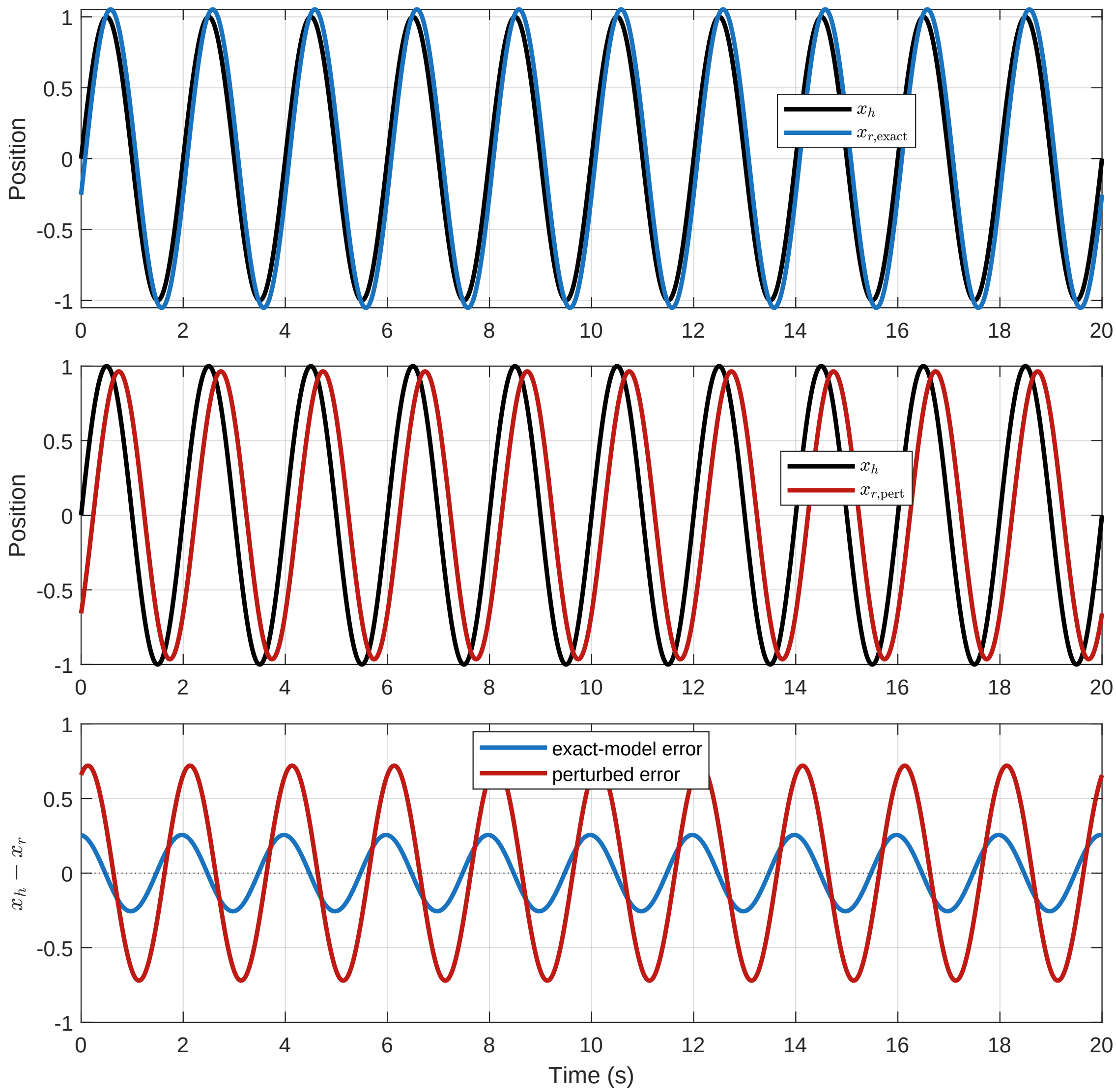

Figure B.3: Closed-loop 0.5 Hz tracking comparison using $\gamma = 0.9\gamma_{\max}$ for each case. The top panel shows exact-model tracking, the middle panel shows tracking with the 2.0% pole-frequency perturbation, and the bottom panel compares the resulting deformation $x_h - x_r$. The exact-model case has 18.07% RMS deformation because the command filter and finite gain remain in the loop, while the perturbation increases the RMS deformation to 50.94%.

Figure B.4 sweeps the pole-frequency shift from 0 to 3% with the same fixed filter. At

$\epsilon = 0$, $\gamma_{\max} = 14.37$ and $\delta_{\text{rms},0.5} = 18.07\%$. At $\epsilon = 1.0\%$, the allowable gain drops to 9.08 and the deformation increases to 28.72%. At $\epsilon = 2.0\%$, the allowable gain drops to 4.68 and the deformation increases to 50.94%. At $\epsilon = 3.0\%$, the allowable gain drops to 3.27 and the deformation increases to 62.75%. The very small perturbation case is not strictly monotonic because shifting the poles can move the limiting phase crossing in either direction, but the trend shows that percent-level modal-frequency errors can remove a large fraction of the stable online gain and more than double the deformation.

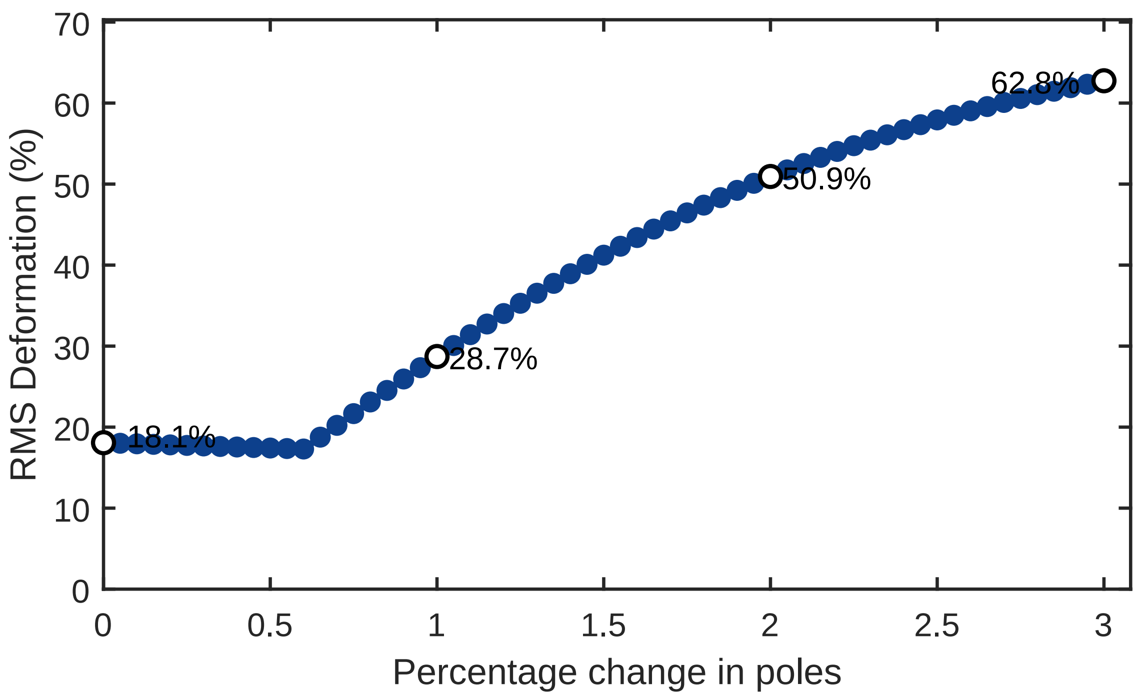

Figure B.4: Effect of uniform pole-frequency error on online tracking deformation with the fixed fourth-order, 4 Hz Butterworth command filter. Each point recomputes the open-loop gain margin of (B.9), sets $\gamma = 0.9\gamma_{\max}$, and evaluates the normalized 0.5 Hz RMS deformation from (B.13).

More aggressive filtering can recover some robustness, but that comes at the cost of tracking. A separate sweep over Butterworth order and cutoff for the 2.0% perturbation found the best case at order four with a more conservative 3.11 Hz cutoff. Even then, the 0.5 Hz RMS deformation was 27.10%. If the filter has a high-frequency cutoff, small model errors reduce the allowable gain. If the filter is made more conservative, phase lag and limited bandwidth increase deformation. This explains why the estimator is used offline between trials in Chapter 4. Offline iterative estimation can use the model-based inverse without making the model-cancellation errors part of the real-time feedback characteristic equation.

Appendix C
BASELINE-MODEL SIMULATION STUDY

Chapter 4 is motivated by the case where the object dynamics are low enough in frequency that MC1-style inverse compensation no longer gives small deformation during a single trial. This appendix studies that transition using the same two-mass baseline model as the motivating example. The first internal flexible mode is moved through the range relevant to voluntary human motion, and performance is reported using the same normalized 0.5 Hz RMS deformation metric used in Appendix B.

This study is separate from the robustness analysis in Appendix B. Appendix B considers model mismatch in an online cancellation loop. Here, the model is treated as known so that the limiting effect of the object natural frequency can be isolated. Even under this best-case assumption for MC1, low-frequency flexible-object dynamics can prevent small within-trial deformation.

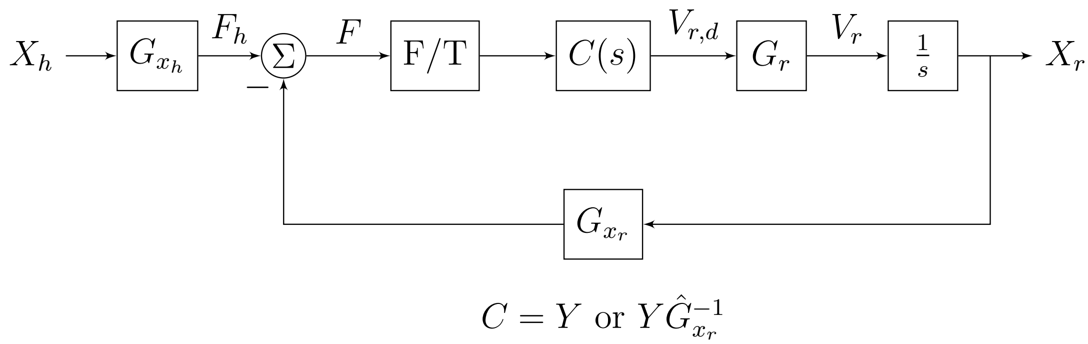

Figure C.1: Closed-loop simulation architecture for the baseline-model sweep. The flexible-object model maps human and robot motion to the force measured at the robot wrist. The controller block is set to standard admittance, $C(s) = Y(s)$, or to the MC1-style inverse-compensated controller, $C(s) = Y(s)\hat{G}_{x_r}^{-1}(s)$.

The measured force in the baseline model is

$$F(s) = G_{x_h}(s)X_h(s) - G_{x_r}(s)X_r(s), \tag{C.1}$$

where

$$G_{x_r}(s) = m_2 s^2 + c_2 s + k_2 - \frac{(c_2 s + k_2)^2}{D(s)}, \tag{C.2}$$

$$G_{x_h}(s) = \frac{(c_2 s + k_2)(c_1 s + k_1)}{D(s)}, \tag{C.3}$$

$$D(s) = m_1 s^2 + (c_1 + c_2)s + (k_1 + k_2). \tag{C.4}$$

At zero frequency, both transfer functions reduce to the equivalent stiffness

$$K_{eq} = G_{x_r}(0) = G_{x_h}(0) = \frac{k_1 k_2}{k_1 + k_2}. \tag{C.5}$$

Thus, standard admittance control sees an approximately spring-like object only when the human-motion frequencies are well below the flexible-object dynamics. The pole pair associated with the internal flexible-mode denominator $D(s)$ has undamped natural frequency

$$\omega_n = \sqrt{\frac{k_1 + k_2}{m_1}}, \qquad f_n = \frac{\omega_n}{2\pi}, \tag{C.6}$$

with damping ratio

$$\zeta = \frac{c_1 + c_2}{2\sqrt{m_1(k_1 + k_2)}}. \tag{C.7}$$

The sweep varies this first internal flexible-mode frequency by varying m_1 while keeping the static stiffness K_{eq} fixed. For each selected natural frequency f_n,

$$m_1(f_n) = \frac{k_1 + k_2}{(2\pi f_n)^2}. \tag{C.8}$$

The nominal damping ratio ζ_0 and the relative damping distribution are preserved by setting

$$\eta_i = \frac{c_{i,0}}{c_{1,0} + c_{2,0}}, \qquad i \in \{1, 2\}. \tag{C.9}$$

Then set

$$c_i(f_n) = \eta_i \, 2\zeta_0 \sqrt{m_1(f_n)(k_1 + k_2)}, \qquad i \in \{1, 2\}. \tag{C.10}$$

The standard admittance controller uses $Y(s) = \alpha\omega_c/(s + \omega_c)$ and gives

$$T_{adm}(s) = \frac{Y(s)G_r(s)G_{x_h}(s)}{s + Y(s)G_r(s)G_{x_r}(s)}. \tag{C.11}$$

For the MC1 comparison, the sweep uses a best-case exact normalized inverse, $K_{eq}G_{x_r}^{-1}(s)$, so that

$$T_{MC1}(s) = \frac{K_{eq}Y(s)G_r(s)G_{x_r}^{-1}(s)G_{x_h}(s)}{s + K_{eq}Y(s)G_r(s)}. \tag{C.12}$$

Following Appendix B, performance is evaluated with a sinusoidal human input

$$x_h(t) = A\sin(2\pi \cdot 0.5t).$$

For each f_n and each stable controller setting, the normalized RMS deformation percentage is

$$\delta_{\mathrm{rms},0.5}(f_n) = \frac{100}{\sqrt{2}} \left|1 - T\left(j2\pi \cdot 0.5; f_n\right)\right|. \tag{C.13}$$

where T is either (C.11) or (C.12). This metric includes both magnitude error and phase lag. To keep the comparison tied to stability-limited controller bandwidth rather than retuning the controller for a single sinusoid, the cutoff is fixed at $\omega_c = 10$ rad/s. For each f_n, α is swept over the same design grid used in the motivating example, $0.1 \leq \alpha \leq 10$, and the plotted value uses 90% of the largest stable gain in that grid. Under exact inverse compensation, the closed-loop stability limit is independent of f_n, so the same MC1 gain is used across the sweep.

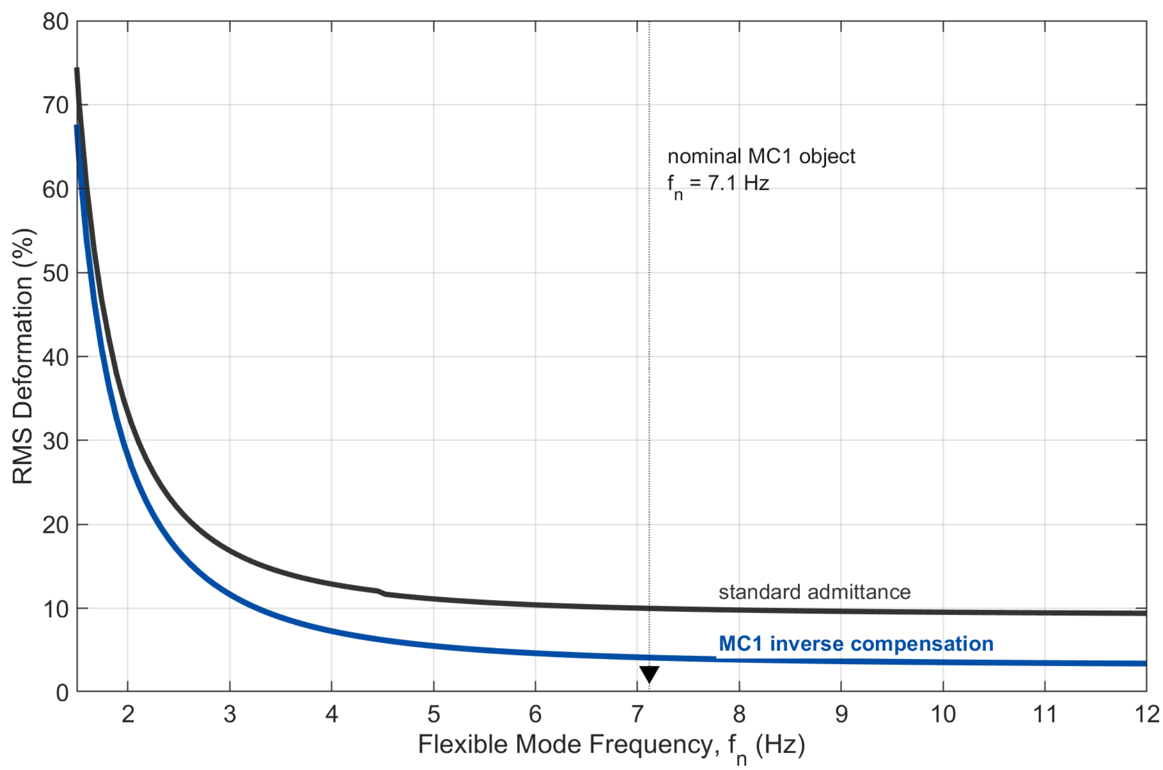

Figure C.2: Baseline-model natural-frequency sweep for a 0.5 Hz sinusoidal human input. The cutoff is fixed at $\omega_c = 10$ rad/s, and each point uses 90% of the largest stable gain in the controller grid to provide gain margin. The dotted vertical line marks the nominal MC1 object frequency. At the nominal object frequency, MC1 reduces the simulated RMS deformation from about 10.0% to 4.1%. When the flexible mode moves into the low-frequency range relevant to voluntary motion, both within-trial controllers produce large deformation.

Figure C.2 summarizes the transition. When the flexible mode is high enough relative to the 0.5 Hz input, the object behaves nearly like a spring during the task, and standard admittance can keep deformation moderate. MC1 reduces deformation in this case by using the inverse model to allow a more aggressive stable response. As the flexible mode moves into the low-frequency range relevant to voluntary motion, however, the MC1 curve also rises. In this range, the limitation is not only stability or controller tuning. Even with exact inverse compensation of the robot-side dynamics, the closed-loop response still contains the ratio $G_{x_h}(s)/G_{x_r}(s)$, and that ratio is strongly distorted when the object mode lies near the task frequency. These low-frequency cases are the ones addressed by MC2, where improvement is obtained across repeated trials rather than by increasing within-trial admittance alone.